High-Resolution And Large-Area Laser Interference Nanomanufacturing Technology

Dapeng Wang

University of Bedfordshire

HIGH-RESOLUTION AND LARGE-AREA LASER INTERFERENCE NANOMANUFACTURING TECHNOLOGY

by

Dapeng Wang

A thesis submitted to the University of Bedfordshire, in fulfilment of the requirements for the degree of Doctor of Philosophy

March 2015

Abstract

The thesis systematically investigates the laser interference nanomanufacturing technology taking into account its advantages and abilities to realise various potential applications. The latest progresses have addressed the major issues hampering the cross-scale developments of structural applications, such as cost-ineffective fabrication, limited area, low efficiency and challenging integration. The studies carried out on high-resolution and large-area laser interference nanomanufacturing technology will complement the exploration of modern optical devices and extraordinary functional applications.

With respect to classical interference theory and relevant references, there is still a lack of studies providing insight into the effects of polarisation on the multi-beam interference while it is found that the polarisation vector plays a key role in the formation, period and contrast of interfering patterns. Herein, the theory of multi-beam interference is developed through the integration of the polarisation vector and electric field vector. It is worth pointing out that based on the detailed analysis of the four-beam interference with the special polarisation modes, it is demonstrated that the modulation phenomenon in four-beam laser interference is the result of the misalignment of incident angles or unequal incident angles only in the case of the TE-TE-TM-TM mode.

In the experiments, a straightforward method of generating various well-defined structures on material surfaces is proposed using the nanosecond laser interference system. The experimental results of two-, three- and four-beam interference show a good correspondence to the theoretical analyses and simulations. Artificial bio-structures are fabricated using the four-beam interference method with the TE-TE-TE-TE polarisation mode and the fabricated microcone structures exhibit excellent properties with both a high contact angle (CA=156.3˚) and low omnidirectional reflectance (5.9-15.4%). In order to

fabricate high-resolution structures, the 266nm nanosecond laser interference system is employed to treat the organic and metal-film materials. Nanograting structures with feature sizes of sub-100nm width and 2nm height are fabricated on the organic material surface. An attempt is successfully conduced to produce the nanoelectrode arrays by using laser interference lithography and chemical deposition. Finally, the advantages of the developed laser interference technology and contributions of the research are summarised, and recommendations of future work are given.

Acknowledgement

I would like to express the deepest gratitude to my supervisors, Professor Yong Yue and Professor Zuobin Wang, for their kind help and precise guidance throughout this work. They are both outstanding advisors. I have learned a tremendous amount from them, not only in science, but also about ideas and skills that will be invaluable in my professional life.

True appreciation is given to the International Research Centre for Nano Handling and Manufacturing of China (CNM) for providing me an opportunity to carry out the experimental work. I wish to extend my sincere thanks to Dr. Jia Xu, Mr Ziang Zhang, Ms Yang Liu, Dr. Li Li and all the members for teaching me along my study. There are endless wonderful memories at CNM.

I really appreciate Professor Dayou Li, Professor Carsten Maple, Dr. Shuang Gu, Mr Tao Cao and Dr. Beisheng Liu at IRAC for providing a large amount of useful information and references.

Finally, I am deeply grateful for my families and all the best friends, e.g. Mr Linghao Meng and Mr Shaomeng Shen, for their continuing love and support, without which I would not have achieved my study goals.

List of Contents

List of Figures

List of Tables

Nomenclature

A_n	Amplitude
k	Wave number (k=2π/λ)
ω	Frequency
t	Given point in time
φ	Initial phase
$\vec{E}$	Electromagnetic wave vector
$\tilde{E}_m$	Complex exponential form of mth electric field vector
$\tilde{E}_n^*$	Conjugate function of $\tilde{E}_n$
$\vec{k}_m$	The mth vector in the propagation direction
$\vec{r}_m$	The mth position vector
I	Intensity distribution
$\vec{i}$	x unit vector in Cartesian coordinates
$\vec{j}$	y unit vector in Cartesian coordinates
$\vec{k}$	z unit vector in Cartesian coordinates
θ	Incident angle
ϕ	Azimuthal angle
P or d	Period
λ	Wavelength
n	Refractive index
h	Thickness of the coating
$\gamma_{S/V}$	Solid/vapour interfacial free energy
$\gamma_{S/L}$	Solid/liquid interfacial free energy
$\gamma_{L/V}$	Liquid/vapour interfacial free energy
R_f	Roughness factor
ψ_L	Solid surface area fraction of the solid and air
ψ_A	Air surface area fraction of the solid and air
$\vec{p}_m$	Polarisation vector
ψ	Polarised angle
ρ_{XY}	Correlation coefficient
E	Expected value

cov	Covariance
μ_x	Mean values of image patch X
μ_y	Mean values of image patch Y
K	Interference contrast
I_{max}	Maximum interference intensity
I_{min}	Minimum interference intensity
CA	Contact angle
$T=T(x,z,t)$	Temperature at the position (x, z) at time t
q_a	Absorbed heat
q_m	Heat of melting
q_v	Heat of vaporisation
ρ	Density
c_p	Specific heat of the material
k	Thermal conductivity
t_p	Pulse time
τ_p	Pulse duration
r	Reflectivity of surface
L_m	Latent heat of fusion
T_m	Melting temperature
T_b	Boiling temperature
L_v	Latent heat of vaporisation
χ	Thermal diffusivity

Declaration

I declare that this thesis is my own unaided work. It is being submitted for the degree of Doctor of Philosophy at the University of Bedfordshire.

It has not been submitted before for any degree or examination in any other University.

Name of candidate: DAPENG WANG Signature: 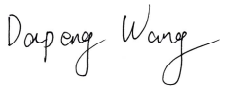

Date: 16 March 2015

Chapter 1

Introduction

1.1 Background

"*There is Plenty of Room at the Bottom*" was a lecture given by the professor Richard Feynman in 1959. The speaking is regarded as a prime event in the history of nano world for it inspires the conceptual beginnings of the field. At present, nanoscience and nanotechnology are increasingly important research topics since quantities of exciting new physical and chemical mechanisms and countless applications are explored when the feature shape or characteristic dimension of matter is down to atomic and molecular scales. The latest developments have shown that novel nanostructures with reducing the size of dimensionality can exhibit a number of exceptional abilities, such as meta-materials [1], surface plasmon polaritons (SPPs) [2, 3], quantum dots [4], and bionic structures [5, 6]. These progresses in nanostructures design and realisation will lead to novel functionalities. Hence, nanomanufacturing is a key branch and attracting the global attentions.

1.2 Overview of Current Micro and Nano Fabrication Technologies

A number of approaches for fabrication of micro and nano structures have been proposed by worldwide scientists, e.g. optical lithography (OL), laser interference lithography (LIL), wet and dry etching, electron beam lithography (EBL), focused ion beam lithography (FIB), scanning probe lithography (SPL), nanoimprint lithography (NIL).

OL, also named as photolithography, is a process to transfer a geometric pattern to a thin layer of photosensitive resist by means of optical mask. A complex optical system and series of subsequent processes are included in the whole

process, which determines its extremely high cost. It affords the expensive cost both in initial (> $20 million) and in operating investments (A typical mask set costs exceed $1 million) [7]. Nonetheless, OL is still one of the most powerful tools for the mass production of integrated circuits (IC) industry. Quantities of advanced microchips or microprocessors are fabricated by OL as well.

LIL is a regular pattern definition technique without the use of complex optical system and mask. The interference pattern consists of a series of periodic grating bump or hole features recorded on photosensitive resist. Although LIL is not a one-stop process like focused ion beam lithography and laser writing, it has the advantage of producing a complete substrate within one single exposure and offers the possibility to realise a well-defined micro and nano structured surfaces on a macro scale. There are many parameters associated with laser interference lithography to achieve precision control, e.g. wavelength, incident angle, azimuthal angle, polarised angle, phase and refractive index of surrounding medium, but it is regarded as a promising tool for the fabrication of advanced structures like anti-reflection and self-cleaning surfaces.

Wet etching is a micro fabrication method by using liquid chemicals to remove in which the material is dissolved when immersed in a solution. Some single crystal materials, such as silicon, exhibit the anisotropic etching rate depending on the material crystalline direction. The classic example is that the <111> crystal plane sidewalls appear when etching rather than a hole in a <100> silicon wafer in the potassium hydroxide (KOH). The result is a pyramid shaped hole instead of a hole with rounded sidewalls with an isotropic etchant. Wet etching is a standard procedure of commercial solar cells texturing.

Dry etching refers to utilise a physical, chemical principle or a combination of both to remove the substrate materials. Generally, plasma etching (PE) and reactive ion etching (RIE) are most widely used in mass production. By exposing substrate to bombardment ions, only the unmasked material where physical or chemical reaction takes place will be removed. Therefore, dry etching is an

anisotropic process and has the advantage of high level of resolution. Similar to wet etching, the chemical etchants and gases used during manufacturing are quite toxic and corrosive.

EBL and FIB belong to dry etching and recently have been developed to the powerful technologies for prototyping with higher resolution at below 10nm but take a competitive disadvantage of time consuming as a result of their serial point-by-point writing modality. For example, approximately one week is needed to pattern 160nm lines spaced 500nm apart over a $1cm^2$ area with an e-beam operating at 500KHz and with an exposure dimension of 10nm. Hence, they are suitable for producing the custom design templates or masks.

SPL is used to write microscopic patterns on material surfaces. This technique uses a scanning tunneling microscope or atomic force microscope to apply chemicals to a surface, or manually modify the surface. Through the processes of alteration and application with a sharp tip, high-resolution nanoscale patterns are created. But, it is extremely slow, and is currently only used for constructing surface model systems.

NIL is an attractive method for low cost nanopatterning. The NIL process is a mechanical replication process where a surface relief from a template is embossed onto a thin polymer layer on the substrate. Two versions of NIL are typically employed: the first is based on thermal embossing of thermoplastic polymers and the second is based on transparent stamps and UV-curable polymers.

Any discussion of tools for micro and nano fabrication necessarily involves consideration of the manufacturing cost both in resources and in time. There is no research community or company which has resources for everything and they must make choices based on affordability and productivity. Through many years development, each technology has own advantages, disadvantages and special potential for various applications, as concluded in Table 1.

Table 1 Advantages and disadvantages of OL, LIL, EBL, FIB and SPL.

Names	Advantages	Disadvantages
OL	High-throughput, Large area	High cost, Fixed pattern
LIL	Controlled periodicity, Low cost	Multiple processes
EBL	High resolution, Flexible pattern	High cost, Low efficiency
FIB	High resolution, Flexible pattern	High cost, Low efficiency
SPL	Flexible pattern	Limited materials, Low efficiency
NIL	High throughput, Mass production	Template dependent

In the mentioned technologies, they can be divided into two categories: direct technologies and indirect technologies. As shown in Fig. 1.1, indirect technology refers to OL, LIL and NIL. Direct technology refers to NIL, FIB, EBL and SPL, respectively. Compared with them, direct laser interference nanomanufacturing technology has both indirect and direct characteristics. When the fabricated material is photosensitivity resist, it's similar to laser interference lithography. In contrast, it also can be used to modify the solid materials (e.g. silicon, metal and so on) to generate micro and nano structures on surfaces as the direct technology.

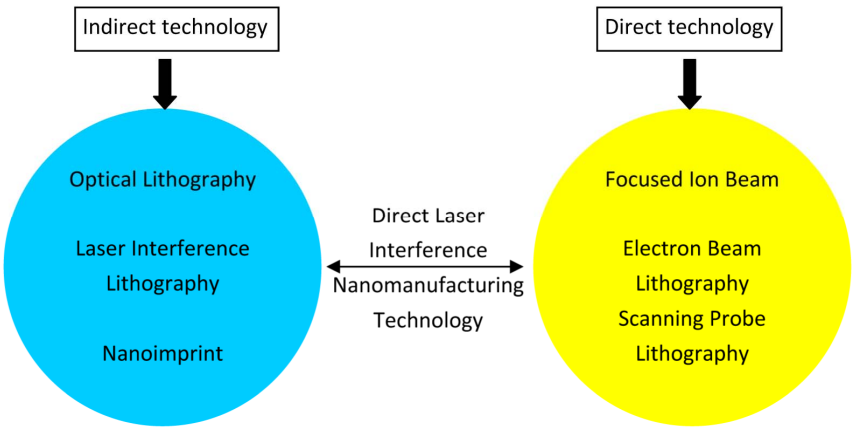

Fig. 1.1 Indirect and direct technologies.

With the merits of simple system and facile technological procedure, direct laser

interference nanomanufacturing (DLIN) is a promising tool for mass production and expected to overcome drawbacks of other technologies. It is a powerful technology with the capability for the manufacturing of micro and nano structures at the same time and offers the distinct potential to fabricate various materials over large area. Compared with the attentions attracted by LIL, there is a lack of the detailed investigation to improve the ability of DLIN and explore more significant applications. Thus, laser interference especially direct laser interference nanomanufacturing technology with high resolution and large area is necessary to be researched and further developed.

1.3 Overview of Laser Interference Lithography

Laser interference lithography (LIL) is a maskless technique and the basic principle for interference is the same as in interferometer and holography. Due to rapid development of surface nanopatterning, nanoelectronic and nanophotonic devices, LIL has become increasingly important as it enables to generate a facile, inexpensive and large-area micro and nano structures. LIL uses a number of coherent beams from different directions in two-dimension or three-dimension configuration to produce an interference pattern. The patterns can form with arrays or matrices of lines, dots or many different distributions. Periodic structures are expected to apply for many advanced devices, such as diffractive optical elements, antireflective optical elements, photonic crystals and high-density magnetic materials [8]. LIL also plays a role in the fabrication of Micro-Electro- Mechanical Systems (MEMS) and biosensor [9].

With respect to the principle of LIL, it is well known that the grating period *d* is given by $d = \frac{\lambda}{2\sin\theta}$ in two-beam interference. So the simplest way of reducing the grating period is to use a laser source of shorter wavelength and larger incident angles. For example, at a 75° angle of incidence, $\sin\theta$=0.97, the limiting period is $\geq \lambda/2$ and extends below 100nm at a wavelength of 193nm. The

structure and periodicity are determined primarily by the wavelength of the laser used and the angles at which the different beams interfere with each other. But the dimensionality of the patterns depends on the number of laser beams. Very recently, a cross-scale pattern achieved by six-beam interference has been reported by our research team [10]. In the method, bionic Moth-eye structures for antireflection in the infrared band were produced. It can be confirmed that there will be more and more innovative and significant applications found with deep investigation of LIL and DLIN.

Around 1970, researchers found that holograms or diffraction grating were created on the photoresist surface and laser interference lithography was born. But the lack of desirable coherent source limits its development. Nonetheless, LIL had been an innovative tool since then and offered the focus depth at millimetre scale. For the early setup of interference experiment, Lloyd's minor interferometer was used widely because of making optical waveguides coupling flexibly. To date, a lot of efforts have been devoted to develop LIL. Ellman et al. reported that one and two dimensional periodic patterns were recorded in a 600 nm layer of AZ-1505 positive i-line photoresist [11]. Areas about 1 cm in diameter were processed with an optimum fluence of 20mJ/cm^2. They conclude a method to realise desired width of structures by controlling the thickness of photoresist. Baroni et al. used LIL and RIE to fabricate a hexagonal array of 145μm microlenses on a 4-inch quartz wafer [12]. To obtain a dimensional square lattice, double-exposure method was used by rotating the sample stage of 90˚. It was found that the microlenses structures showed a 15% improvement of reflectivity compared to unstructured area. By combining UV mask lithography and LIL, Yang et al. fabricated the hierarchical structures on a layer of photoresist [13]. Mask lithography was employed first to obtain micropatterns and subsequently the wafer was treated by LIL. The processes are shown in Fig. 1.2. Compared to one-dimensional nanograting structures achieved by LIL only, the hierarchical structures showed hydrophobicity by trapping air inside the structures and the maximum contact angle was 120±5˚. The findings will benefit the surface

engineering of microfluidic systems.

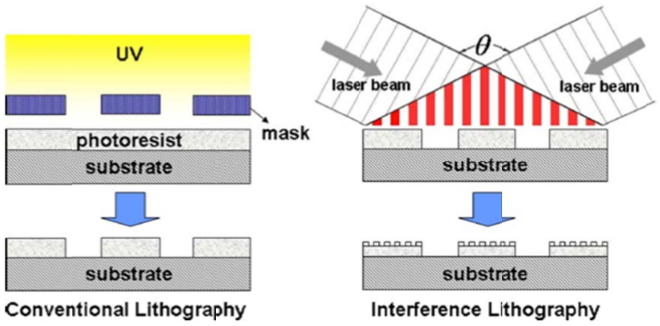

Fig. 1.2 The process for patterning composite structures. (Yang et al. 2010)

In order to realise nanofludic applications effectively, Pérez et al. presented a simple method to fabricate the metallic hollow-core nanostructures by LIL [14]. The processes can be described briefly as five step, i.e. photoresist spinning, exposure, develop, metal deposition and resist removal. By controlling the concentration of photoresist solution and spinning speed, two different thicknesses of 200nm and 600nm were obtained and corresponding metal hollow-core structures were fabricated, as shown in Fig. 1.3.

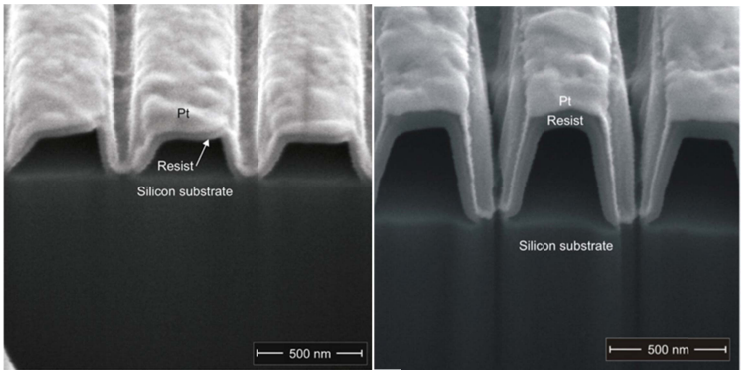

Fig. 1.3 Cross-sectional view of the samples after resist removal with thicknesses of (a) 200nm; (b) 600nm. The micrographs are taken at a tilt angle of 52°. (Pérez et al. 2012)

In the conclusion, they pointed out that the cross section of the channels is up to 100nm×100nm and the method made a break-through in the fabrication of hollow-core structures. In 2013, Seo et al. achieved 4cm^2-sized single-layer membrane reflectors on a two-dimensional photonic crystal (PC) structures using

LIL technique [15]. Moreover, a transfer printing technology was also employed to copy the membrane reflectors of PC onto glass successfully. Arrays of nanohole structures with the period of 610nm and feature size of 264nm were fabricated, as shown in Fig. 1.4. With the measurement of reflectivity, it can be seen as high as 95% around 1300nm and a bandwidth of 100nm. The work demonstrated a high throughput and low cost approach to impact on future optoelectronic and photonic applications.

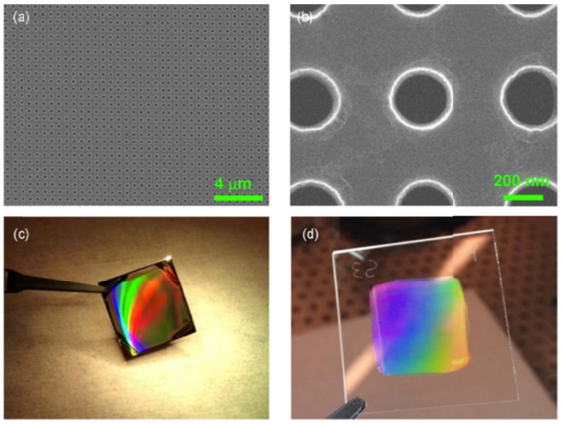

Fig. 1.4 (a) SEM image of the hole array pattern formed on a SOI substrate. (b) Zoomed-in image of (a). (c) Optical image of a LIL-patterned sample after dry etching of a top Si layer on SOI. (d) Optical image of a transferred Si NM MR on a glass substrate. (Seo et al. 2013)

As the attentions of surface-enhanced infrared absorption (SEIRA) increase, a number of approaches have developed to fabricate small-size metal structures. Bagheri et al. have recently published their novel work on antenna-assisted SEIRA fabricated by LIL [16]. After cleaning the substrates for 10 min in an ultrasonic bath, a 2nm thick chromium layer (adhesion layer) and 35nm thick gold layer were evaporated. Subsequently, a 90nm thick photoresist was coated on the substrates. The micro and nano structures were fabricated via LIL process and transferred into gold layer by means of argon ion beam etching. After the residues yielded in the fabrication process were removed, the samples need to be immersed into an octadecanethiol (ODT) solution in pure ethanol for at least 48 hours. The purpose of that is to form a monolayer of ODT covalently bound to the gold surface. Since the geometrical dimensions played a critical role in the resonance frequencies of

metal particles, a series of antennas with different lengths and widths varied from 2.1 to 0.8μm and 1 to 0.4μm respectively were fabricated. It was found that the enhanced transmission signal was improved by a factor of 6.4%. The fabrication of antenna-assisted SEIRA is enabled by LIL and the findings will expand the reach of infrared detection in life science and medicine and offer a possibility of chip-based technology [17].

From the literature review in brief of LIL, it has been demonstrated that LIL has a number of advantages compared to other technologies and additionally they are shown clearly in the bullet points.

- Controllable period ($d=\lambda/2\sin\theta$)

  It is well known that the period of tow-beam interference depends on the wavelength and incident angles, which means that the identical laser interference system enables to control the period from micrometre to nanometre theoretically by changing the incident angles, which is shown in Fig. 1.5. With respect to other micro and nano fabrication technologies, it's difficult to realise the controllable period. For instance, the chemical technologies are lack of controllability for the resulting structures faithfully depend on the order of magnitudes of crystal lattice. It is the only way to reduce the period for OL and dry etching with the help of smaller pitch mask. Additionally, EBL and FIB enable to adjust the period flexibly but at the cost of proximity error.

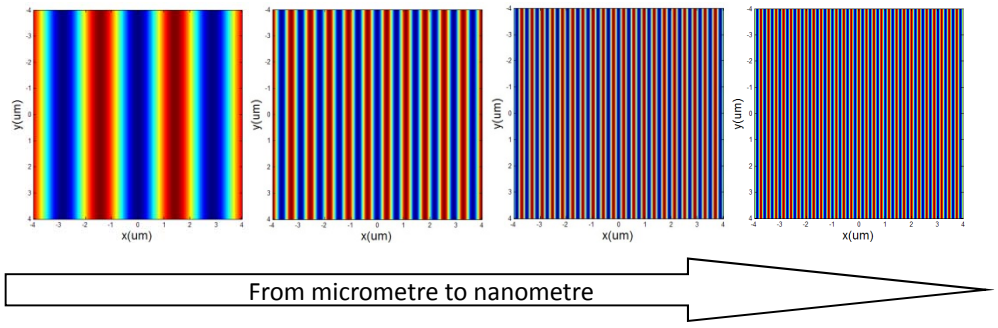

Fig. 1.5 Schematic diagram of controllable period.

Various patterns

For an interference image, there are a number of parameters which have a strong influence of the eventual pattern, such as wavelength, incident angle, azimuthal angle, polarised angle, phase and number of interfering beams. For the examples shown in Fig. 1.6, the grating, square dot, honeycomb array and dual-periodic array can be generated by LIL. It is worth mentioning that the dual-periodic patterns generally show a good agreement with the natural bionic structures. Inspired by these patterns, a number of artificial structures are fabricated, such as antireflection and self-cleaning coats. Apart from them, there are a huge number of variations in the special cases. With a deeper investigation of LIL, numerous emerging applications will be discovered.

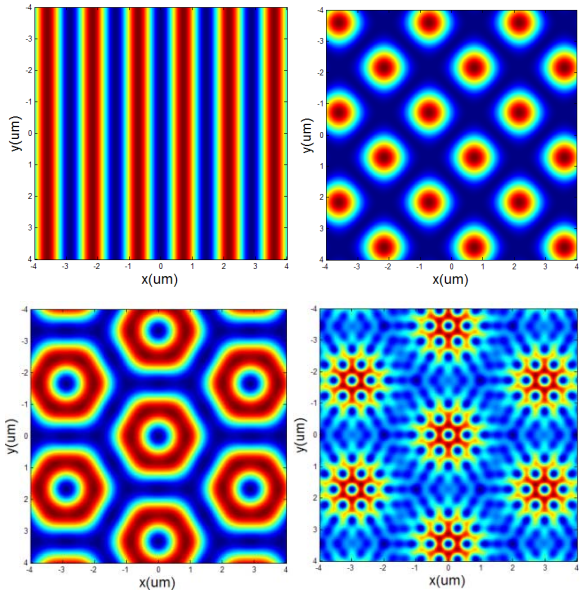

Fig. 1.6 Schematic diagram of various interference patterns.

Simple system

Generally, a LIL system consists of a laser source and several optical mirrors. Beamsplitters and high-reflective mirrors are used to divide the laser source into two, three, four beams and so on. Additionally, wave plates and polariser are used to control the phase and polarised angles of each beam.

Fig. 1.7 shows two interference systems in our laboratory, one is nanosecond interference system and the other one is 532nm interference system. The continuous laser system is basically suitable for exposing the photosensitive resist, while the high-pulsed laser system is applied to carry out the direct modification.

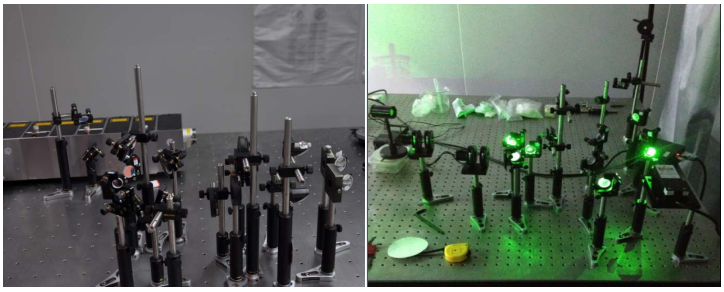

Fig. 1.7 Schematic diagram of common LIL systems.

- Parallel fabrication

Unlike to EBL and FIB, LIL produces the periodic patterns throughout the beam area at the same time. The output light from the laser mirror via the whole beam expander lens or spherical lenses enables to obtain a large area of uniform parallel light, and then several coherent beams superimpose together to expose the photoresist. Thus, LIL has the capability of large-area fabrication. The significant advantage makes LIL produce in a more efficient way.

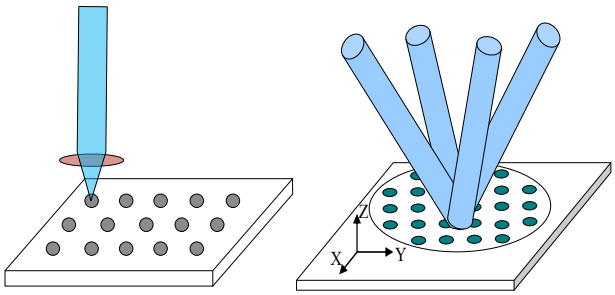

Fig. 1.8 Schematic diagram of point-by-point and parallel fabrication strategies.

But for the conventional LIL, its processes are similar with OL. Multiple essential processes have to be carried out successively to obtain nanostructures on the

samples. Fig. 1.9 indicates that the deposition, exposure, development, pattern transfer are indispensable steps in the whole procedure of indirect technologies. In comparison, direct technologies enable to fabricate micro and nano structures with only a single process. In the view of process number, direct technologies appear a category of efficient techniques. Additionally, every process is dependent on a number of relevant equipment for the indirect technologies, which certainly increases the operation cost. However, the direct technologies, for instance EBL, FIB and SPL, take a point by point or line by line writing strategy. They all suffer a time consuming nature. Therefore, quantities of applications demand current methods to develop a parallel technology which can fabricate the various structures with high efficiency and low cost. DLIN is the very technology. The pattern generated by the intensity distribution of interference is transferred to the material to produce periodic structures directly. In the research, a nanosecond laser interference system was used. With the help of fourth harmonic generators, ultraviolet wavelength of 266nm allows to carry out the high-resolution experiment. Combination with a linear stage and closed-loop system, DLIN has the ability to perform a large-area fabrication as well.

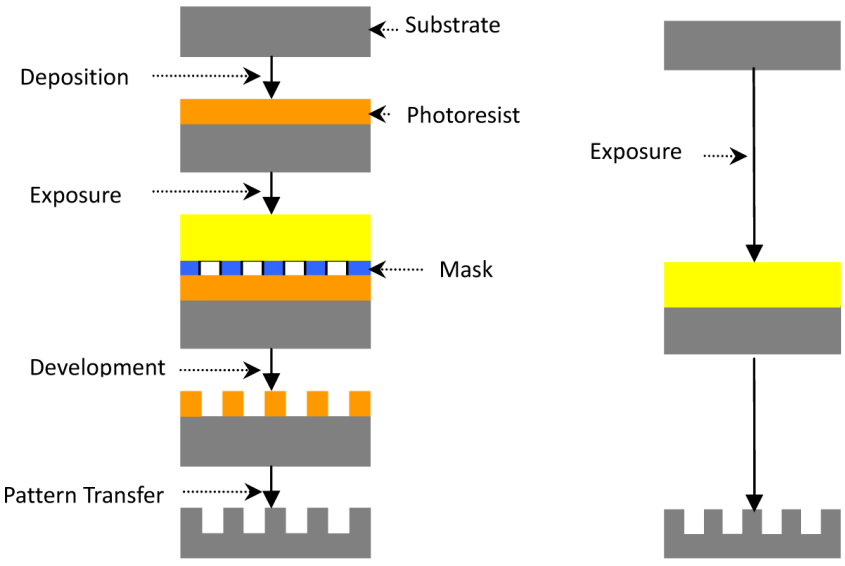

Fig. 1.9 Typical flow charts of indirect and direct processes.

1.4 Aim and Achievements of the Thesis

1.4.1 Aim and Objectives

In my work, I aim to develop LIL further for a high-resolution and large-area technique. The traditional LIL needs multiple technological procedures (e.g. deposition, exposure, development and wet or dry etching) and expensive equipment. To improve the fabrication ability towards high efficiency and low cost, Direct Laser Interference Nanomanufacturing (DLIN) is presented because of its numerous significant advantages. To realise the aim, a number of objectives are identified here and addressed in the following chapters.

- To gain an in-depth understanding of the principle of LIL, investigate the existing lithography technologies and critically analyse their advantages and disadvantages
- To explore the capability of LIL and DLIN for obtaining different nanostructure patterns with a large number of interference experiments and simulations
- To carry out nanosecond laser interference experiments and analyse the theoretical distribution and the interaction mechanism of materials processed with coherent nanosecond laser beams
- To study the effect of polarisation vectors on four-beam interference theoretically and experimentally
- To achieve large-area anti-reflection and superhydrophobicity structures by means of DLIN
- To simulate overlapping scans to approximate a uniform intensity distribution for large-area fabrication using Matlab and improve the alignment of scanning

- To conduct direct and indirect methods for improving the resolution of nanostructures and apply to nanoelectrode arrays

- To analyse the outcome, draw conclusions and contributions and recommend further work

1.4.2 Achievements

With respect to theoretical aspect, the work contributes to the multi-beam interference theory since the polarisation vector is taken into account and integrated into the electric filed vector. Through the combination of polarisation vector and electric field vector, a number of significant parameters are analysed and moreover the modulation phenomenon occurred in four-beam interference can be interpreted verifiably. As for the experiments, the 1064nm and 266nm nanosecond laser interference system were set up, aiming to fabricate large-area and high-resolution nanostructures respectively. With the investigation of the four-beam laser interference, both antireflection and superhydrophobicity functional surfaces are achieved successfully. In addition, the nanograting structures with feature sizes of sub-100nm width and 2nm height were fabricated. These findings pave an avenue for further development of laser interference technology.

During the subject of my PhD research work, a number of significant outcomes and meaningful achievements have been published in 7 high impact-factor journal papers and 6 conference papers. Some results described in the thesis are related to the previously published work in which I am the lead author. Chapter 3 cites the wok of “Determination of Beam Incidence Conditions Based on the Analysis of Laser Interference Patterns” which is submitted in International Journal of Light and Electron Optics. Chapter 4 cites the work of “Direct Modification of Silicon Surface by Nanosecond Laser Interference Lithography” and “Modification of Silicon Surface by Direct Laser Interference”. Chapter 5 cites the work of “Effects of Polarisation on Four-beam Laser Interference Lithography”.

Chapter 6 cites the work of “Both Antireflection and Superhydrophobicity Structures Achieved by Direct Laser Interference Nanomanufacturing” and “Anti-reflection Structures Fabricated by Direct Laser Interference Technology under Different Ambiances”. My publications are shown below.

Journal papers

1. **Dapeng Wang**, Zuobin Wang, Ziang Zhang, Yong Yue, Dayou Li, Renxi Qiu and Carsten Maple, “Both Antireflection and Superhydrophobicity Structures Achieved by Direct Laser Interference Nanomanufacturing” Journal of Applied Physics 115, 233101 (2014).

2. Jinjin Zhang, Zuobin Wang, Xu Di, Le Zhao, and **Dapeng Wang**, “Effects of Azimuthal Angles on Laser Interference Lithography”, Applied Optics 53, 6294 (2014).

3. Ziang Zhang, Zuobin Wang, **Dapeng Wang**, and Yunfeng Ding, “Periodic Antireflection Surface Structures Fabrication on Silicon by Four-beam Laser Interference Lithography”, Journal of Laser Applications 26, 012010 (2014).

4. Wenjun Li, Zuobin Wang, **Dapeng Wang**, Ziang Zhang, Le Zhao, Dayou Li, Renxi Qiu, and Carsten Maple, “Superhydrophobic Dual Micro- and Nanostructures Fabricated by Direct Laser Interference Lithography”, Optical Engineering 53, 034109 (2014).

5. Jia Xu, Zuobin Wang, Ziang Zhang, **Dapeng Wang**, and Zhankun Weng, “Fabrication of Moth-eye Structures on Silicon by Direct Six-beam Laser Interference Lithography”, Journal of Applied Physics 115, 203101 (2014).

6. **Dapeng Wang**, Zuobin Wang, Ziang Zhang, Yong Yue, Dayou Li, and Carsten Maple, “Effects of Polarization on Four-beam Laser Interference Lithography”, Applied Physics Letters 102, 081903 (2013).

7. **Dapeng Wang**, Zuobin Wang, Ziang Zhang, Yong Yue, Dayou Li, and Carsten

Maple, “Direct Modification of Silicon Surface by Nanosecond Laser Interference Lithography”, Applied Surface Science 282, 67 (2013).

8. **Dapeng Wang**, Zuobin Wang, Yong Yue, Juncai Yu, Chunlei Tan, Dayou Li, Renxi Qiu, and Carsten Maple, “Determination of Beam Incidence Conditions Based on the Analysis of Laser Interference Patterns”, International Journal of Light and Electron Optics, submission, 2014.

International conference papers

1. **Dapeng Wang**, Yong Yue, Ziang Zhang, Dayou Li, Carsten Maple, and Zuobin Wang, “Direct Laser Interference Technology and Potential Applications”, International Conference on Manipulation, Manufacturing and Measurement on the Nanoscale (3M-NANO), 2014, Accepted.

2. Ziang Zhang, Zuobin Wang, and **Dapeng Wang**, “Micro-lens Arrays Fabricated by Laser Interference Lithography”, International Conference on Manipulation, Manufacturing and Measurement on the Nanoscale (3M-NANO), 2014, Accepted.

3. **Dapeng Wang**, Yong Yue, Ziang Zhang, Dayou Li, Carsten Maple, and Zuobin Wang, “Anti-reflection Structures Fabricated by Direct Laser Interference Technology under Different Ambiances”, International Conference on Manipulation, Manufacturing and Measurement on the Nanoscale (3M-NANO), pp (82-85), 2013.

4. Le Zhao, Zuobin Wang, **Dapeng Wang**, Ziang Zhang, Zhankun Weng, Carsten Maple, Dayou Li, and Yong Yue, “Silicon Wafer Modification by Laser Interference”, 8th IEEE International Conference on Nano/Micro Engineered and Molecular Systems (NEMS), pp (1236-1239), 2013.

5. **Dapeng Wang**, Zuobin Wang, Ziang Zhang, Yong Yue, Dayou Li, and Carsten Maple, “Modification of Silicon Surface by Direct Laser Interference”, International Conference on Manipulation, Manufacturing and Measurement

on the Nanoscale (3M-NANO), pp (5-8), 2012.

6. Yinbao Lei, Zuobin Wang, Jia Xu, Jinjin Zhang, **Dapeng Wang**, Yu Hou, Yong Yue, and Dayou Li, “Determination of Two-Dimensional Phase Shifts in Three-Beam Laser Interference Patterns”, International Conference on Manipulation, Manufacturing and Measurement on the Nanoscale (3M-NANO), pp (9-13), 2012.

Chapter 2

Fundamental Theories and Methodology

2.1 Basic Concepts

2.1.1 Light Waves and Laser

In physics, the term “light” refers to electromagnetic radiation, whether visible or not. The representative properties of light are intensity, propagation direction, frequency or wavelength spectrum and polarisation. The speed of light is a constant, around 2.99x10^8m/s in vacuum. Generally, many waves can be regarded as a plane wave in a localized region of space. In the 19th century, James Clerk Maxwell concluded that light was a form of electromagnetic radiation and gave a full mathematical description known as Maxwell’s Equations [18]. Based on the Maxwell’s Equations, the plane sinusoidal equation for an electromagnetic wave propagating in the *x* direction is expressed

$$\vec{E}(x,t) = A_0 \cos(k \cdot x - \omega \cdot t + \varphi) \quad , \tag{2.1}$$

where A_0 is the amplitude, k is the wave number and equals $2\pi/\lambda$ (λ is wavelength), x is a point in the x direction, ω is the frequency, t is a given point in time, and φ is the initial phase.

The term "laser" originates as an acronym for light amplification by stimulated emission of radiation. Since laser was invented in 1954, it has been applied for many important applications both in the common consumer devices and the scientific research. The inventors won the Nobel Prize in 1964 for the fundamental work in the field of the construction of oscillators and amplifiers. Basically, lasers are distinguished from other light waves by their monochromatic, directional and coherent properties. Monochromaticity means a definite

wavelength or frequency, while an ordinary white light is a combination of different wavelengths. Laser is emitted in a high direction, by which the pointers, rangefinders and weapons are invented. Coherence enables a stationary interference and is a basis factor for practical applications such as holography, optical coherence tomography and telescope interferometers.

2.1.2 Interference

Interference is a phenomenon in which two or more waves that are coherent with each other to form a resultant wave and the intensities are modulated periodically. In the beginning of the 19th century, people tried to propose many experimental observations to explain the phenomena, including diffraction effects and colours in thin films. Among them, double-slit interference is the most famous experiment demonstrated by Tomas Young in 1803 and it gives a comprehensive understanding of the wave theory of light. To make interference occur, several conditions have to be met:

- Spatial and temporal overlap of the two light fields,
- Coherence of the two light fields,
- Non-orthogonal polarization states.

In fact, any type of single-frequency waves (e.g. light, radio, acoustic and water waves) has the possibility to be observed with interference effect while they overlap. Generally, the ideal interference source is the light which consists of a very narrow spectrum of frequency. Since laser was invented, a wide variety of applications have been developed based on interference principle.

2.2 Classical Interference Theory

In the interference area, the intensity distribution of *N*-beam laser interference can be described as the superposition of electric field vectors of *N* beams and the formula is expressed by [19]

$$I = \left| \sum_{m=1}^{N} \tilde{E}_m \right|^2 = \sum_{m=1}^{N} \sum_{n=1}^{N} \tilde{E}_m \cdot \tilde{E}_n^* = \sum_{m=1}^{N} \sum_{n=1}^{N} A_m A_n \cdot e^{[i(\vec{k}_m \vec{r}_m - \vec{k}_n \vec{r}_n) + \varphi_m - \varphi_n]} . \quad (2.2)$$

where $\tilde{E}_m$ is the complex exponential form of *m*th electric field vector and $\tilde{E}_n^*$ represents the conjugate function of $\tilde{E}_n$, $\vec{k}_m$ is the vector in the propagation direction, $\vec{r}_m$ is the position vector and φ_m is the initial phase.

In Eq. (2.2), $\tilde{E}_m$, $\vec{k}_m$, and $\vec{r}_m$ are expressed by [10, 19]

$$\tilde{E}_m = A_m \cdot e^{[i\vec{k}_m \vec{r}_m - \omega t + \varphi_m]} , \quad (2.3)$$

$$\vec{k}_m = k(\sin\theta_m \cdot \cos\phi_m \cdot \vec{i} + \sin\theta_m \cdot \sin\phi_m \cdot \vec{j} - \cos\theta_m \cdot \vec{k}) , \quad (2.4)$$

$$\vec{r} = x \cdot \vec{i} + y \cdot \vec{j} + z \cdot \vec{k} , \quad (2.5)$$

where A_m is the amplitude, θ_m is the incident angle, ϕ_m is the azimuthal angle, ω is the frequency, t is a given point in time, k is the wave number ($k = 2\pi/\lambda$, λ is wavelength), and $\vec{i}, \vec{j}, \vec{k}$ are unit vectors in Cartesian coordinates.

Take example for two-beam interference, the schematic is shown in Fig. 2.1. The initial laser beam is divided into two beams with the azimuthal angles of $\phi_1 = 0^\circ$ and $\phi_2 = 180^\circ$.

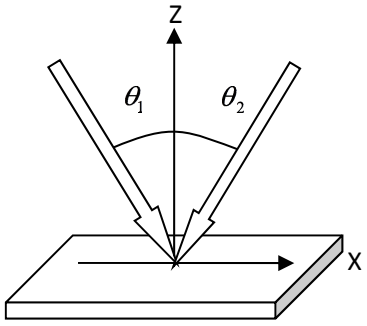

Fig. 2.1 Schematic of two-beam interference.

It is assumed that amplitudes of each beam are identical and initial phases are 0.

According to Eqs. (2.1)-(2.5), the electric field vectors are written as below [19]

$$\left.\begin{aligned}\tilde{E}_1 &= A\cdot e^{[ik(\sin\theta_1\cdot x-\cos\theta_2\cdot z)-\omega t]}\\ \tilde{E}_2 &= A\cdot e^{[ik(-\sin\theta_2\cdot x-\cos\theta_2\cdot z)-\omega t]}\end{aligned}\right\}. \tag{2.6}$$

The intensity distribution of two-beam interference can be concluded [7]

$$I = A^2\left[2-2\cos(2k\sin\theta\cdot x)\right] = A^2\left[2-2\cos(2\pi\frac{2\sin\theta}{\lambda}x)\right]. \tag{2.7}$$

Thus, the period of two-beam interference is determined by $d = \lambda/2\sin\theta$.

2.3 Theories for the Applications

2.3.1 Principle for Anti-reflection

According to the thin-film optics, as shown in Fig. 2.2, the condition to achieve zero reflection is [20]

$$n_{AR-film} = \sqrt{n_1 n_2}\ , \tag{2.8}$$

$$h = \lambda/4\cdot n_{AR-film}\ , \tag{2.9}$$

where $n_{AR\text{-}film}$ is the refractive index of the media of the antireflection coating, n_1 and n_2 are the refractive indices of the ambient and solid media (n_1≈1 in air), respectively, h is the thickness of the coating, and λ is the wavelength.

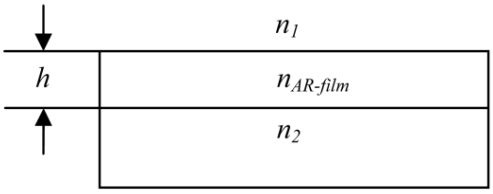

Fig. 2.2 Sketch of an antireflection film.

When the period of structures is shorter than the wavelength of incident light,

the sub-wavelength structures can be regarded as an anisotropic optical thin film with an effective refractive index. Based on the effective medium theory, the effective refractive index (n_{eff}) can be expressed as [21]

$$n_{\text{eff}} = (1-\sigma_n)^2 n_1 + \sigma_n^2 n_2 \quad , \tag{2.10}$$

$$\sigma_n = W_n / P \quad , \tag{2.11}$$

where W_n is the width of structures and P is the period.

As shown in Fig. 2.3, microcone structures have a slope from the top to the bottom, and they show a partial similarity to numerous effective medium layers. The reflection from the visible to infrared wavelengths can be suppressed by the effective multi-layers with the gradient refractive indices.

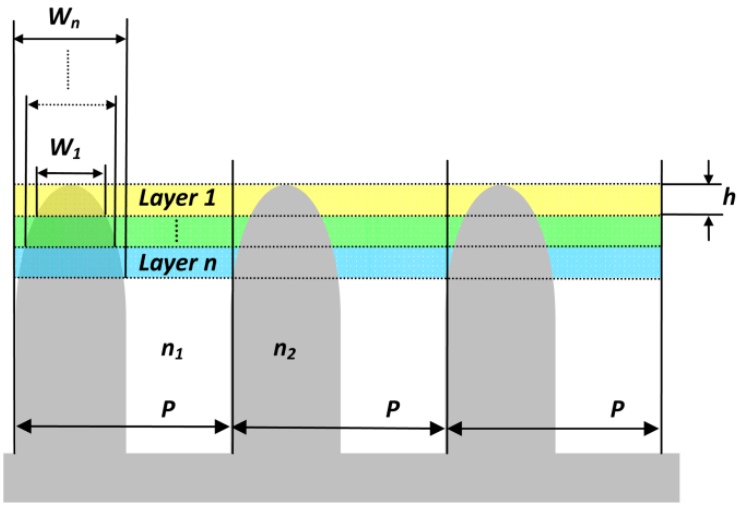

Fig. 2.3 Sketch of sub-wavelength structures with effective medium layers.

In practice, the incident energy is lost both through external reflection on a polished wafer surface and through scattering by surface nano structures, while the textured surface does absorb more energy through multiple internal reflections and refractions. Compared with the effective medium theory, the increase of surface area because of the convex and concave structures can be attributed to another light-trapping mechanism. Fig. 2.4 shows schematically

how radiation is trapped by multiple reflections at both the outer and inner walls of a surface structure.

As an emerging candidate, another novel nanostructures, namely surface plasmons (SPs) have attracted much attention due to high absorption or light-trapping performance [22]. The underlying mechanism of SPs can be attributed to confine the collective oscillations of photonics locally by metal nanostructures. Subwavelength metallic nanostructures can couple propagating light freely into a thin absorbed layer. But SPs are excited only in the case of the frequency of the incident photons matches the resonance frequency of metal nanoparticles. Their resonance wavelength is dependent on the three-dimensional sizes and the dielectric parameters of the surrounding environment [23]. Thus, different approaches are subjected to fabricate various feature sizes of nanostructures. Surface plasmon resonance in nanometre-sized structures is called as localized surface plasmon resonance (LSPR). Due to the high absorption of LSPR for a broad spectral band and a wide angular range of incidence with polarisation insensitivity, it has been proved to be a promising material for effective absorption in thin-film solar cells [24].

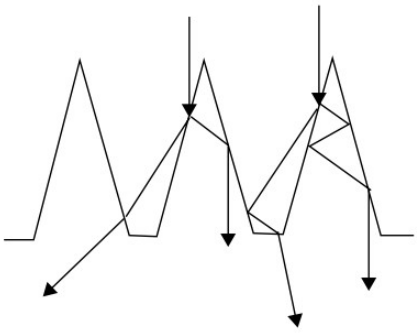

Fig. 2.4 Sketch of light trapping through multiple reflections.

2.3.2 Principle for Self-cleaning

The lotus leaf has the self-cleaning function which can pick up the dirty and dust particles by water droplets due to a complex micro and nano scale architecture of the surface and the waxy crystal [25, 26]. Previous studies have also investigated

the unique property of the superhydrophobic surface is attributed to the micro and nano structure [5, 27-30]. Superhydrophobic surfaces with a high static Contact Angle (CA) above 150° exhibit excellent repellence and self-cleaning properties. The CA is formed by a liquid at the three phase contact line where the liquid, vapour and solid intersect. The drop shape is controlled by the three forces of interfacial tension shown in Fig. 2.5. The CA is a quantitative measure of the wetting of a surface by a liquid. The wettability can be explained with Young equation [31]

$$\cos\theta_0 = \frac{\gamma_{S/V} - \gamma_{S/L}}{\gamma_{L/V}} \quad , \tag{2.12}$$

where θ_0 is the Yong CA, $\gamma_{S/V}$ is the solid/vapour interfacial free energy, $\gamma_{S/L}$ is the solid/liquid interfacial free energy, and $\gamma_{L/V}$ is the liquid/vapour interfacial free energy.

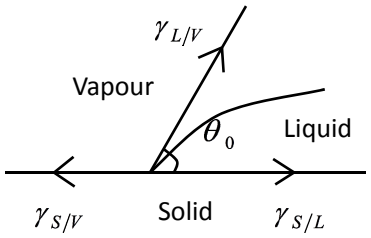

Fig. 2.5 A liquid drop showing the quantities in Young equation.

Young equation is valid in the case of a flat solid surface. The Wenzel model is used in the case of a rough surface that changes the contact angle. The Wenzel state is defined by the following Eq. (2.13) for the contact angle on a rough surface [32]

$$\cos\theta = R_f \cos\theta_0 \quad , \tag{2.13}$$

where θ is the apparent contact angle which corresponds to the stable equilibrium state. R_f is the roughness factor which is a measure of how surface roughness affects a homogeneous surface. The roughness factor is defined as the

ratio of the solid-liquid area to its projection on a flat plane. θ_0 is the Young contact angle defined for a perfect flat surface.

The Wenzel model is not sufficient to deal with a heterogeneous surface. A more complex model is needed to measure the apparent contact angle on composite surfaces. This heterogeneous surface is explained by the Cassie–Baxter model, illustrated in Fig. 2.6, and the equation is written as [33]

$$\cos\theta = \psi_L \cos\theta_1 + \psi_A \cos\theta_2 \quad , \tag{2.14}$$

where θ_1 and θ_2 are the contact angles of the flat solid and air surfaces, respectively. ψ_L and ψ_A are the solid and air surface area fractions of the solid and air, respectively. When the contact angle of the air film is 180° and $\psi_L + \psi_A = 1$, Eq. (2.14) can be rewritten as [33]

$$\cos\theta = \psi_L(\cos\theta_1 + 1) - 1 \quad . \tag{2.15}$$

It is known from Cassie-Baxter that two criteria must be necessary to meet the condition of hydrophobicity: a contact line density criterion and asperity height criterion. The thickness of the air pocket has an effect on gathering the water droplet [34].

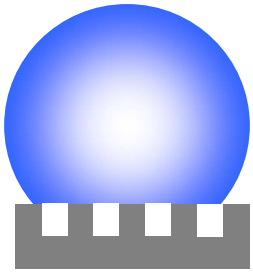

Fig. 2.6 Typical Cassie-Baxter model for wetting behaviour of a water droplet on the rough solid substrate.

One of the ways to improve the hydrophobicity of the surface is to increase its roughness, and the roughness surface fabrication has become a subject to be investigated. The roughness has been used to assess the wettability in order to

design the superhydrophobic surface [35]. The fundamental theories described in section 2.3 are a basis for chapter 6 which focuses on the applications.

2.4 Methodology in the Thesis

In the thesis, effects of polarisation vector on the interference patterns are presented and studied as it is found that polarisation has a strong influence on contrast, period and formation of interference patterns. Through the integration of polarisation vector and electric field vector, the theory of multi-beam interference is developed and implemented throughout research strategy. Based on them, theoretical analyses of interfering distributions in the two-, three- and four-beam interference are studied systematically. Meanwhile, Matlab is employed to simulate the patterns and verify the results.

The polarisation vector is defined as $\vec{p}_m$. It's well known that the electric field vector, the propagating direction, and the polarisation vector are perpendicular with one another and based on the theory of solid geometry, the expression of polarisation vector can be inferred by Eq. (2.16) in terms of incident, azimuth and polarised angels.

$$\begin{aligned}\vec{p}_m = &-(\cos\theta_m \cdot \cos\phi_m \cdot \cos\psi_m - \sin\phi_m \cdot \sin\psi_m)\cdot \vec{i} \\ &-(\cos\theta_m \cdot \sin\phi_m \cdot \cos\psi_m + \cos\phi_m \cdot \sin\psi_m)\cdot \vec{j} \\ &-(\sin\theta_m \cdot \cos\psi_m)\cdot \vec{k}\end{aligned}, \qquad (2.16)$$

where ψ_m is the polarised angle. Consequently, the formulation of intensity distribution is rewrote as below

$$I(r) = \sum_{m=1}^{N} \vec{E}_m \cdot \sum_{n=1}^{N} \vec{E}_n^* = \sum_{m=1}^{N}\sum_{n=1}^{N} A_m \vec{p}_m \cdot A_n \vec{p}_n \cdot e^{[i(\vec{k}_m - \vec{k}_n)\vec{r} + \varphi_m - \varphi_n]} \quad . \qquad (2.17)$$

The Eqs. (2.16) and (2.17) derived in a new form are two fundamental formulations which contribute to the theory of physical optics. According to the

Eqs. (2.16) and (2.17), the period, contrast and intensity peaks can be obtained in the multi-beam interference. In the following chapters, it is on the basis of Eqs. (2.16) and (2.17) that a series of theoretical analyses are implemented in a detailed way.

In the experimental study, DLIN is applied to carry out the fabrication of periodic micro and nano structures on various materials surface. Compared with traditional LIL, DLIN utilises a nanosecond pulsed laser source. The energy distribution modulated by coherent beams is transferred to the material surfaces as a result of producing periodic structures directly. Without the need of pretreatment, mask and pattern transfer processes, DLIN is a facile, rapid and cost-effective technology. The framework of methodology in the thesis is shown in Fig. 2.7.

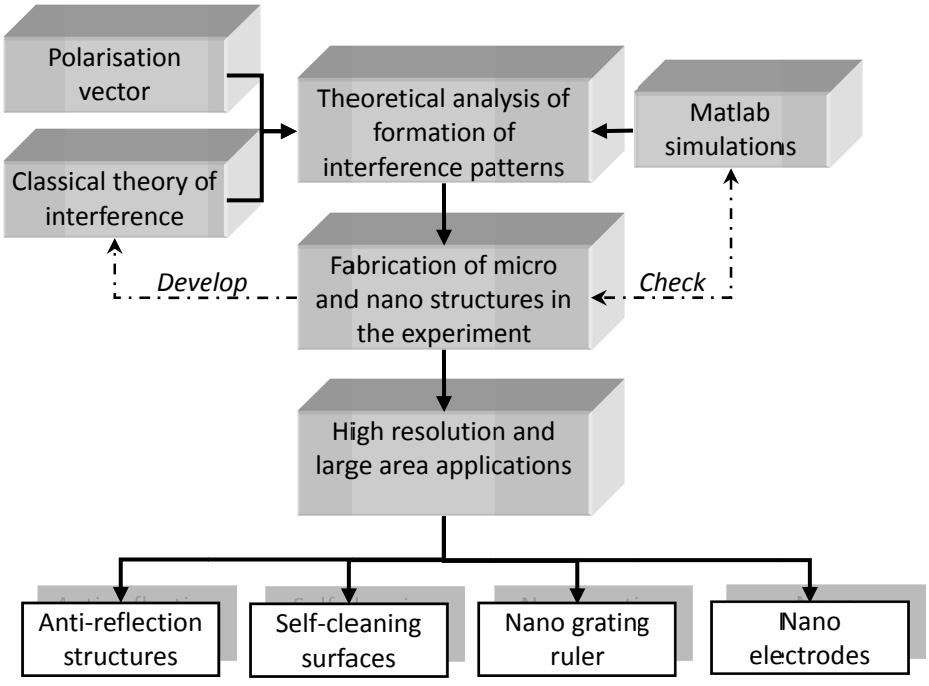

Fig. 2.7 Framework for research methodology.

DLIN is developed in order to realise a number of innovative and multifunctional applications. In the thesis, the potential applications, such as anti-reflection structures of solar cells, self-cleaning surfaces, high-resolution nano gratings and nanoelectrodes arrays, are explored experimentally. Among them, the periodic

microcone structures with a huge number of nano features on the surface were fabricated by the developed four-beam interference with the designed polarisation mode.

Benefiting from the methodology, the internal links between the chapters are well established. They are revealed in views of the experimental simulations, theoretical analyses and applications respectively. Chapter 3 firstly studies the multi-beam imaging interference system for the experimental simulations. Two-beam interference systems, or named as interferometers are the traditional interfering instrument for the high precision measurement. Compared with them, the system setup in the work breaks the limitation of number of interfering beams. A number of novel outcomes, e.g. dual-periodic structure patterns, are found by means of the system. Besides the theoretical demonstrations and computer simulations, the experimental simulations for studying the formation of interference patterns are of great importance to display the influence of parameters in real-time. Subsequently, chapters 4 and 5 are to implement the theoretical analyses systematically. The principal objective of chapter 4 is to fabricate the well-defined structures whose formations show a good agreement with regard to the theoretical derivations and additionally discuss the thermal effect of nanosecond laser on the solid matter. The experimental aspects are related to the two-, three- and four-beam interference configurations. In contrast with previous publications, it is found that the modulation phenomenon of four-beam interference is brought about only in the case of TE-TE-TM-TM polarised mode. Chapter 5 inserted individually does give a detailed explanation of the effects of polarisation vector. In the following chapters 6 and 7, the large-area and high-resolution applications are explored finally. Inspired the experimental results in chapter 5, a developed method for the fabrication of both superhydrophobic and antireflection functional structures is proposed in chapter 6. It is worth mentioning that DLIN offers an unprecedented way to achieve two functions at the same time in a high-efficiency manner. As for the high-resolution application, the organic material is selected as the research object in chapter 7 by

referring to previous work for the influence of thermal conductivity is obvious during the laser modification and meanwhile the strategy of exploiting the best contrast configuration in two-beam interference case is applied to improve the structural feature sizes. Thus, the methodology focuses into the integrity throughout the whole thesis.

2.5 Summary

In the chapter, a number of basic concepts in the physical optics, the conventional theory of interference and the principles for applications are introduced. Although people know Young's (double-slit) experiment and the period of two-beam interference well, the effects of other parameters, e.g. the polarisation vector and the azimuthal vector, on the distribution, period and contrast in multi-beam interference are complicated and inexplicable. The existing works generally focus on applications by using interference technology but neglect the analysis of theoretical formulation. In fact, the interference patterns are the combination of a number of vectors and any one of them has a strong influence of resulting distribution. To overcome the problem specially, the methodology is addressed in section 2.4. With the help of the methodology, the theoretical analysis and experimental results show a good correspondence, which demonstrates that the derived theoretical formulations reveal the interfering characterisation in nature.

With the investigation of classical theory of interference, there is still a lack of theoretical analysis of polarisation vector in multi-beam interference. For a given configuration of interference system, the formation of interfering patterns is complicated and unpredictable without the detailed analysis. In the thesis, effects of polarisation vector on the interference patterns are studied and the formulations of multi-beam interference cases are derived on a basis of polarisation vector. It is also worth pointing out that the theoretical analysis of polarisation gives an explanation for the modulation phenomenon in the

four-beam interference. Furthermore, the study for the effects of polarisation on interference is constructive to carry out the following experiments as well. In the subsequent chapters, different polarisation modes are selected to fabricate various micro and nano structures and realise a number of significant applications.

Chapter 3

He-Ne Laser Interference and Imaging System

3.1 Introduction

In this chapter, the He-Ne laser interference imaging system is introduced. Compared with LIL and DLIN whose fabricated structures are observed by scanning electron microscope (SEM) or atomic force microscope (AFM), the He-Ne laser interference system takes the advantage of real-time imaging and can contribute to visual feedback on micro and nano scales. The investigation of multi-beam laser interference is a complex and challenging problem from a book-keeping perspective due to the additional field. Although computer software can simulate the formation of interference patterns, there are also a number of offsets which deviate a little from theoretical conditions in practice. Principal motivation is to better understand the formation of interference patterns and analyse different incidence conditions with the combination of image processing method.

It is known that the period of interference can be controlled by changing the incident angles of beams or the radiation wavelength. For practical applications, the wavelength is first selected so that the period depends on the incident angles. Meanwhile, the influences of polarised angles, azimuth angles and number of beams are also extremely important for obtaining desired interference patterns since the spatial distributions of interfering beams are a function of the mentioned parameters. In the case of two-beam laser interference, different incidence conditions introduced by the polarisation vectors result in different contrasts [36]. In the case of three-beam laser interference, the modulation period is produced in the coplanar incidence conditions, and in the case of four-beam interference, there are three different types of patterns produced by polarisation modes. To determine the relationship between the beam incidence conditions

and interference patterns, a series of steps, including image acquisition, processing and analysis based on the theory of physical optics, were taken to achieve high precision measurements.

A number of approaches for the period measurement were addressed by the previous publications. Wang et al. presented a method of displacement measurement based on Young's experiment at the early stage. The displacement or period was determined according to the 100×152 pixels image patches obtained from a fiber-optic interferometer by using fringe pattern matching and the polynomial curve fitting methods. It was shown that the simulation and experiment results demonstrated a subpixel resolution of measurement [37]. Subsequently, Ji et al. took in deep investigation of quality inspection and applied Hough Transform (HT) and Maximum Likeihood Estimation (MLE) methods to detect nanoscale patterns produced by LIL. It was found that the HT method is invalid to deal with the patterns of strong noises and a statistical method based on the MLE could estimate each circle's centre and shape [38]. In order to resist the noises, Liu et al. presented a method of fringe pattern correlation. In the method, the phase difference between any two fringe patterns is determined by the method. Meanwhile, several types of noise such as Gaussian noise, salt and pepper noise, and speckle noise were added to the fringe patterns. It was demonstrated that the fringe pattern correlation had the advantages of high precision and high resistance to noise [39]. Compared with perpendicular fringes, the cross-correlation function has been developed to measure the oblique fringes and determine the slope [40].

The measurement of period is a premise for calculating the incident angles and the detailed analyses of the formation of three and four-beam interference play a critical role in the determination of beam incident conditions. Any slight change of incident angles or intensities of beams will introduce significant variations of periods and contrasts of interference patterns. However, there has been no published work on the subject. To deal with the challenging problem,

interference patterns were captured by a He-Ne laser interference system under different incidence conditions, the pattern period measurement was achieved by cross-correlation function, and the pattern contrast was calculated by image processing. Subsequently, the incident angles and intensities of beams were determined based on the analysis of spatial distributions of interfering beams. As a consequence, the relationship between the beam incidence conditions and interference patterns is revealed.

3.2 Imaging System Setup

In the experiment, the He-Ne laser (CVI Melles Griot, 25-LHP-213) with the wavelength of 633nm and output power of 0.5mw was used for the LIL imaging system. This laser source takes advantages of good beam quality and 30cm coherence length. To perform real-time imaging, a CCD camera (PiontGrey, CMLN-13S2M-CS) replaces the exposed sample and a 20× Galilean beam expander (BE) is fixed before the camera as the period of interference is far smaller than the CCD pixel size.

3.2.1 Two-beam Laser Interference

From Fig. 3.1 shown, the laser source was divided into two coherent beams by beamsplitters (BS) and high reflection (HR) mirrors. To control the power and polarised angles of each beam precisely, half-wave plates and polarisers were placed before the CCD. The azimuthal angles are ϕ_1=0˚, ϕ_2 =180˚. Two light paths can be seen as:

(1) laser→BS_1→HR_1→BE→CCD;

(2) laser→HR_3→HR_2→BE→CCD.

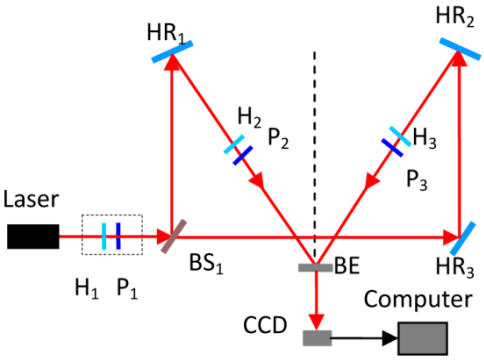

Fig. 3.1 Schematic set-up for two-beam He-Ne laser interference.

3.2.2 Three-beam Laser Interference

In the three-beam interference, there are two cases of non-coplanar and coplanar conditions. From Fig. 3.2 shown, the laser source was divided into three coherent beams by beamsplitters (BS) and high reflection (HR) mirrors. In the non-coplanar condition, the azimuthal angles are ϕ_1=0˚, ϕ_2 =120˚, and ϕ_3 =240˚. Three light paths can be seen as:

(1) laser→BS_1→HR_1→BE→CCD;

(2) laser→BS_2→HR_5→HR_2→BE→CCD;

(3) laser→HR_4→HR_3→BE→CCD.

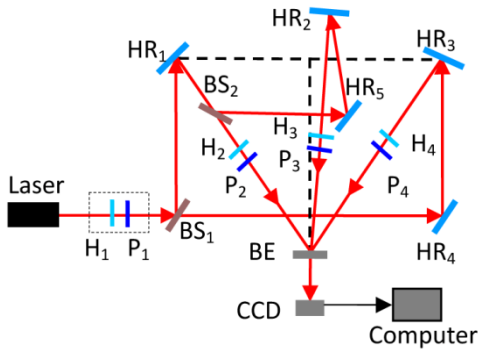

Fig. 3.2 Schematic set-up for non-coplanar three-beam He-Ne laser interference.

From Fig. 3.3 shown, the laser source was divided into three coherent beams by beamsplitters (BS) and high reflection (HR) mirrors. In the coplanar condition, the azimuthal angles are ϕ_1=0˚, and ϕ_2 =ϕ_3 =180˚. Three light paths can be seen as:

(1) laser→BS_1→HR_1→BE→CCD;

(2) laser→BS_2→BE→CCD;

(3) laser→HR_2→BE→CCD.

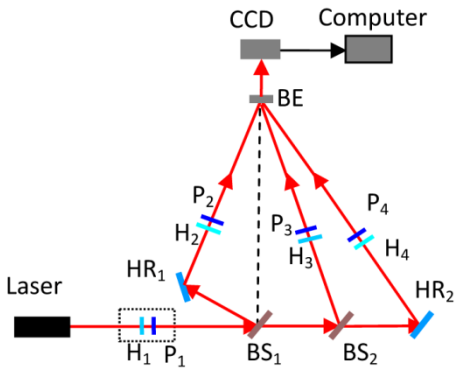

Fig. 3.3 Schematic set-up for coplanar three-beam He-Ne laser interference.

3.2.3 Four-beam Laser Interference

From Fig. 3.4 shown, the laser source was divided into four coherent beams by beamsplitters (BS) and high reflection (HR) mirrors. The azimuthal angles are ϕ_1 =0˚, ϕ_2 =90˚, ϕ_3 =180˚, and ϕ_4 =270˚. Four light paths can be seen as:

(1) laser→BS_1→HR_1→BE→CCD;

(2) laser→BS_1→HR_1→BS_2→HR_2→BE→CCD;

(3) laser→HR_4→HR_3→BE→CCD;

(4) laser→HR_4→HR_3→BS_3→HR_5→BE→CCD.

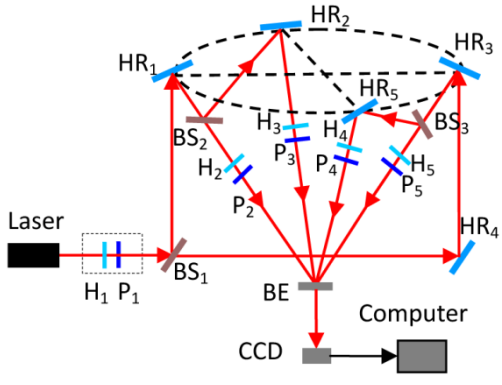

Fig. 3.4 Schematic set-up for four-beam He-Ne laser interference.

3.2.4 Dual Periodic Patterns Achieved by Multi-beam Laser Interference

Since the LIL was proposed, people extensively employed the two-, three- or four-beam laser interference systems in a conventional way to produce periodic dot and line patterns [41-43]. However, few efforts are devoted to explore special configurations of interference system. A number of surprising phenomena are neglected actually. Herein, in order to achieve dual periodic patterns, two developed systems are addressed.

From Fig. 3.5 shown, the well-designed four-beam laser interference is developed. A grating with periodic dots pattern will be generated in this case. The dual periodic patterns or structures have a number of exceptional abilities. The relevant simulation and experimental results are showed in the following sections.

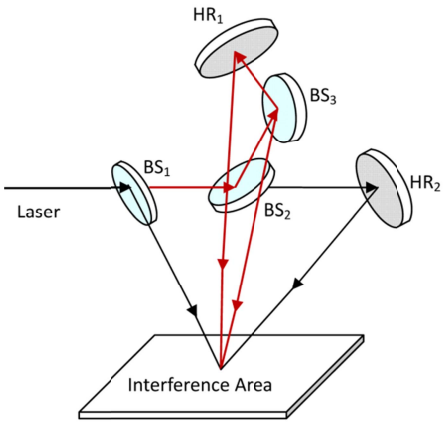

Fig. 3.5 3D schematic of the four-beam laser interference.

In addition, from the nature inspired, people have explored a number of biomimetic structures by means of micro and nano technologies. With respect to the existing technologies, the fabrication of dual periodic structures probably depends on a series of writing procedures as a result of the technological nature. However, utilising the multi-beam interference method could generate an array of extraordinary patterns directly. The specific schemes which enable to the special patterns are innovative in terms of optics.

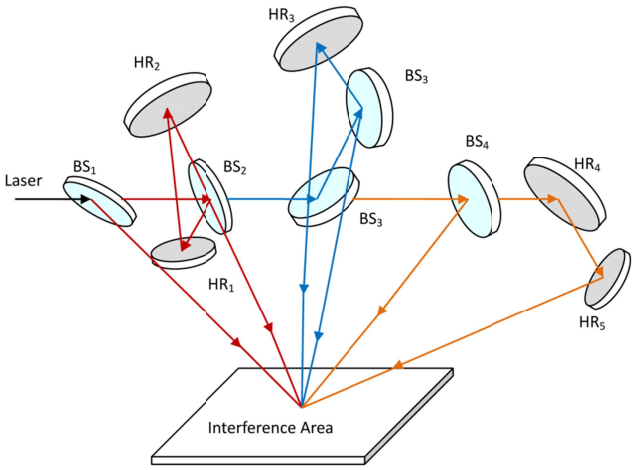

Fig. 3.6 3D schematic of the six-beam laser interference.

Herein, the number of coherent beams is expanded to six and an extraordinary interference pattern is obtained experimentally. The schematic of the six-beam laser interference is shown in Fig. 3.6. As for the special patterns, the He-Ne interference system shows a significant advantage of visualisation of undiscovered interfering conditions. Besides the two examples illustrated in Fig. 3.5 and 3.6, there are a lot of well-deigned conditions which could produce more insights to the multi-beam interference.

3.3 Experimental Results of Imaging System and Matlab Simulations

In the experiment, various interference patterns were captured by the CCD camera and Matlab was employed to simulate the corresponding distribution of interfering beams. From Fig. 3.7 shown, two-, three- and four-beam interference images show a good agreement with Matlab simulations.

Matlab is a powerful tool for the simulation of interference modelling. From the theoretical perspective, the resulting patterns are largely dependent on a number of physical parameters, i.e. the number of beams, wavelength, incident angles, azimuth angles, polarised angles and relative phases, and meanwhile show an extreme sensitivity to the slight variation of these parameters. The untraceable task will benefit from the visualisation of Matlab. For a fixed

configuration, the parameters can be set as the exact values in accordance with the experiment and then Matlab can help calculate 2D or 3D distribution. By varying the designed value, the optimised adjustment can be obtained. In addition, the method also suits to analyse the special cases which are difficult to attain in practical terms, for example six or more beams interference.

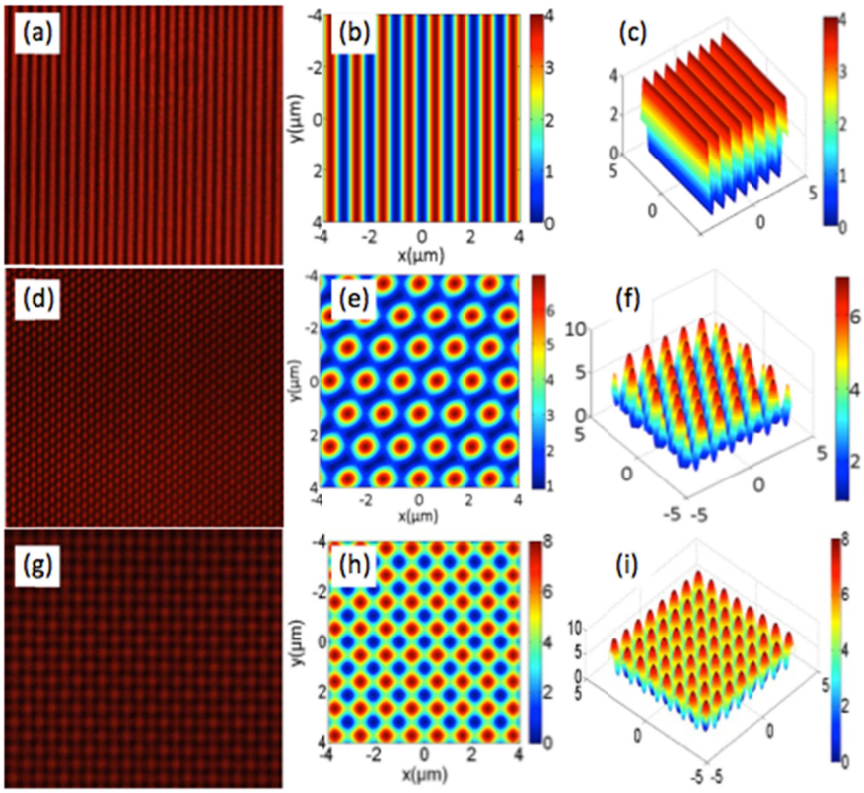

Fig. 3.7 Experimental results of He-Ne laser interference and imaging system vs. Matlab simulations. (a) Two-beam interference CCD image; (b) Corresponding 2D and (c) 3D intensity profiles simulated by Matlab; (d) Three-beam interference CCD image; (e) Corresponding 2D and (f) 3D intensity profiles simulated by Matlab; (g) Four-beam interference CCD image; (h) Corresponding 2D and (i) 3D intensity profiles simulated by Matlab.

The dual periodic patterns produced by the designed four- and six-beam laser interference techniques are shown in Fig. 3.8. It is worth pointing out that the six-beam interference pattern has a high similarity with the surface of *Rosa sinensis* petal [44]. The biomimetic structures can supply us with examples to understand the relationship between surface structures and surface properties (e.g. superhydrophobicity, high adhesive force and structural colour).

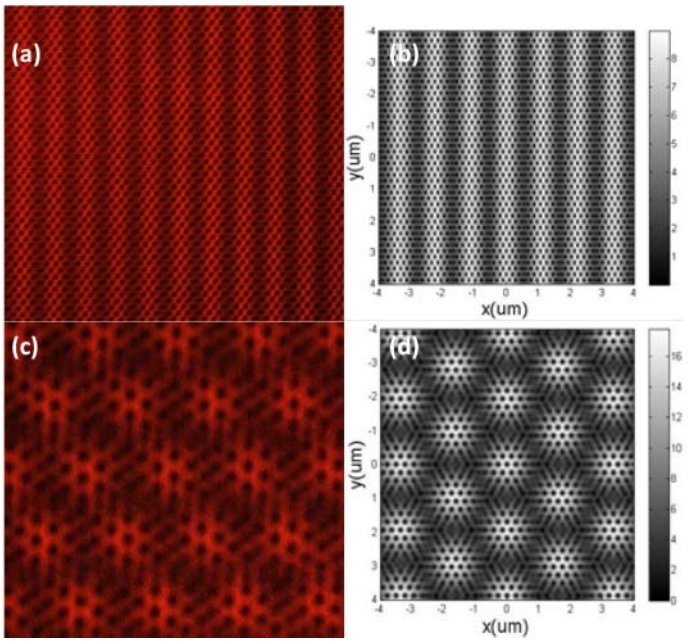

Fig. 3.8 Dual periodic patterns vs. Matlab simulations. (a) The four-beam interference image and (b) corresponding intensity profiles simulated by Matlab; (c) The six-beam interference image and (d) corresponding intensity profiles simulated by Matlab.

3.4 Image Processing for Period and Contrast Measurements

In order to determine the period of the interference patterns, two patches of interference patterns are selected as the fixed and reference image patches. It can be calculated that the fixed patch matches with the reference patch by means of the cross-correlation coefficient which represents the similarity numerically. The schematic of this algorithm is shown in Fig. 3.9(a). The correlation coefficient, ρ_{XY} , between two matrices from the two image patches X and Y is defined as [39]

$$\rho_{XY} = \frac{\mathrm{cov}(X,Y)}{\sigma_X \sigma_Y} = \frac{E[(X-\mu_X)(Y-\mu_Y)]}{\sigma_X \sigma_Y} \quad , \tag{3.1}$$

where *E* is the expected value, *cov* is the covariance, μ_X and μ_Y are the mean values of *X* and *Y*, and σ_X and σ_Y are the standard deviations.

According to the theory of optics, the interference contrast is defined as [7, 11]

$$K = \frac{I_{max} - I_{min}}{I_{max} + I_{min}}, \tag{3.2}$$

where I_{max} and I_{min} are the maximum and minimum interference intensities. For the calculation of contrast, the pattern is divided into N patches or regions. The pattern contrast can be calculated by extracting the maximum and minimum grey-scale values in every selected patches or regions firstly and then averaged the contrast values of the whole image. Fig. 3.9(b) illustrates the schematic of this algorithm.

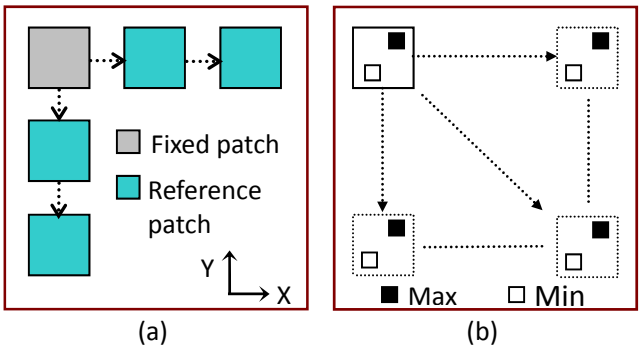

Fig. 3.9 The schematic of image processing algorithms. (a) Principle of determining the period by pattern correlation; (b) Principle of determining the contrast.

All the equations from (3.3) to (3.12) in this chapter are derived on a basis of Eqs. (2.16) and (2.17) and simultaneously refer to the previous work [11, 18-19]. More details of the methodology can be seen in section 2.4. In the two-beam laser interference, a periodic fringe pattern is produced with the incident angles of $\theta_1 = \theta_2 = \theta$, the azimuthal angles of $\phi_1 = 0°$ and $\phi_2 = 180°$, and the polarised angles of $\psi_1 = \psi_2 = 90°$, the intensity distribution can be expressed by

$$I_{two-beam} = A_1^2 + A_2^2 - 2A_1A_2\cos[k(\sin\theta_1 + \sin\theta_2)x]. \tag{3.3}$$

It can be seen from Eq. (3.3) that the period of the interference pattern is $d = \lambda/2\sin\theta$ in the case of the symmetrical two-beam incidence. Fig. 3.10(a) is the fringe pattern obtained by the CCD camera. The pixel number of phase shifts is 29.577 in Fig. 3.10(b). The pixel size of the CCD is 3.75μm, and the measured

period of the interference pattern is 5.546μm. In the experiments, the incident angles were set as θ_1=θ_2=3.3°, which resulted in the period of 5.498μm theoretically. It is found that the offset between the designed angles and the measured angles is 0.03°. Moreover, with the calculation of the contrast, the intensity of each beam can be determined. The maximum and minimum grey-scale values are extracted from the 96×128 pixels patches which shift in the whole interference pattern. The final value is obtained by averaging all the contrasts with the shifting step of 10 pixels from the row and column directions. According to Eqs. (3.2) and (3.3), in this case, *K* can be written as

$$K_{two-beam} = \frac{2A_1A_2}{A_1^2 + A_2^2} \quad , \tag{3.4}$$

and the calculation result is 0.87. It can be concluded that the amplitude of one beam is 1.7 times higher than that of the other one.

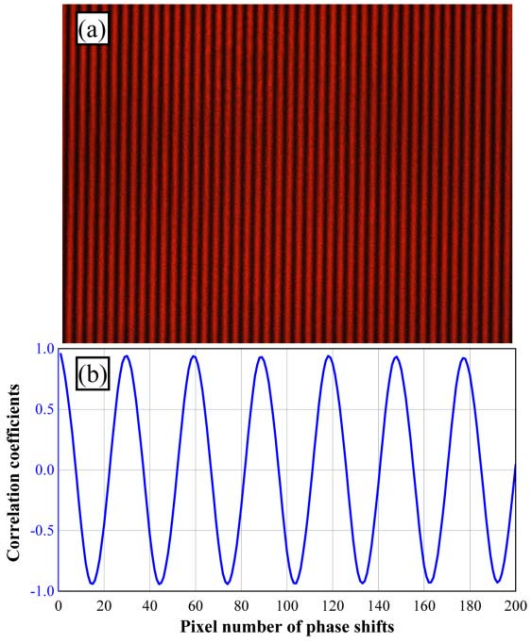

Fig. 3.10 (a) The CCD image of the two-beam laser interference; (b) Corresponding correlation coefficients as a function of phase shifts.

In the cases of three-beam laser interference, there are generally two different configurations corresponding to coplanar and non-coplanar incidence conditions.

The triangle distribution pattern is generated by the non-coplanar incidence condition while the dual-grating pattern is generated by the coplanar incidence condition, as shown in Fig. 3.11. In the non-coplanar incidence condition, the three beams have the same incident angles of $\theta_1 = \theta_2 = \theta_3 = \theta$, and the azimuthal angles of 30°, 150° and 270°. In the coplanar incidence condition, the incident angles of three beams are $\theta_1 = \theta_2 = \theta, \theta_3 = \theta^*$ ($\theta^* > \theta$), and the azimuthal angles are, $\phi_1 = \phi_2 = 0°$ and $\phi_3 = 180°$.

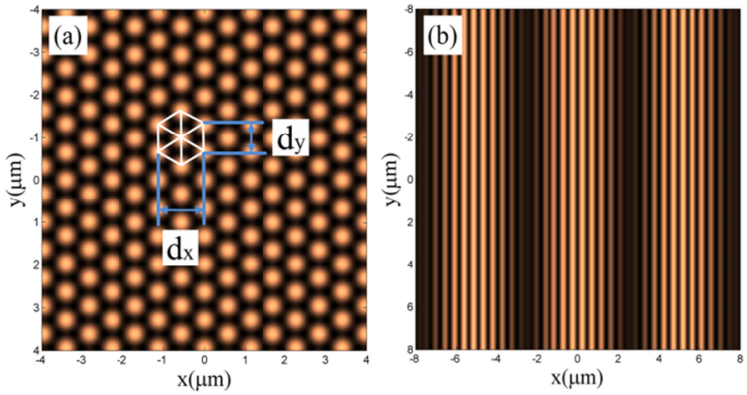

Fig. 3.11 2D simulations of three-beam interference distributions. (a) Non-coplanar incidence condition; (b) Coplanar incidence condition.

According to Eqs. (2.4), (2.5), (2.16), and (2.17), when the polarised angles are 0°, the equation of the three-beam interference in the non-coplanar incidence condition is expressed as below

$$\begin{aligned} I_{three-beam} = {} & A_1^2 + A_2^2 + A_3^2 + \Delta \cdot A_1 A_2 \cos(k\sqrt{3}\sin\theta \cdot x) \\ & + \Delta \cdot A_1 A_3 \cos(k\frac{\sqrt{3}}{2}\sin\theta \cdot x + k\frac{3}{2}\sin\theta \cdot y) \\ & + \Delta \cdot A_2 A_3 \cos(k\frac{\sqrt{3}}{2}\sin\theta \cdot x - k\frac{3}{2}\sin\theta \cdot y) \end{aligned}, \quad (3.5)$$

where $\Delta = 2\sin^2\theta - \cos^2\theta$. It can be seen that the period in the x direction is expressed as

$$d_x = 2\lambda / \sqrt{3}\sin\theta, \quad (3.6)$$

and the period in the y direction is

$$d_y = 2\lambda/3\sin\theta \quad . \tag{3.7}$$

This means that the period in the x direction is $\sqrt{3}$ times larger than the other one, which shows a good correspondence with the simulation in Fig. 3.11(a). Thus, the three-beam laser interference method is able to generate the triangle or hexagon distribution pattern.

The triangle pattern shown in Fig. 3.12(a) was obtained experimentally. Fig. 3.12(b) indicates that the respective pixel numbers of phase shifts in the x and y directions are unequal. According to the results of the correlation coefficient calculations, the measured period in the x direction is d_x=7.854μm and the measured period in the y direction is d_y=4.401μm. The relationship of the ideal pattern is $d_x/d_y = \sqrt{3}$ and the relationship of the experimental result is $d_x/d_y = 1.785$. It is demonstrated that the misalignment of the azimuthal angles causes a minor offset of 0.74° between the designed angles and the measured angles. Unlike the two-beam interference, the contrast of the three-beam interference in the non-coplanar incidence conditions is determined by the amplitude of each beam and has an effect on the incident angles. The contrast in this case is expressed as

$$K_{three-beam} = \Delta \cdot \frac{A_1A_2 + A_1A_3 + A_2A_3}{A_1^2 + A_2^2 + A_3^3} . \tag{3.8}$$

To calculate the contrast, the incident angle needs to be determined first. As Fig. 3.12(b) and Eq. (3.5) suggested, the incident angle is 5.3°, so $\Delta = 0.9744$. Meanwhile, the contrast is calculated by the image processing method which is used in the two-beam interference and the result is 0.9706. Thus, it is demonstrated that the amplitudes are almost equal with each other.

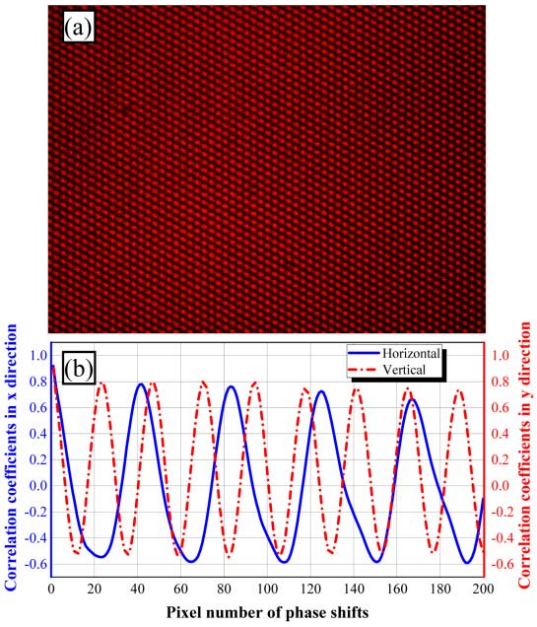

Fig. 3.12 (a) The CCD image of the three-beam laser interference in the non-coplanar incidence condition; (b) Corresponding correlation coefficients in x and y directions as a function of phase shifts.

When the azimuthal angles of three beams are in the same plane, a dual-grating structure pattern is produced. In the experiment, the initial laser beam was divided into three beams with the azimuthal angles of $\phi_1 = \phi_3 = 0°$ and $\phi_2 = 90°$, the polarised angles of $\psi_1 = \psi_2 = \psi_3 = 90°$, and the incident angles of $\theta_1 = \theta_2 = \theta$ and $\theta_3 = \theta^*$ ($\theta^* > \theta$). In this case, the intensity of interference $I'_{three\text{-}beam}$ is expressed as

$$\begin{aligned} I'_{three-beam} &= A_1^2 + A_2^2 + A_3^2 - 2A_1A_2\cos(2k\sin\theta \cdot x) \\ &+ 2A_1A_3\cos[(\sin\theta - \sin\theta^*)x - (\cos\theta - \cos\theta^*)z] \\ &- 2A_2A_3\cos[(\sin\theta + \sin\theta^*)x + (\cos\theta - \cos\theta^*)z] \end{aligned} \quad (3.9)$$

Eq. (3.9) indicates that the intensity of interference is a function of the coordinates in the x and z directions. Generally, the interference is deemed to occur in the xy plane. This means that the value of z is zero, so there are three interference terms in the x directions. They are expressed as

$$\begin{cases} d_1 = \dfrac{\lambda}{2\sin\theta} \\ d_2 = \dfrac{\lambda}{\sin\theta + \sin\theta^*} \\ d_3 = \dfrac{\lambda}{\left|\sin\theta - \sin\theta^*\right|} \end{cases}. \tag{3.10}$$

In practice, θ^* and θ are approximately equal with each other, consequently, d_1 and d_2 are approximately equal, and d_3 is larger than them ($d_1 \approx d_2$, $d_3 >> d1$). Thus, it is the reason that the interference pattern exhibits dual periods. Fig. 3.13 shows the experimental result. From the curve in Fig. 3.13(b), the periods are calculated as d_1=3.5625μm, d_2=3.1875μm and d_3=27.5625μm. According to the values and Eq. (3.10), the incidence conditions can be determined, and they are θ=5.1˚ and θ^*=6.3˚±0.3˚.

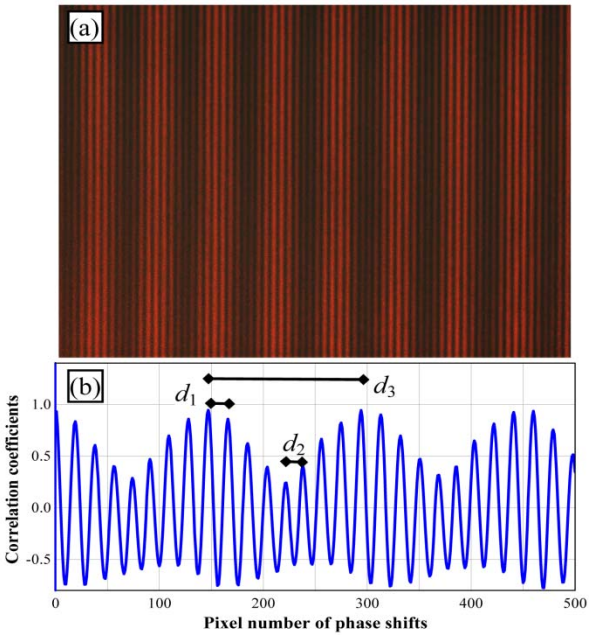

Fig. 3.13 (a) The CCD image of the three-beam laser interference in the coplanar incidence condition; (b) Corresponding correlation coefficients as a function of phase shifts.

In this case, the contrast is expressed as

$$K'_{three-beam} = \frac{A_1A_2 + A_1A_3 + A_2A_3}{A_1^2 + A_2^2 + A_3^3}. \tag{3.11}$$

and the calculation result is 0.734. The decrease of contrast could be caused by the unequal amplitudes of each beam.

The four beams follow a symmetrical configuration with the azimuthal angles of 0°, 90°, 180° and 270°. The polarisation angles of four beams were 90°. It can be seen in Fig. 3.14(a) that a two-dimensional grating pattern and periodic dots are produced in this case and the maximum intensities distribute along both x and y axes. The formula of the four-beam laser interference can be expressed as

$$I_{four-beam} = A_1^2 + A_2^2 + A_3^2 + A_4^2 - 2A_1A_3\cos[k\ (\sin\theta_1 + \sin\theta_3)x] - 2A_2A_4\cos[k\ (\sin\theta_2 + \sin\theta_4)y] \quad . \qquad (3.12)$$

As Eq. (3.12) suggested, the intensity distribution of the four-beam interference is equivalent to the two exposures of two-beam interference by rotating the substrate with 90˚. When the incident angles are $\theta_1 = \theta_2 = \theta_3 = \theta_4 = \theta$, the periods in the x and y directions are $d_x = d_y = \lambda/2\sin\theta$. Fig. 3.13(a) shows the captured image of four-beam interference and the measurements of phase shifts are illustrated in Fig. 3.13(b).

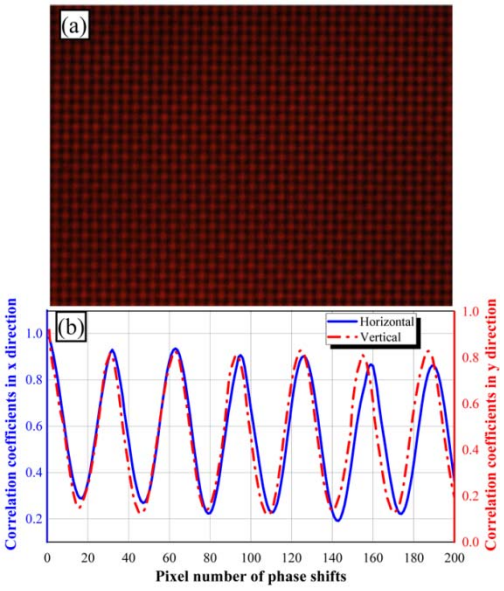

Fig. 3.14 (a) The CCD image of the four-beam laser interference; (b) Corresponding correlation coefficients as a function of phase shifts.

The resulting periods in the x and y directions are 5.8121μm and 5.7192μm, respectively. According to Eq. (3.13), the incident angles can be concluded that θ_1=θ_3=3.17˚, and θ_2=θ_4=3.12˚. With the help of theoretical and image analysis, the deviations of 93nm and 0.05˚ have been determined.

The measurements of period and contrast were attained by Matlab and the scripts are described as Appendix A.

It has been demonstrated that the image processing methods is a powerful tool for analysing almost all types of beam incidence conditions in LIL. Furthermore, the imaging system can also be integrated into a LIL system to achieve real-time imaging and lithography. The schematic of the innovative system is shown in Fig. 3.15. Additional beamsplitter mirrors or prisms are utilised to set up the imaging system, keeping the original optical path unchanged. Once the relationship of the incident angles between the LIL and imaging systems is determined, real-time and dynamic calibrations can be achieved, which is an important application in LIL processes.

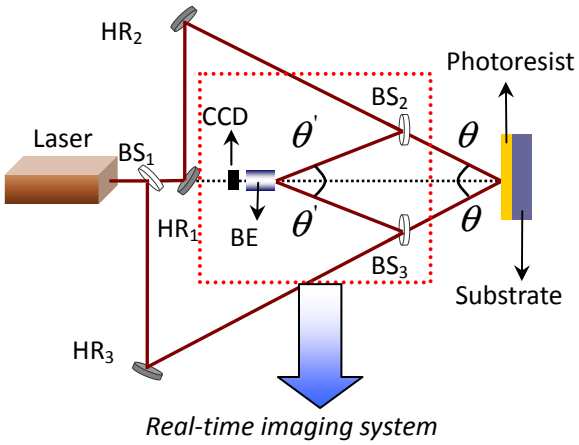

Fig. 3.15 Schematic of the real-time imaging and lithography system.

3.5 Summary

For the conventional LIL, it is a common way that the specimen observations have to be taken into sequential action after the fabrication process finishes. The

minor adjustments take place dependently according to the SEM/AFM results, which is inflexible. As an improved alternative, the imaging interference system has the advantage of detecting the patterns in actual time. It is the principle motivation that chapter 3 proposes the imaging interference system. By taking into a comparative consideration of references [36-40], the algorithms for period measurements are presented. However, to resolve the problem of fulfilling the feedback on micro and nano scales, the comprehensive theoretical analyses especially in the complex multi-beam interference cases must be integrated into the systematic methodology. The combination of previous existing algorithms and theoretical analyses presented in the thesis makes progress with the visualisation and feedback of LIL system.

In this chapter, the He-Ne laser interference system has been setup and by means of it, the multi-beam laser interference patterns can be captured in real-time. Besides traditional two, three and four-beam interference configurations, some extraordinary bionic micro and nano arrays have been found. It extends the capabilities of laser interference technology towards quantities of potential applications for a number of landmark findings demonstrate multi or cross-scale structures own many incredible properties and they have been surprisingly neglected. Moreover, the dual micro and nano interference patterns achieve by He-Ne laser interference system show a good correspondence with computer simulations.

The beam incidence conditions (i.e. measurements of periods and intensities of each beam) are also investigated theoretically and experimentally. It is demonstrated that beam incidence conditions have a significant impact on the period, contrast and formation of interference patterns. To determine the beam incidence conditions, the periods and contrasts of interference patterns are measured by means of image processing algorithms with subpixel accuracy and subsequently the incident angles and intensities of beams are calculated based on the theoretical analysis of spatial distributions of interfering beams. The

relationship between the beam incidence conditions and interference patterns is revealed. The proposed method is useful for the control and calibration of LIL processes, and for reverse engineering applications.

The experimental simulations implemented by the He-Ne imaging interference system are instructive to better understand the influence of slight misalignment of the parameters and conduct the following practical experiments. In the next chapter, an advanced laser interference system is put forward to fabricate the silicon material. In order to examine the performances of high throughput and versatility, the schemes of two-, three- and four-beam interference are translated into actions. Compared to the traditional manner, a high powerful laser is used to create the well-defined structures and a series of significant outcomes are achieved by properly selecting the process parameters.

Chapter 4

Direct Laser Interference Nanomanufacturing

4.1 Related Work

Different from direct laser writing (DLW) which uses a focused laser to modify or subtract materials in a serial or spot by spot way [45], DLIN is able to create a periodic array simultaneously. It is a parallel technique. Stroisch et al. reported that they used a pulsed, frequency tripled picosecond Nd:YAG laser for holographic ablation to pattern a surface relief grating onto an organic material [46]. The laser was 150ps pulsewidth at a wavelength of 355nm and the repetition rate was fixed at 10Hz. In their experiment, two-beam interference method was utilised and a fused silica phase mask of 1050.7nm pitch was added into the system as a beamsplitter. Generally, picosecond lasers often take disadvantage of short coherent length. Therefore, a phase mask is an indispensable element in the system. To quantify the ablation yield, energy densities of 5, 7, 13 and 20mJ/cm^2 were applied to treat a 175-300nm thin film of Alq_3: DCM on glass substrate. The representative of a relief Bragg reflector in their work was shown in Fig. 4.1. The structures were ablated using 500 pulses of 5mJ/cm^2 and the resulting maximum diffraction efficiency of 2.4% was achieved by using 500 pulses of 9.5mJ/cm^2.

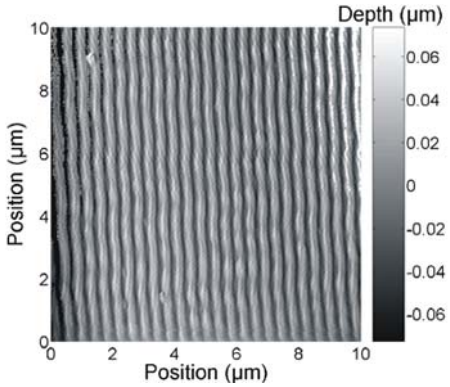

Fig. 4.1 Representative AFM picture of a relief Bragg reflector. (Stroisch *et al.* 2007)

Voisiat et al. also employed a diffractive optical element (DOE) to split the laser irradiation into four beams and they pointed out that the DOE is a key element of experiment setup [47]. The laser source was a picosecond laser Foxtrot (Ekspla Ltd.) with the wavelength of 1064nm and pulse duration of 60ps and the spot where interference of beams took place was 475μm in diameter. The limitation of area fabricated by picosecond and femtosecond laser is a disadvantage of low efficiency. In their experiment, five different metals were used: Chromium, Gold, Copper, Aluminium and Silver. The incident angles of 8.6˚ (±1 order diffraction) resulted in the period of 5μm and pulse energy was fixed to 0.7mJ. It was found that the Chromium, Aluminium and Silver thin films were formed to quadratic matrix arrangement with a single laser pulse while three pulses were required to ablate the Gold thin film as it is a highly reflecting metal. Copper film was 5 times thicker and 100 laser pulses were required for the throughout ablation. In their work, different materials and regular structures were studied by controlling the process parameters. However, there is a lack of theoretical analysis of formation of four-beam interference, especially considering the polarisation mode. In summary, they concluded that the final shape was found to be dependent on phase difference between beam pairs. But the phenomenon has not been given a more detailed explanation, which is also one of the highlights in my work.

Not only picosecond laser but also femtosecond laser can generate interfering beams to fabricate micro periodic structures. Kondo et al. demonstrated that the femtosecond laser was split by a diffraction beam splitter and overlapped with two lenses, resulting in one-, two- and three-dimensional microstructures [48]. But due to the requirement of 10μm order accuracy in optical path lengths, it is inflexible to adjust. Very recently, Wang et al. reported a solution of the limited coherence length of femtosecond laser by means of light field tailoring of the incident beam with a phase mask. With the interaction of first-order diffracted beams and induced waves such as surface plasmon polaritons (SPPs), an interesting phenomenon has been found that the structures are consisted of periodically arranged sub-wavelength nanogratings, as shown in Fig. 4.2.

Furthermore, the orientation of nanogratings relative to microgratings can be controlled by changing the polarised angles of beams. The period of nanogratings ranging from 200nm to 220nm can be explained by the Drude-like mode and defined as $\Lambda = \frac{\Lambda_{sp}}{2} = \frac{\pi}{k_{sp}}$, where K_{sp} is the wave vector of SPP. It has been demonstrated that the hybrid structures can be attained in semiconductor like GaAs, ZnO, ZnS, and ZnSe.

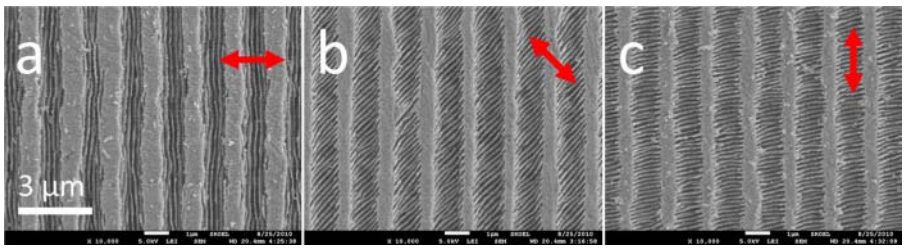

Fig. 4.2 Nanograting orientation tuning by changing the incident laser beam polarisation. The red arrows represent different laser field polarised at (a) perpendicular, (b) 45˚ tilted, and (c) parallel to the micrograting direction. (Wang et al. 2014)

Castro et al. created line and dot structures on the surface of multi-walled carbon nanotubes (MWNTs) based coatings dispersed in antimony-doped tin oxide (ATO) matrix by means of direct two- and three-beam laser methods [49].

A high-power pulsed Nd:YAG nanosecond laser (Quanta-Ray Pro-290, Spectra Physics) was used in their work. They discussed that both MWNT-ATO and pure networks of MWNTs coatings on the borosilicate glass substrates were irradiated with one single pulse. Well-defined arrays of conductive coatings were fabricated with laser fluence ranging from 207 to 644mJ/cm^2 on the MWNT-ATO and MWNT-NET film surfaces, as depicted in Fig. 4.3 and Fig. 4.4. The significant different topographies of two films were caused by high absorption coefficient of ATO.

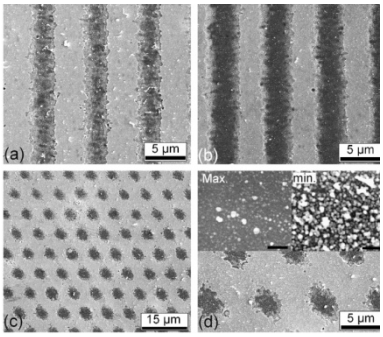

Fig. 4.3 Scanning electron microscope micrographs of irradiated MWNT-ATO films with (a and b) two and (c and d) three laser beams interference patterns: (a) laser fluence=207mJ/cm^2; (b) laser fluence=483mJ/cm^2; (c and d) laser fluence =644mJ/cm^2. The insert in (d) shows the surface morphology at the interference maximum and minimum. (Castro et al. 2008)

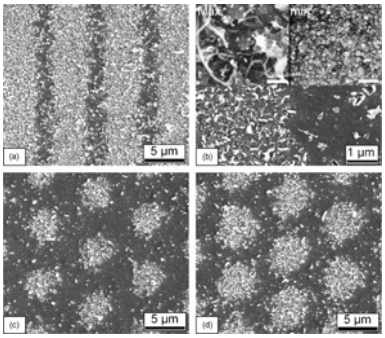

Fig. 4.4 Scanning electron microscope micrographs of MWNT-NET films deposited on borosilicate glass irradiated with (a and b) two and (c and d) three laser beams interference patterns. The laser fluences were (a) 272mJ/cm^2, (b) 251mJ/cm^2, (c) 163mJ/cm^2, and (d) 211mJ/cm^2. The insert in (b) shows the surface morphology at the interference maximum and minimum. (Castro et al. 2008)

Since laser interference metallurgy was proposed [50], numerous efforts have been implemented to create micro and sub-micro structures on the bulk metal surfaces. For the purpose of fabrication of well-defined structures, a nanosecond NG: YAG laser of 355nm wavelength was used by D'Alessandria et al. and they studied the mechanism of structure formation on aluminium surfaces and also analysed the experimental results by means of thermal simulations [51]. With the laser fluence of 688mJ/cm^2, the modification on surface took place independently of structure shapes. As the increase of laser fluence up to 2100mJ/cm^2, the quality of morphology decreased and countless droplet ejected molten metal were observed at the same time. To explain the main forces to create the structures during the direct laser interference ablation, a thermal simulation determining the temperature distribution of irradiation area was developed. It was found that the influence of reflectivity, laser fluence and period played important role in laser removal of materials. Their subsequent publication gave a detailed explanation for a FEM simulation [52]. According to the method,

the photo-thermal interaction of features of one or two layer thin metallic films is interpreted and corroborates the experimental observations.

Besides the technique itself, considerable efforts are currently focusing on the various potential applications. A number of arising novel nanomaterials and devices are attracting attentions of people throughout the world. In 2013, Roch et al. used a nanosecond UV-laser (wavelength 355nm) to irradiate the tetrahedral amorphous carbon (ta-C) films that feature outstanding properties of chemical inertness, low wear and low friction [53]. Depending on the pulse number, the thresholds of the graphitization of ta-C films vary from 47 to 74mJ/cm^2. With the investigation of tribological performance under non-lubricated condition, it was found that the both line and dot structures fabricated by using two and three beam interference method enabled to reduce the coefficient of friction and the maximum reduced up to 30% from un-patterned samples to micro dot-structured ones, as shown in Fig. 4.5.

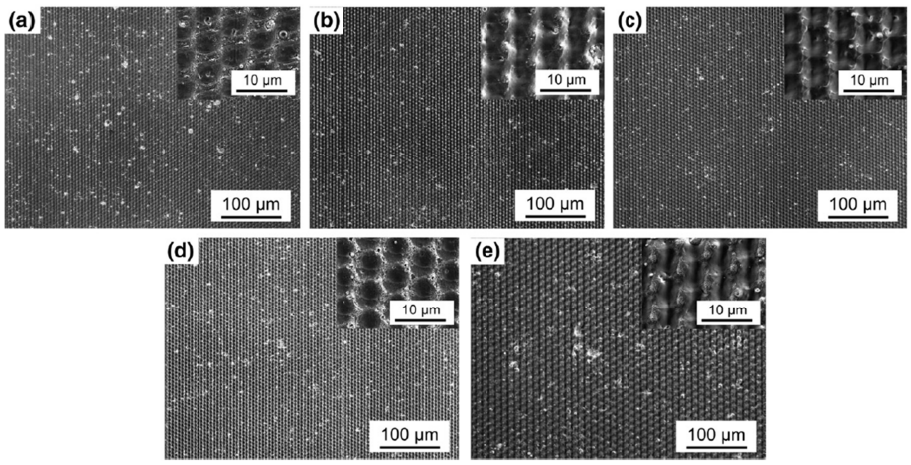

Fig. 4.5 Scanning electron micrographs of 2.5µm ta-C film structured by DLIP technique. The spatial period was 5.0µm. The dot-like patterns were fabricated by utilising three-laser beams setup. Different numbers of laser pulses and laser fluences were used. In (a)–(c) the number of laser pulses is constant (20 pulses) and the fluence is increased from 405mJ/cm^2 to 590mJ/cm^2 and 810mJ/cm^2. In images (d) and (e) the fluence is constant (405mJ/cm^2) and the pulse number is increased from 10 to 30 pulses. (Roch et al. 2013)

Recently, people are developing the direct laser interference technology to a

number of significant applications, such as light emitting devices (LEDs) and solar cells. In 2014, Kim et al. report that direct laser interference patterning (LIP) as an effective technology was used to achieve controlled periodic structures on a semiconductor surface [54]. The first layer of LEDs, a *p*-GaN: Mg (~200nm, $p\sim7\times10^{17}cm^{-3}$), was treated by a nanosecond laser (wavelength=266nm, pulse width=10ns, and repetition rate=10Hz). Since the hexagonal lattice array is found to be optimized structures for enhancing the conversion efficiency, three-beam interference configuration was utilised in the experiment. After laser ablation, holes arranged in a two-dimensional distribution were produced with an open size of 500nm, depth of 50nm, and a periodicity of 1μm. The proposed method is regarded as a quite powerful tool without photolithography or electron-beam lithography processes. Finally, the laser-patterned LEDs exhibit an enhancement in light output power of 20% compared to conventional LEDs having a flat top surface. A representative result in their work is shown in Fig. 4.6.

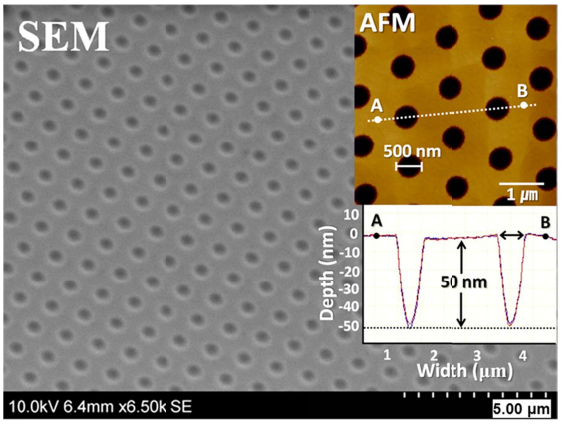

Fig. 4.6 Surface images of the laser-patterned light-emitting diode epitaxial layer structure showing inverted-cone-shaped holes in *p*-GaN layers by SEM and AFM (inset). (Kim et al. 2014)

Considering the texture surface enhancing the light output power or efficiency, the primary mechanism is to disturb the waveguide effect which brings about spontaneous recombination and confinement of photons. In order to verify the viewpoint, Monte-Carlo ray-tracing simulations were carried out by means of the LIGHTTOOLS modelling software. The results demonstrate that the light is more efficiently extracted from the top of texturing surface of LEDs than that of

un-patterned LEDs.

Actually, the enhancement of efficiency on a basis of structured surface is also found to be an effective solution for organic light emitting diodes (OLEDs) [55]. Both LEDs and OLEDs are very important energy-saving products and are being widely applied for illumination, smartphones, digital cameras, and quantities of consumer electronics. It has been demonstrated that direct laser interference technique has the capability of producing periodic micro and nano structures with high throughput and at the same time promising novelty revolutionary applications in a huge number of areas.

In summary, several research groups have reported that they used the direct laser interference technology for the fabrication of periodic structures in different materials. However, there is a lack of theoretical analysis of the formation of laser interference patterns and their corresponding surface structures fabricated. In this work, the silicon material is selected and expected to create different well-defined surface structures based on theoretical analysis of the formation of laser interference patterns. Two-beam, three-beam and four-beam nanosecond laser interference systems were set up to modify the silicon surface, resulting in the grating, regular triangle and square structures. AFM was employed to observe the profiles of samples and analyse the structural dimensions. From the AFM micrographs shown, the critical features of structures have a dependence on laser fluences. By properly selecting the process parameters, well-defined grating and dot structures can be achieved.

4.2 Overview of Nanosecond Laser Interference System

In the work, a nanosecond laser interference system was employed to carry out the experimental study. The laser is a Q-switched Nd:YAG laser (INNOLAS SpitLight-2000, Germany), producing maximum 2J per pulse at 1064nm at 10Hz. The pulsewidth is 6-8ns and beam diameter is approximate to 9mm. It features robust and stable resonator structure, which ensures high quality of Gaussian

beam and high efficiency. Different harmonic generators extend the wavelength range to the second, third and fourth harmonics. Moreover, the laser is injected with a seeded laser and the linewidth is low to 0.003cm^{-1}. These features offer an excellent coherent source for interference.

4.2.1 DLIN Concept

DLIN refers to direct laser interference nanomanufacturing. Compared with conventional LIL, the energy distribution modulated by nanosecond laser interference is transferred to substrate surface directly and corresponding micro and nano structures throughout spot area are fabricated at the same time.

4.2.2 Advantages of System

DLIN takes the advantage of straightforward process without the mask and photoresist. Additionally, compared with the point by point writing modality of EBL, FIB and SPL, it is a parallel technology which can fabricate various structures with two or multi-beam laser interference simultaneously. The periodicity of structures corresponds to the interference distribution with maximum and minimum intensities, which can be controlled from micrometres to nanometres continuously by adjusting the incident angles (θ) and/or wavelengths (λ). The size of produced structures can be as large as the beam area (>cm^2). In summary, the advantages of DLIN can be concluded as follows:

- High throughput
- Low cost
- Controlled periodicity ($d=\lambda/2\sin\theta$)
- Large area manufacturing (>cm^2)
- Various materials (e.g. semiconductor, metal, organic material and so on).

Due to the simple system and technological procedure, DLIN is a promising tool for volume production and suitable for a large quantity of potential applications. It is a promising technology with the capability for the manufacturing of micro and nano structures.

To develop the DLIN, the theoretical and experimental investigations are carried out systematically. The significances of the work in this chapter are highlighted as below:

- Direct modification of silicon surface by nanosecond laser interference technology
- Theoretical analysis of the formation of laser interference patterns and use of silicon material to create their corresponding well-defined surface structures
- Two, three and four beam laser interference systems used to fabricate grating, regular triangle and square structures on silicon surfaces
- Analysis of the critical features of structures obtained from different laser fluences
- Nanosecond laser interference lithography suited to flexibly fabricate well-defined micro and nano structures for different applications such as anti-reflection and self-cleaning surfaces by properly selecting the process parameters.

4.3 Experimental Procedures

All the samples used in the experiment were polished single crystal silicon (100) wafers and the experiments were carried out under ambient conditions. The schematic of optical path is shown in Fig. 4.7. The beams were split by beamsplitters and high-reflective mirrors. Quarter wave plates and polarisers were placed before the exposed samples to control the power and polarisation

angles precisely. The power and energy of the laser were measured with the Laser Power and Energy Meter (Coherent LabMax-top, USA). The surface morphology of the samples was characterised with the atomic force microscope (AFM).

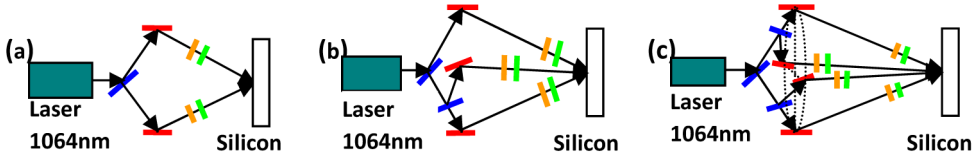

Fig. 4.7 Schematic set-up for the direct laser interference system with (a) two-beam; (b) three-beam; (c) four-beam. The red line is high-reflective mirror, the blue line is beamsplitter, the orange line is quarter wave plate, and the green line is Brewster polariser.

4.4 Direct Modification of Silicon Surface

4.4.1 Theoretical Analysis and Simulations

The theoretical equations of two, three and four-beam laser interference with proposed polarisation modes describing the electric field vectors and interference intensity distributions are derived on a basis of the methodology in section 2.4 and expressed in Eqs. (4.1), (4.2) and (4.3) respectively,

$$I_{TE-TE} = A^2[2-2\cos(2k\cdot\sin\theta\cdot x)] \ , \tag{4.1}$$

$$I_{TE-TE-TM} = A^2\left\{\begin{array}{l} 3+\sqrt{3}\cos\theta\cdot\cos\left(k\cdot\sin\theta\cdot y\right) \\ -\sqrt{3}\cos\theta\cdot\cos\left[k\left(\sqrt{3}/2\cdot\sin\theta\cdot y+3/2\cdot\sin\theta\cdot x\right)\right] \\ -\cos\left[k\left(\sqrt{3}/2\cdot\sin\theta\cdot y-3/2\cdot\sin\theta\cdot x\right)\right] \end{array}\right\} \ , \tag{4.2}$$

$$I_{TE-TE-TE-TE} = A^2\cdot[4-2\cos(2k\cdot\sin\theta\cdot x)-2\cos(2k\cdot\sin\theta\cdot y)] \ . \tag{4.3}$$

The distribution of the interference patterns was done by Matlab to simulate 2D and 3D profiles. Since the theoretical equations are hardly enough to describe all the insights of a physical phenomenon, mathematical modelling and

computer-assisted investigation are applied to study the implications. According to Eqs. (4.1)-(4.3), the simulations of two, three and four-beam interference were shown in Fig. 4.8. From the simulations suggested, it is demonstrated that grating pattern is generated in the two-beam interference, triangle array pattern is generated in the three-beam interference, and square array pattern is generated in the four-beam interference. With the investigation of parameters, i.e. wavelengths, incident angles, azimuthal angels, polarised angles and relative phase, the formation of interference patterns exhibit a large variation. Herein, the resulting structures have shown a good correspondence with the theoretical analysis and simulations, which is discussed in the next section.

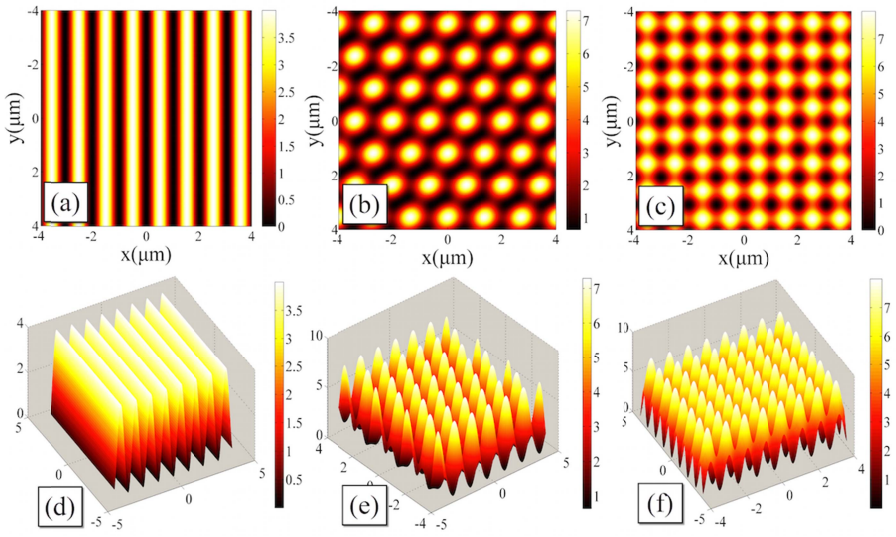

Fig. 4.8 Laser interference simulations. (a) 2D intensity distribution for two-beam interference; (b) 2D intensity distribution for three-beam interference; (c) 2D intensity distribution for four-beam interference; (d) 3D intensity distribution for two-beam interference; (e) 3D intensity distribution for three-beam interference; (f) 3D intensity distribution for four-beam interference; ($\lambda = 1064nm, \theta = 30°$).

4.4.2 Two-beam Laser Interference

The initial laser beam is divided into two beams with the azimuthal angles of $\phi_1 = 0°$, $\phi_2 = 180°$, $\psi_1 = \psi_2 = 90°$ and the incident angles of $\theta_1 = \theta_2 = 4°$, which, according to Eq. (2.7), results in the period of 7.5μm. Because of the TM

polarisation from the laser source, quarter wave plates are needed to change the linear polarisation to circular polarisation, and then polarisers are placed in the final position to obtain the desired polarisation angles. Different exposure doses, ranging from 560 to 700mJ/cm^2, are used to determine the optimum dose for a good feature patterning. The results are shown in Fig. 4.9.

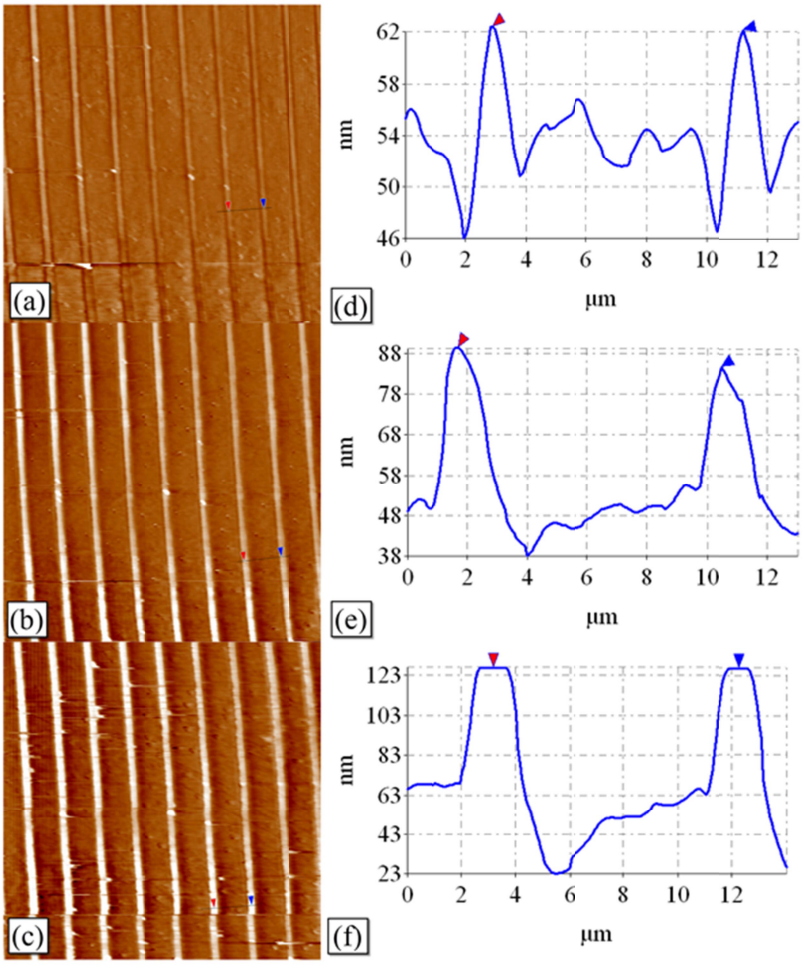

Fig. 4.9 AFM micrographs of two-beam laser interference patterning with a single pulse: (a) laser fluence=560mJ/cm²; (b) laser fluence=630mJ/cm²; (c) laser fluence=700mJ/cm²; (d), (e) and (f) the cross-sectional views in (a), (b) and (c), respectively.

4.4.3 Three-beam Laser Interference

In the experiment, the three incident beams, followed a symmetrical configuration with the azimuthal angles of $\phi_1 = 0°$, $\phi_2 = 120°$, $\phi_3 = 240°$,

$\psi_1 = \psi_2 = 90°$, $\psi_3 = 0°$ and the incident angles of $\theta_1 = \theta_2 = \theta_3 = 6.8°$, result in the period of 4.5μm. Compared with two-beam laser interference, three-beam laser interference can fabricate the equilateral triangle dot structures, as shown in Fig. 4.10. Exposure doses are identical with two-beam laser interference, ranging from 560 to 700mJ/cm^2.

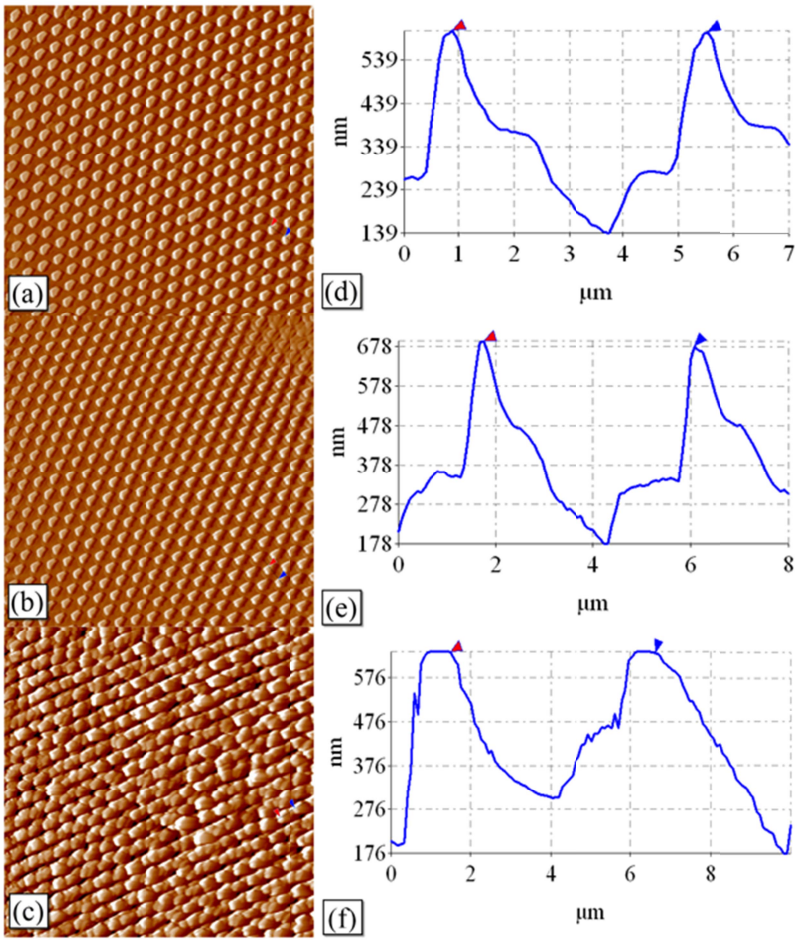

Fig. 4.10 AFM micrographs of three-beam laser interference patterning with a single pulse: (a) laser fluence=560mJ/cm²; (b) laser fluence=630mJ/cm²; (c) laser fluence=700mJ/cm²; (d), (e) and (f) the cross-sectional views in (a), (b) and (c), respectively.

4.4.4 Four-beam Laser Interference

The four incident beams, followed a symmetrical configuration with the azimuthal angles of $\phi_1 = 0°$, $\phi_2 = 90°$, $\phi_3 = 180°$, $\phi_4 = 270°$, the polarised

angles of $\psi_1 = \psi_2 = \psi_3 = \psi_4 = 90°$, and the incident angles of $\theta_1 = \theta_2 = \theta_3 = \theta_4 = 5°$, which results in the period of 6.1μm. As shown in Fig. 4.11, the square dot structures are fabricated by four-beam laser interference. Different laser fluences have an effect on the structures, which is discussed in the following section.

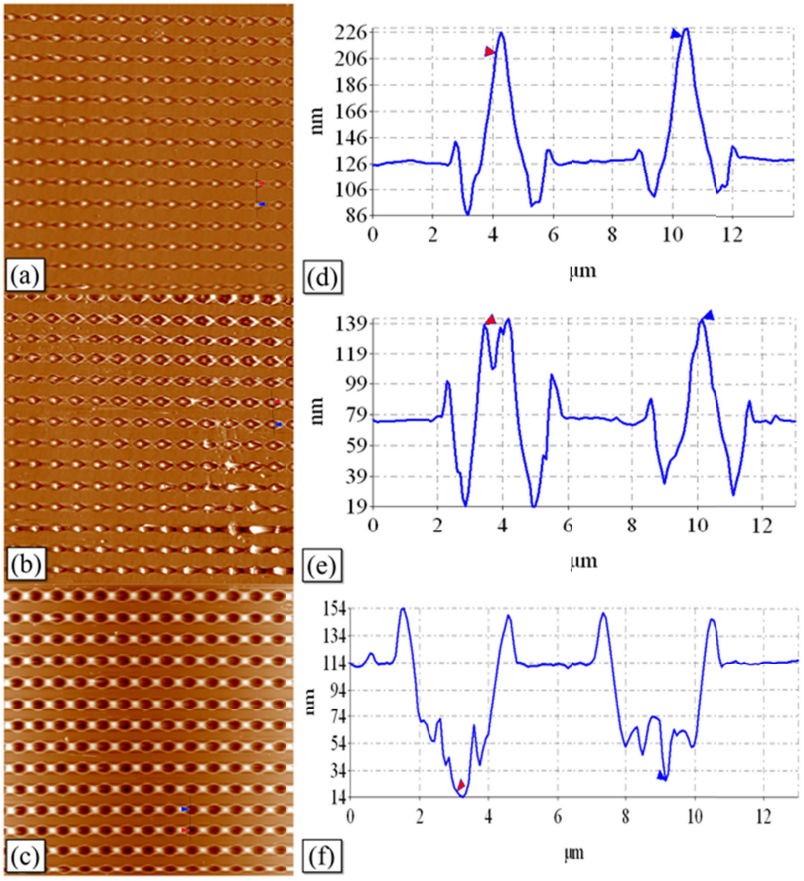

Fig. 4.11 AFM micrographs of four-beam laser interference patterning with a single pulse: (a) laser fluence=560mJ/cm²; (b) laser fluence=630mJ/cm²; (c) laser fluence=700mJ/cm²; (d), (e) and (f) the cross-sectional views in (a), (b) and (c), respectively.

4.4.5 Discussion of Surface Structures

Based on the theoretical analysis, the intensity distributions of two, three and four-beam laser interference have been obtained. Eq. (4.1) suggests that there is only one periodicity along the X axis in two-beam laser interference. Consequently, grating structures are formed on the silicon surface in two-beam laser interference. Unlike the two-beam interference, there are three interfered terms

in Eq. (4.2) for three-beam laser interference. The direction of dot periods is along the X axis, the straight line of $y=\sqrt{3}x$ and the straight line of $y=-\sqrt{3}x$, respectively. For this reason, three-beam laser interference can fabricate triangle dot structures. Eq. (4.3) indicates that the periods along the X and Y axes are identical; thereby four-beam laser interference generates the square dot structures. The theoretical derivation shows a good correspondence with not only simulations but also the experimental results (Figs. 4.9, 4. 10 and 4.11).

The energy distribution modulated by laser interference is transferred to the silicon surface to produce the periodic structures. The structures were obtained by nanosecond laser interference lithography, and they were different from those in the reference [56]. Tavera et al. used the laser fluences from 0.8J/cm^2 to 2.0J/cm^2 and obtained three different structures showing the effects of the laser fluences on the result patterns. The absorption coefficient of silicon is about 1.11E+01 (cm^{-1}) at 1064nm wavelength but 1.04E+06 (cm^{-1}) at 355nm wavelength. Since the absorption coefficient at 355nm is much stronger than that at 1064nm [57], the well-defined interference structures were observed in the outer perimeter regions, and the central areas were likely to be overexposed due to the applied larger laser fluences, especially when the focusing lens was used. To meet certain application requirements, focusing or objective lens is useful to increase the laser fluence at the cost of reduced irradiation areas. With high-peak power pulsed laser, macroscale areas (>cm^2) of fabrication can be efficiently achieved. In addition, the deeper trenches and holes obtained in this work show that the thermal diffusion length and structural period play important roles in the result patterns. If the period approaches the thermal diffusion length, the temperature difference between maximum and minimum intensities decreases and does not bring about a periodic melting surface, leading to a more homogenous heating source. Consequently, the deeper structures could be easily obtained for larger interference periods. Furthermore, the energy of single photon at 355nm is around three times then that at 1064 nm. When the 355nm laser irradiated the samples, the laser light can induce single-photon or multiphoton inter-band

transitions and photon-electron excitation can result in direct bond breaking. But infrared laser excites electrons within the conduction band and vibrations in silicon. In this case, the thermalization of the excitation energy is fast and the laser can be considered as a heat source.

As another interesting finding, conductivity variations across silicon surfaces were observed by conductive atomic force microscopy (CAFM). From the Fig. 4.12 shown, the current images of three- and four-beam interference (Fig. 4.12(b) and (d)) show a correspondence with the topographic images (Fig. 4.12(a) and (c)).

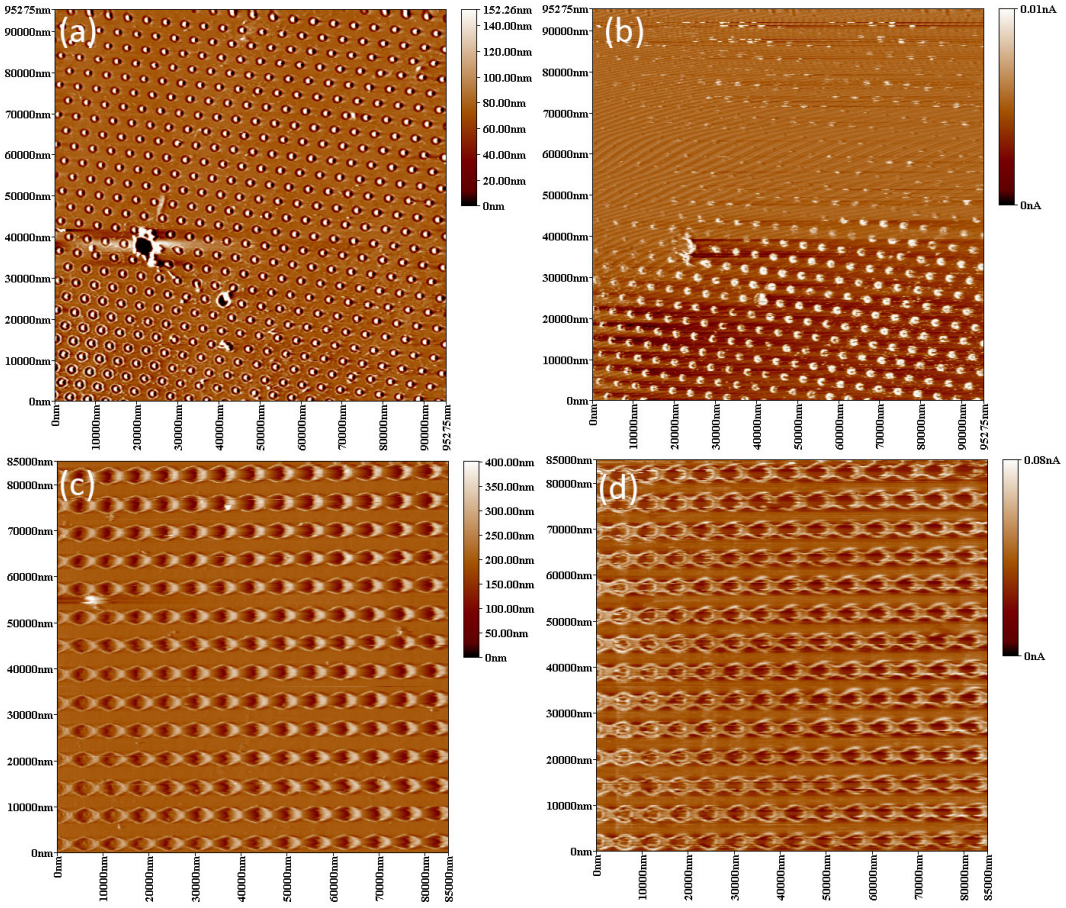

Fig. 4.12 (a) the topographic image of three-beam interference; (b) the conductive image of three-beam interference; (c) the topographic image of four-beam interference; (d) the conductive image of four-beam interference.

A 10v bias voltage is applied between conductive tip of CAFM and samples, generating maximum current of 0.01nA on the sample fabricated three-beam

interference and maximum current of 0.08nA on the sample fabricated four-beam interference. Due to the current images were taken from the same position of topographic images, it can be identified that the surface conductivity induced by laser is rearranged and the arrangement correlating to distribution of microstructures may be attributed to the enhancement of effective contact area between tip and microstructures [58, 59].

Whatever the grating, triangle or square micro and nano structures are found to be an effective way to fulfil the applications of Photonic crystals and Quantum dots. For instance, the Bragg grating is a type example of one-dimension photonic crystal used as an optical switch [46]. Compared to the existing techniques which enable to fabricate the functional structures, e.g. EBL and FIB that write features with point-by-point or line-by-line strategy, an array of uniform periodic structures can be produced at the same time directly by means of DLIN. In addition, the resulting structures have the advantage of affecting the motion of photons or electrons in an extraordinary way and promise to be used in different forms in a wide range of applications.

4.5 Summary

The previous chapter mainly addresses a visualized method to observe the interference patterns in actual time. Through the implementation of experimental simulations, the method enables to verify the correspondences between the theoretical analyses and experimental results and moreover offers a more intuitive way to explore the principle of interference distribution. Benefiting from the extensive detailed analyses in chapter 3, the experiments carried out by the high-power laser interference system is put forward.

In this chapter, the strategy of direct modification of silicon surface is used by means of nanosecond laser interference technique and the theoretical analyses of the formation of two or multi-beam laser interference are studied as well. The pattern generated by the intensity distribution of interference is transferred to the

material to produce periodic structures. For a relative low laser fluence, well-defined grating and dot structures have been achieved, and with the laser fluences increased, interactive thermal effect has been observed. Compared with other technologies, DLIN provides an attractive way to fabricate or modify various materials with low cost and high throughput. By properly selecting the process parameters, nanosecond laser interference system is well suitable to flexibly fabricate micro and nano structures for different applications such as anti-reflection and self-cleaning surfaces.

In contrast to two- and three-beam interference, the modulation phenomenon takes place obviously in the case of four-beam interference. The phenomenon was found and described in a number of previous publications. However, there is still a lack of underlying mechanism of modulation and corresponding influence factors are not well-interpreted, which remains a challenge and gap for the scientific and engineering fields. Thus, chapter 5 is highlighted individually and the goal is to explicate the effects of polarisation vector on four-beam interference in views of both theoretical and experimental aspects.

Chapter 5

Effects of Polarisation on Laser Interference Technology

5.1 Related Work

In laser interference, the intensity distribution is a function of incident angles, azimuthal angles, phase differences and polarisation directions. At present, more and more applications are focused on the fabrication of periodic and quasi-periodic micro and nano structures. Among them, four-beam laser interference lithography is the most extensively investigated technology [47, 60-63]. Theoretically, four-beam laser interference could generate evenly-distributed periodic structure patterns, but in practice, noticeable modulations were almost unavoidably introduced in interference patterns due to the misalignment of incident angles or unequal incident angle.

Tan et al. reported that the linear defects were fabricated by four-beam interference lithography when the modulation period emerged and then it was found that the grade-type defects had the potential to be used for tapered transmission line defect resonators, graded photonic crystals (PhC) and tapered PhC micro- cavities embedded in photonic wire waveguides [64]. With respect to the modulation period, they pointed out a number of influence parameters, i.e. incident angles, phase changing and polarisation. Experimentally, the width of linear defects showed a dependence on the relationship of intensity and threshold of modification. From Fig. 5.1 shown, the centre and border regions, corresponding to (a) and (b) in the figure respectively, of one laser spot exhibited different defect widths along x-direction. Due to the Gaussian beam distribution, position A was irradiated much more strongly than position B. The results were W_1=1.727μm, W_2=2.434μm. Although it was demonstrated that the unequal incident angles in four-beam interference would give rise to the modulation or secondary period in their case and the quantitative analysis of modulation pitch

was discussed as well, the other polarisation configures which also bring about different formations of four-beam interference remain an unexplained gap.

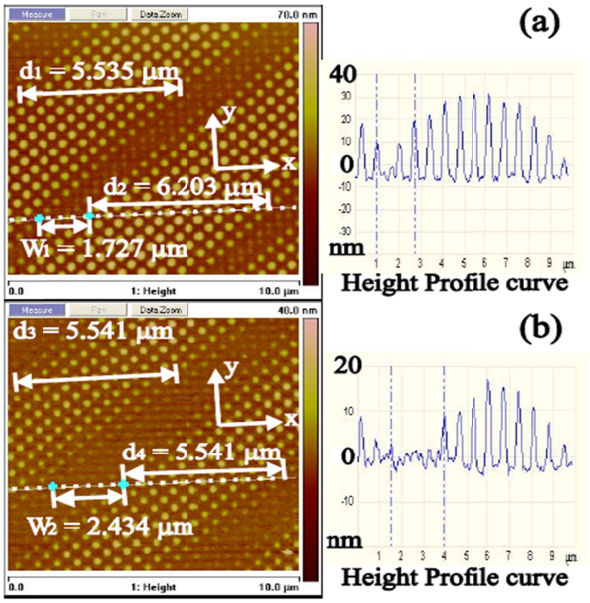

Fig. 5.1 AFM micrograph of interference patterns generated by the laser beams at (a) high intensity and (b) low intensity. (Tan et al. 2008)

In the follow-up work, the property of non-uniformity of peak intensity across the wafer in which the modulation occurred was employed to generate a "large size area" and a "small size area", aiming to achieve high-resolution nanostructures [65]. The schematic is shown in Fig. 5.2.

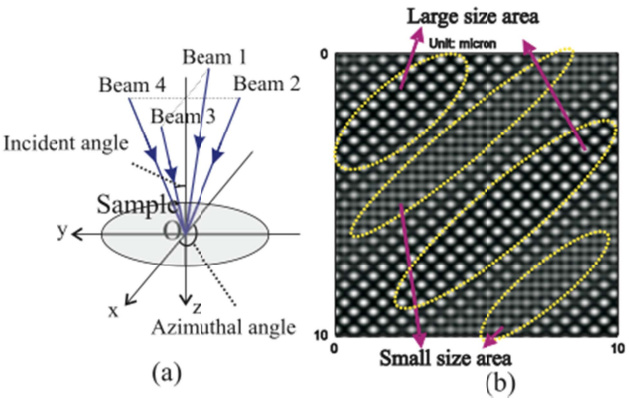

Fig. 5.2 (a) Scheme of the four-beam interference system; (b) simulated intensity distribution of four-beam interference field on a sample. (Tan et al. 2009)

The sample was a 5nm thick SiO_2 layer grown on a 2 inch GaAs (111) wafer by means of plasma-enhanced chemical vapour deposition and laser source was a gas nanosecond laser (wavelength=308nm, pulsed width=20ns). By controlling the laser fluence properly, a phenomenon that the SiO_2 thin layer transformed into bubble state at the maximum interfering intensities was observed. A model of light-matter interaction was proposed to interpret the result. After dry etching of SiO_2, small nanohole structures appeared and the minimum one was less than 30nm and depth of 3nm. In summary, periodic nanostructures were formed on the wafer including the bubble-like SiO_2 features and nanohole in GaAs and hole size of 30nm was directly observed by AFM.

Tavera et al. have reported that laser induced periodic surface patterns, in particular micro and nano ripples, were found when the nanosecond laser irritated silicon material with a four-beam nanosecond interference system [56]. Different laser fluences (0.8J/cm^2, 1.3J/cm^2, 2.0 /cm^2) were used to modify the samples and corresponding measurements of solar weighted reflectance were obtained. For the below laser fluence of 0.8J/cm^2, silicon does not suffer the significant modifications in their experiment. With higher laser fluence (0.8-1.3J/cm^2), the central area is dominated by the micro ripples pattern. Since the period of micro ripples shows a correspondence with modulation in four-beam interference, it is confirmed that the presence of micro ripples is caused by the intensity modulation due to a non-perfectly symmetric configuration. According to the simulation result, a 3° mistake of one of four incident angles will give rise to a period of 12.5μm modulation approximately, as show in Fig. 5.3. The conclusion can be also obtained by the previous publications but there is still a lack of detailed analysis of different polarisation modes and the relationship of polaristion vector and modulation. The formation of nano ripples appears when laser fluence further increases up to 1.3-2.0 J/cm^2. At first, they form concentric circles surrounding the central area and then spread over the spot with a laser fluence up to 2.0J/cm^2. As a result of presence of micro and nano ripples, the reflectivity shows a decrease for the samples processed with

laser.

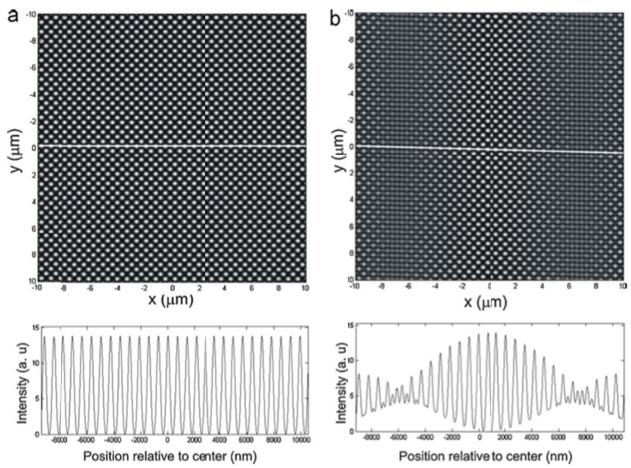

Fig. 5.3 Intensity distribution simulation of the resulting interference of four laser beams with an angle of incidence of 30° and a period of 500nm: (a) perfectly symmetric configuration [β_1=0°, β_2=90°, β_3=180°, β_4=270°], (b), asymmetric configuration [β_1=0°, β_2=90°, β_3=180°, β_4=273°]. The lower graphs show the intensity distribution along the white line. (Tavera et al. 2011)

As mentioned above, numerous literatures have demonstrated that the intensity modulation is related to the unequal incident angles in four-beam interference. Apart from the incident angles, the effects of azimuthal angles and phase differences on the pattern formation were also discussed in a number of publications [14, 48, 61, 66-68]. However, little work has been carried out to study in detail the effect of polarisation on the formation of interference patterns and surface structures in four-beam laser interference.

5.2 Theoretical Analysis

Three different polarisation modes, including TE-TE-TE-TE, TE-TE-TE-TM and TE-TE-TM-TM, were presented to analyse the effects of polarisation on four-beam laser interference based on theoretical analysis, simulations and experiments. Transverse electric wave abbreviates as TE and transverse magnetic wave abbreviates as TM.

As shown in Fig. 5.4, the four incident beams follow a symmetrical configuration

with the azimuthal angles of $\phi_1 = 0°$, $\phi_2 = 90°$, $\phi_3 = 180°$ and $\phi_4 = 270°$. The incident angles of the four beams can be set as $\theta_1 = \theta_2 = \theta_3 = \theta_4 = \theta$. However, if any of the incident angles is misaligned, or is unequal to the others, there will be a modulation in the pattern. In this case, the incident angle $\theta_3 = \theta^*$ is used in the simulations, keeping other parameters unchanged. Based on the Eqs. (2.4), (2.5), (2.16), and (2.17), it is assumed that amplitudes of each beam are identical and initial phases are 0. Effects of three different polarisation modes are discussed below.

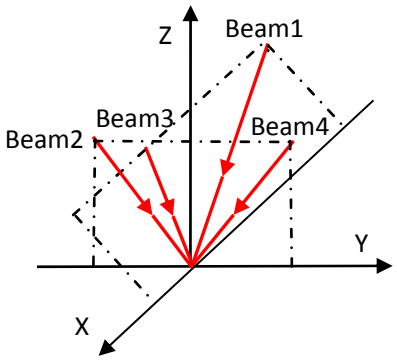

Fig. 5.4 Four-beam interference configuration.

In the case of the TE-TE-TE-TE mode, the polarisation angles of four beams are set as $\psi_1 = \psi_2 = \psi_3 = \psi_4 = 90°$. According to Eqs. (2.4), (2.5), (2.16), and (2.17) and the methodology described in section 2.4, the electric field vectors can be written as

$$\begin{aligned}
\vec{E}_1 &= A\left\{-y\cdot\vec{j}\cdot\cos\left[k(\sin\theta\cdot x-\cos\theta\cdot z)-\omega t\right]\right\}\\
\vec{E}_2 &= A\left\{x\cdot\vec{i}\cdot\cos\left[k(\sin\theta\cdot y-\cos\theta\cdot z)-\omega t\right]\right\}\\
\vec{E}_3 &= A\left\{y\cdot\vec{j}\cdot\cos\left[k(-\sin\theta\cdot x-\cos\theta\cdot z)-\omega t\right]\right\}\\
\vec{E}_4 &= A\left\{-x\cdot\vec{i}\cdot\cos\left[k(-\sin\theta\cdot y-\cos\theta\cdot z)-\omega t\right]\right\}
\end{aligned} \quad . \tag{5.1}$$

The intensity of the interference I_i and the modulation intensity of the interference I_i^* are expressed as

$$I_i = A^2\cdot\left[4-2\cos(2k\cdot\sin\theta\cdot x)-2\cos(2k\cdot\sin\theta\cdot y)\right] \ , \tag{5.2}$$

$$I_i^* = A^2 \cdot \left\{4 - 2\cos k \cdot \left[(\sin\theta + \sin\theta^*) \cdot x - (\cos\theta - \cos\theta^*) \cdot z\right] - 2\cos(2k \cdot \sin\theta \cdot y)\right\} \quad . \text{(5.3)}$$

In the case of the TE-TE-TE-TM mode, the parameters of the electric field vectors are the same as the TE-TE-TE-TE mode except the polarisation vectors. They are changed to

$$\begin{aligned} \vec{p}_1 &= -y \cdot \vec{j} \\ \vec{p}_2 &= x \cdot \vec{i} \\ \vec{p}_3 &= \cos\theta \cdot x \cdot \vec{i} - \sin\theta \cdot z \cdot \vec{k} \\ \vec{p}_4 &= -x \cdot \vec{i} \end{aligned} \quad . \qquad (5.4)$$

The intensity of the interference I_{ii} and the modulation intensity of the interference I_{ii}^* are expressed as

$$I_{ii} = A^2 \cdot \begin{Bmatrix} 4 - 2\cos(2k \cdot \sin\theta \cdot y) \\ +2\cos\theta \cdot \cos[k \cdot (\sin\theta \cdot x + \sin\theta \cdot y)] \\ -2\cos\theta \cdot \cos[k \cdot (\sin\theta \cdot x - \sin\theta \cdot y)] \end{Bmatrix} \quad , \qquad (5.5)$$

$$I_{ii}^* = A^2 \begin{Bmatrix} 4 - 2\cos(2k \cdot \sin\theta \cdot y) \\ +2\cos\theta^* \cdot \cos k[\sin\theta^* \cdot x + \sin\theta \cdot y - (\cos\theta - \cos\theta^*)z] \\ -2\cos\theta^* \cdot \cos k[\sin\theta^* \cdot x - \sin\theta \cdot y - (\cos\theta - \cos\theta^*)z] \end{Bmatrix} \quad . \qquad (5.6)$$

In the case of the TE-TE-TM-TM mode, the parameters of the electric field vectors are the same as the TE-TE-TE-TE mode except the polarisation vectors. The polarisation vectors are

$$\begin{aligned} \vec{p}_1 &= -y \cdot \vec{j} \\ \vec{p}_2 &= -\cos\theta \cdot y \cdot \vec{j} - \sin\theta \cdot z \cdot \vec{k} \\ \vec{p}_3 &= y \cdot \vec{j} \\ \vec{p}_4 &= \cos\theta \cdot y \cdot \vec{j} - \sin\theta \cdot z \cdot \vec{k} \end{aligned} \quad . \qquad (5.7)$$

The intensity of the interference I_{iii} and the modulation intensity of the interference I_{iii}^* are expressed as

$$I_{iii} = A^2 \cdot \begin{Bmatrix} 4 - 2\cos(2k \cdot \sin\theta \cdot x) \\ + 2(\sin^2\theta - \cos^2\theta) \cdot \cos(2k \cdot \sin\theta \cdot y) \\ - 4\cos\theta \cdot \cos[k \cdot \sin\theta \cdot (x + y)] \\ + 4\cos\theta \cdot \cos[k \cdot \sin\theta \cdot (x - y)] \end{Bmatrix}, \quad (5.8)$$

$$I^*_{iii} = A^2 \begin{Bmatrix} 4 - 2\cos\ k \cdot [(\sin\theta + \sin\theta^*) \cdot x - (\cos\theta - \cos\theta^*) \cdot z] \\ + 2(\sin^2\theta - \cos^2\theta) \cdot \cos(2k \cdot \sin\theta \cdot y) \\ - 2\cos\theta \cdot \cos[k \sin\theta (x + y)] \\ + 2\cos\theta \cdot \cos[k \sin\theta (x - y)] \\ - 2\cos\theta \cdot \cos\ k \cdot [\sin\theta^* \cdot x + \sin\theta \cdot y - (\cos\theta - \cos\theta^*) z] \\ + 2\cos\theta \cdot \cos\ k \cdot [\sin\theta^* \cdot x - \sin\theta \cdot y - (\cos\theta - \cos\theta^*) z] \end{Bmatrix}. \quad (5.9)$$

The equations of interference intensity and modulation intensity in three cases are derived. It has been demonstrated that the polarisation vector plays a key role in the formation of interference patterns, pattern contrast and periods.

5.2.1 Effect on the Period and Contrast

It can be seen from Eqs. (5.2) and (5.3) that the maximum intensity is $8A^2$ and the minimum intensity is 0 in the TE-TE-TE-TE mode. The periods in the y direction, expressed by Eqs. (5.2) and (5.3), are identical. But the periods in the x direction are changed from $d_x = \lambda / 2\sin\theta$ to $d_{x^*} = \lambda / (\sin\theta + \sin\theta^*)$. For this reason, the dot patterns are changed from the square to rectangle shape.

In the TE-TE-TE-TM case, the period of dot structures in the x direction is twice of the TE-TE-TE-TE mode. Additionally, $10A^2$ and $2A^2$ are the boundaries of the maximum and minimum intensities respectively, which can be interpreted that the intensity peak will not over $10A^2$ and the background noise will be at least $2A^2$ in this case. The periods in the y direction, expressed by Eqs. (5.5) and (5.6), are unchanged, and the period in the x direction is changed from $d_x = \lambda / \sin\theta$ to $d_{x^*} = \lambda / \sin\theta^*$.

The period of dot structures in the TE-TE-TM-TM mode is $d_x = \lambda / \sin\theta$. The

boundary of maximum intensity is $16A^2$ and the minimum intensity is 0, which shows in accordance with the intensities bar in Fig. 5.5. It can be confirmed that the TE-TE-TM-TM mode has the highest intensity and the best contrast. But there is a very obvious modulation. This modulation is mainly caused by slight differences in the incidence angles of the beams. From Eq. (5.9) suggested, two small periods along the x axis can be found. They are $d_1 = \lambda/(\sin\theta + \sin\theta^*)$ and $d_2 = \lambda / \sin\theta$, respectively. In addition, an extra periodical modulation will be introduced in the interference pattern. It can be expressed as $d_3 = \lambda/\left|\sin\theta - \sin\theta^*\right|$.

5.2.2 Effect on the Formation

From the theoretical analysis obtained in the 5.2 section, the effect of polarisation is addressed and given a detailed explanation of spatial distributions in three cases. Matlab is used as a powerful tool for the simulations that visually display the formation of interference patterns.

It can be seen from Fig. 5.5 that the maximum intensities distribute both along the X, Y axes and periodic dots in the TE-TE-TE-TE mode, which is interpreted in the intensity bars of Fig. 5.5(a), (e) and (i). By comparison, the maximum intensities are only focused on the periodic dots in the TE-TE-TE-TM and TE-TE-TM-TM polarisation modes. Moreover, the maximum intensities of TE-TE-TE-TM and TE-TE-TM-TM are higher than those in the TE-TE-TE-TE mode.

To understand the respective modulation of three cases, the incident angle of Beam 3 (Fig. 5.4) is changed from 6° to 9° and resulting patterns are shown in Fig. 5.5(b), (f) and (j). In the TE-TE-TE-TE mode, the dot patterns are changed from square to rectangle shape. In the TE-TE-TE-TM mode, the features of dots have been changed and the distribution of pattern shows a partial similarity to three-beam interference.

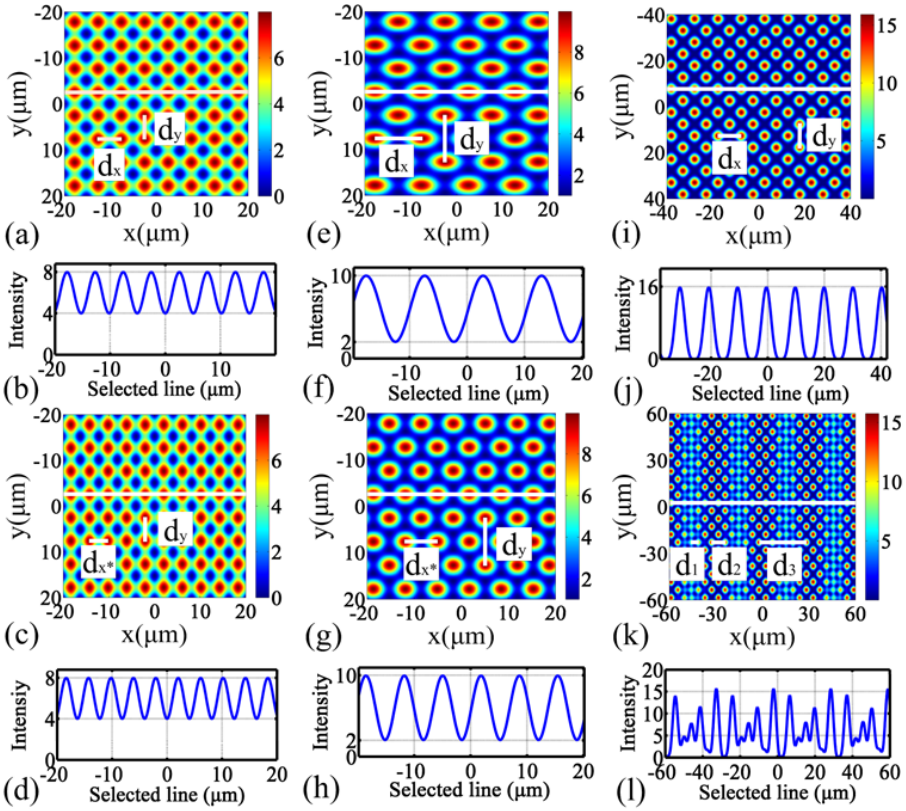

Fig. 5.5 Interference simulation results for three different polarisation modes: (a) TE-TE-TE-TE mode with the identical incident angles; (b) Intensity curve along the double arrows line in (a); (c) TE-TE-TE-TE mode with a misaligned incident angle; (d) Intensity curve along the double arrows line in (c); (e) TE-TE-TE-TM mode with the identical incident angles; (f) Intensity curve along the double arrows line in (e); (g) TE-TE-TE-TM mode with a misaligned incident angle; (h) Intensity curve along the double arrows line in (g); (i) TE-TE-TM-TM mode with the identical incident angles; (j) Intensity curve along the double arrows line in (i); (k) TE-TE-TM-TM mode with a misaligned incident angle; (l) Intensity curve along the double arrows line in (k).

In the case of the TE-TE-TM-TM polarisation mode, an obvious modulation will be produced. The period of modulation is defined as $d_3 = \lambda / \left|\sin\theta - \sin\theta^*\right|$. It can be interpreted from Fig. 5.6 that if the misaligned incident angle is infinitely closed to the normal incident angels, the period of modulation will become larger till the whole pattern tends to uniformity. Another phenomenon as a result of different modulation periods is that compared to the larger incident angles, the incident angles of less than 10˚ suffers from a more obvious modulation, even if the extend of derivation is identified. For example, when $\theta_1=\theta_2=\theta_4=6$˚ and

θ^*=7˚, the resulting period is around 61μm, while $\theta_1=\theta_2=\theta_4$=36˚ and θ^*=37˚, the resulting period is around 76μm. It reasonably brings about a difficult of avoiding the modulation in practice. As for the wavelengths described in the previous publications, the 308nm laser was used in the reference [64, 65], the 355nm laser was used in the reference [56]. According to the equation of modulation period, shorter wavelengths have an alternative possibility of obvious modulations.

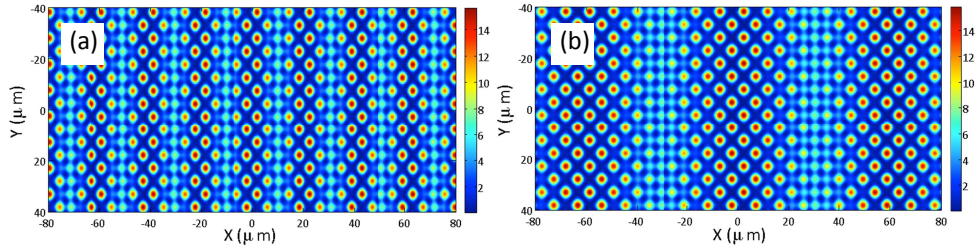

Fig. 5.6 Different modulation periods caused by different misaligned incident angles.

(a) $\theta_1=\theta_2=\theta_4$=6˚, θ^*=9˚; (b) $\theta_1=\theta_2=\theta_4$=6˚, θ^*=7˚.

The theoretical analyses of interference intensities are conductive to understand the distributions in the cases of different polarisation modes. For the TE-TE-TM-TM example, the script of Matlab is written as Appendix A.

5.3 Experimental Investigation

In the experiment, the polished single crystal p-doped (100) silicon was irradiated by using the four-beam laser interference system and the experiments were carried out under ambient conditions. The laser wavelength is 1064nm and the used laser fluence is approximately 0.64J/cm^2. After 60s exposed time, silicon was ablated on the maxima intensity positions.

During the laser treatment, the configuration of the four-beam interference system, i.e. azimuthal angles and incident angles of four beams, is fixed. Only the polarised angles are adjusted by the linear polarisers. The surface morphologies of the samples were characterised with scanning electron microscope (FEI XL30).

5.3.1 Fabrication of the TE-TE-TE-TE Polarisation Mode

The dot or called microcone structures were fabricated in this mode. In the experiment, all the incident angles of four beams are difficult to obtain the strict equality with each other. But an evenly-distributed microcone structures over large area can be achieved in the polarisation mode. The result is shown in Fig. 5.7.

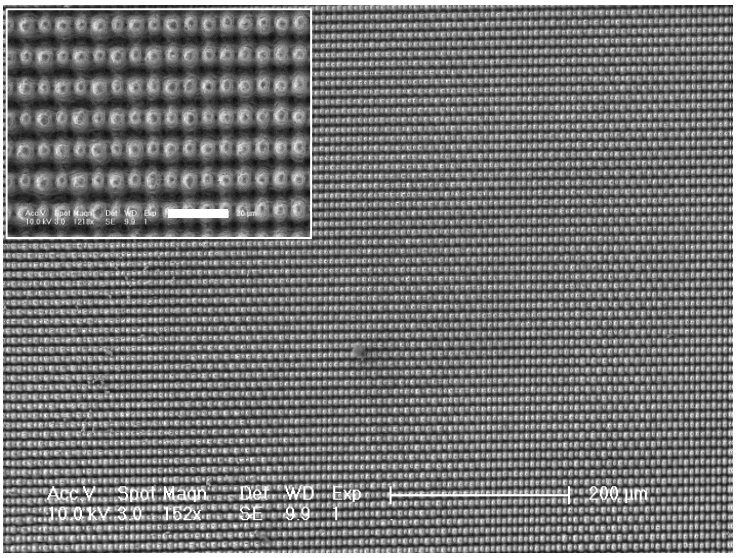

Fig. 5.7 Micrographs of TE-TE-TE-TE four-beam laser interference with 300 pulses and laser fluence=0.64J/cm². The scale bar in the inserted picture is 20μm.

5.3.2 Fabrication of the TE-TE-TE-TM Polarisation Mode

In contrast, microhole structures can be fabricated in the TE-TE-TE-TM mode. The difference between them can be explained by theoretical analysis based on Eqs. (5.2)-(5.3) and (5.5)-(5.6).

5.3.3 Fabrication of the TE-TE-TM-TM Polarisation Mode

Unlike the above two modes, in the TE-TE-TM-TM mode, the modulation have advantages of high peak intensity and the best contrast. But in this case, the patterns can hardly be evenly distributed due to the slight differences of the incident angles. In practice, the modulation is hard to be avoided. To obtain

large-scale uniform structures, the TE-TE-TE-TE mode and TE-TE-TE-TM mode could be better alternatives.

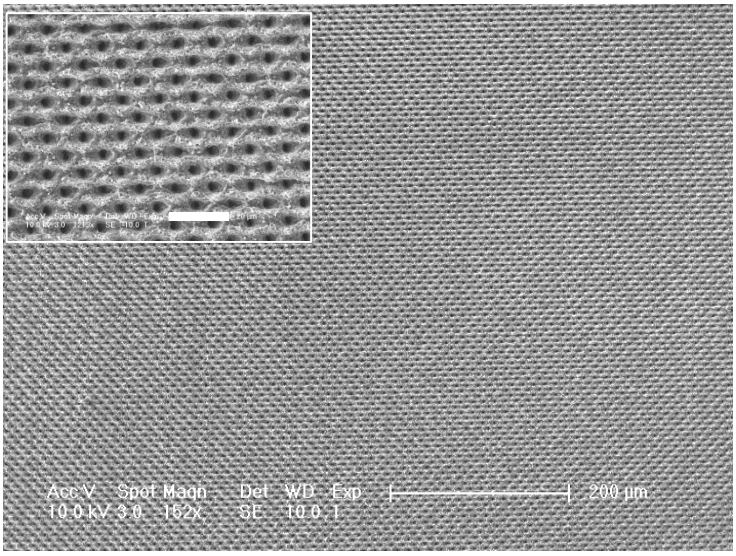

Fig. 5.8 Micrographs of TE-TE-TE-TM four-beam laser interference with 300 pulses and laser fluence=0.64J/cm². The scale bar in the inserted picture is 20µm.

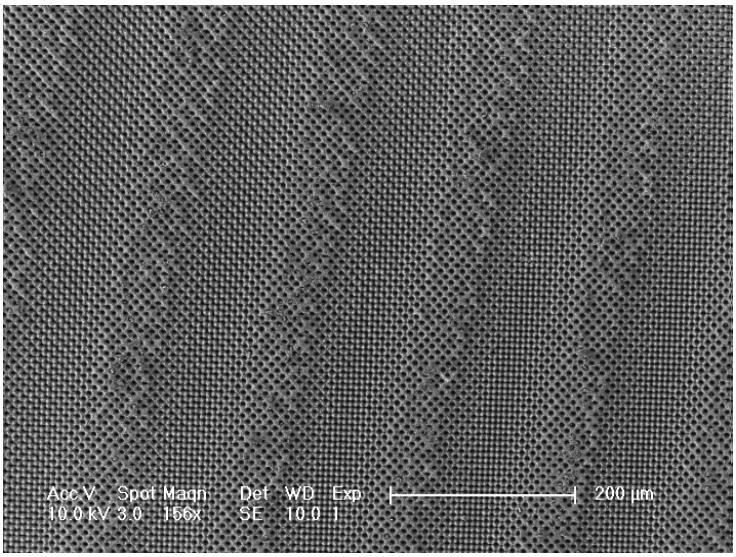

Fig. 5.9 Micrographs of TE-TE-TM-TM four-beam laser interference with 300 pulses and laser fluence=0.64J/cm².

5.3.4 Discussion of formations fabricated by the three polarisation modes

In four-beam interference, the polarisation vector plays a critical role in the formation, contrast and period of interference patterns. To explicate the relation

and difference of three different polarisation modes, the demonstrations in terms of theoretical aspect provide instructive insights to analysing the issue. However, by investigating the state of the art, there is barely record which gives a detailed explanation. All the equations from (5.1) to (5.9) in this chapter are derived on a basis of Eqs. (2.16) and (2.17) and simultaneously refer to the previous work [11, 18-19, 60-61, 64-65]. More details of the methodology can be seen in section 2.4. Once the formulations of intensity distribution in three cases are obtained, the expressions of the contrast and period can be inferred from the internal interfering terms and Matlab enables to realise 2D and 3D visualizations. For the specific incidence condition, e.g. the abnormal or unequal incident angle in the TE-TE-TM-TM polarisation mode, the comparative analyses can reveal the differences with each other.

The experimental observations have shown that microcone structures were fabricated in the TE-TE-TE-TE polarisation mode, while microhole structures were fabricated in the TE-TE-TE-TM polarisation mode. The comparison of simulations and experimental results are illustrated in Fig. 5.10. Two fragments of intensity distribution extracted from Fig. 5.5 (a) and (e) are integrated into Fig. 5.10. In the TE-TE-TE-TE polarisation mode, microcone structures are formed because of the surrounding area ablated by the laser. In the TE-TE-TE-TM polarisation mode, the high-peak maximum intensities produce direct ablation and corresponding microhole structures are fabricated. In this process, interference period is an important parameter as the molten materials at both the maxima positions and minima positions get homogeneous when the period goes down.

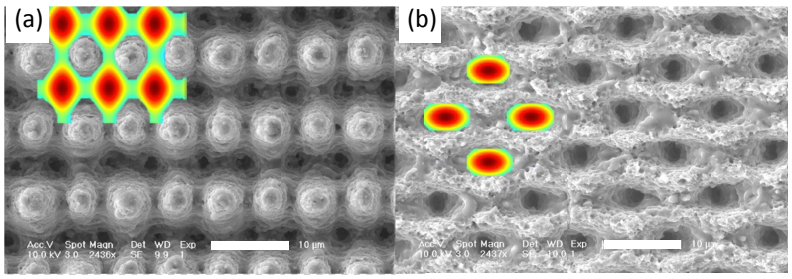

Fig. 5.10 Comparison analyses of the simulations and experimental results. (a) TE-TE-TE-TE

polarisation mode; (b) TE-TE-TE-TM polarisation mode. The scale bars are 10μm.

In the TE-TE-TM-TM polarisation mode, it can be seen that the direction of modulation has a minor slope (Fig. 5.9). The phenomenon could be attributed to the offset of the azimuthal angles. Fig. 5.11 indicates a number of modulations with different conditions of azimuthal angles. Actually, the eventual formation of structures is result of incident and azimuthal factors.

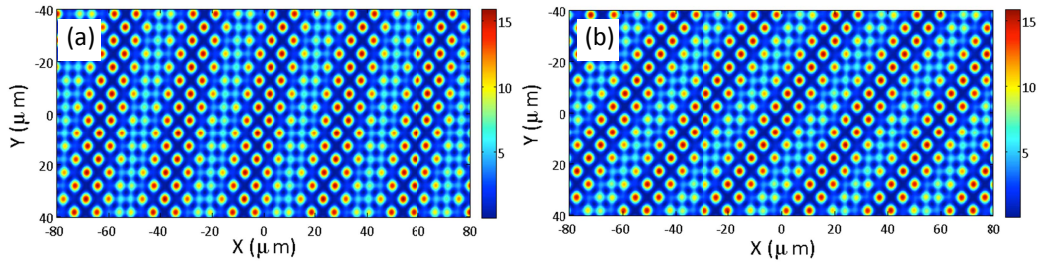

Fig. 5.11 The directions of modulation slop with different azimuthal angels. (a) ϕ_1=0˚, ϕ_2=90˚, ϕ_3=183˚, and ϕ_4=270˚; (b) ϕ_1=-5˚, ϕ_2=90˚, ϕ_3=185˚, and ϕ_4=270˚; ($\theta_1=\theta_2=\theta_4=6^\circ$, $\theta^*=8^\circ$).

5.4 Summary

Through a series of experimental simulations and experiment study in chapters 3 and 4 respectively, the characteristics of multi-beam interference are basically comprehended. While the modulation phenomenon is found in the case of four-beam interference as the further investigation is carried out deeply. Although it has been described by the publications, the remaining challenge is to give a comprehensive explanation of underlying mechanism or avoid the non-uniform structures produced by the modulation effectively and therefore chapter 5 is set up individually.

The effects of polarisation on four-beam laser interference were studied in this chapter. The polarisation plays a key role in the formation of interference patterns, pattern contrasts and periods in four-beam interference and three different polarisation modes are discussed systematically. The resulting patterns have shown a good correspondence with the theoretical analysis and simulations.

The TE-TE-TM-TM mode has the best contrast and highest peak intensity. It is found that the secondary periodicity or modulation in four-beam laser interference is the result of the misalignment of incident angles or unequal incident angles only in the case of the TE-TE-TM-TM mode. Furthermore, the formations of resulting structures are associated with the polarisation modes, e.g. micro or nano cone and hole structures are fabricated in the cases of TE-TE-TE-TE and TE-TE-TE-TM modes respectively. By exploiting the benefits of each case, various applications can be realised potentially. As a consequence, DLIN is demonstrated to be a promising and versatile technique. Based on the achieved outcomes, large-area applications will be studied in the next chapter.

Chapter 6

Large-Area Fabrication and Applications

6.1 Introduction

After an intensive study concerning the theoretical analyses in the previous chapters, a number of meaningful applications are investigated subsequently in this chapter. Since the non-uniform microstructures generated by the modulation effect show a relatively less potential in the large-area applications, the TE-TE-TE-TM and TE-TE-TE-TE polarisation modes are chosen to fabricate the evenly distributed arrays which are suitable for the realisation of optimum property. Section 6.2 mainly discusses with the antireflection structures by means of difference schemes, while a novel characteristic of microcone structures exhibiting both antireflection and superhydrophobicity simultaneously is addressed in section 6.3. Respecting the matters of existing technologies, the comparative results exhibit the advantages of DLIN. More details can be found in the following sections.

As mentioned above, numerous efforts have been made in recent years to fabricate large-area structures on micro and nano scales. Large-area applications with extraordinary properties contribute to the progress from laboratory to industry. Among them, the extensive attentions in many fields have been attracted to antireflection or high absorption structures because they can be widely used in optical detection, solar cells, OLEDs (organic light emitting devices) and high-power laser system. To achieve the function, chemical and physical methods, such as wet chemical etching [69], electrochemical etching, reactive ion etching [70] and nanoimprint lithography [71], have been developed to fabricate the structures. However, the techniques have not the selectivity to substrate without the help of masks. Additionally, some solution and gas sources are quite toxic and corrosive. Recently, another elegant method, femtosecond or nanosecond laser

has been employed to irradiate the silicon surface. Micro spike structures (known as black silicon) were fabricated and its excellent ability of reducing light reflection is attracting more and more attentions. People expect it to open a new door for a wide range of applications.

In this chapter, three different anti-reflection structures were fabricated with the direct laser interference technology under sulphur hexafluoride (SF_6) and air ambiance conditions respectively. The scanning strategy with the four-beam nanosecond laser interference system was applied to realise the wafer-scale fabrication. Due to a larger laser spot and the disturbance-resisting ability for nanosecond laser system, this method is more efficient.

Under the SF_6 ambiance, an array of sharp conical micro spikes was made. By comparison, two periodic structures corresponding to two different polarisation modes were obtained in the air ambiance. To investigate the reflectance of black silicon, microhole and microcone structures, a spectrograph equipped with an integrating sphere was used. It is found that a lower reflectivity is achieved for a higher structure depth. This behaviour may be caused by multiple reflections to improve the amount of light absorbed. Although the reflectivity of black silicon treated by nanosecond laser in the SF_6 ambiance is extremely low, surface photocarrier recombination limits the conversion efficiency due to a high impurity concentration. As an alternative, direct laser interference technology is used to produce well-ordered periodic structures on the material surface in the air ambiance.

Furthermore, in order to realise the extraordinary functions of both self-cleaning and antireflection simultaneously, we propose a straightforward method to fabricate well-defined micro and nano artificial bio-structures compared to the existing technologies. The proposed method of direct laser interference nanomanufacturing (DLIN) takes a significant advantage of high efficiency as only a single technological procedure is needed without pretreatment, mask and pattern transfer processes. Meanwhile, the corresponding structures show both

antireflection (AR) and superhydrophobicity properties simultaneously. The developed four-beam nanosecond laser interference system configuring the TE-TE-TE-TE and TE-TE-TE-TM polarisation modes was set up to generate periodic micro cone and hole structures with a huge number of nano features on the surface. The theoretical and experimental results have shown that the periodic microcone structure exhibits excellent properties with both a high contact angle (CA=156.3˚) and low omnidirectional reflectance (5.9-15.4%). Thus, DLIN is a novel and promising method suitable for mass production of self-cleaning and antireflection surface structures.

6.2 Antireflection structures

6.2.1 Related Work on Black Silicon Fabricated by Femtosecond Laser

Silicon is one of the most important materials for the semiconductor industry. In the matter of many applications, e.g. solar cells, infrared detectors, CCD and other categorised semiconductor devices, surface reflection is a limited factor for the optoelectronic performances with lack of collecting light. In the past, it was found that surface texturing could reduce the surface reflection of light and increase absorption. In 1998, Eric Mazur group reported a novel material, namely black silicon. It was obtained by femtosecond laser processing of crystalline silicon surfaces in the presence of ambient gases SF_6 or Cl_2 [72]. With a number of investigations of black silicon, it was proved to have an excellent antireflection property and the absorbance from near-ultraviolet to the near-infrared can be increased over 90%. Black silicon has potential applications such as high sensitivity infrared photodiodes, high quantum efficiency photodiodes, field emission devices and photovoltaic cells. In order to interpret the mechanism of laser-induced etching, fowlkes et al. found there was a dynamic interplay between the formation of microholes and microcones [73]. The SF_6 total and partial pressures have a pronounced effect on the growth of cones. This fact is an indication that it is the laser-generated plasma that controls the cone growth.

Shen et al. fabricated ordered arrays of silicon microspikes (microcones) with a periodic mask, as shown in Fig. 6.1 [74].

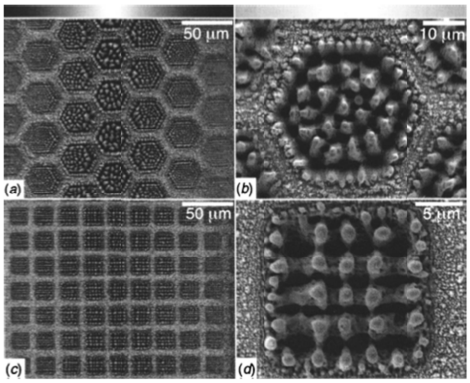

Fig. 6.1 Scanning electron micrographs of ordered silicon spikes formed by masking the irradiated sample with (a), (b) a 30-μm hexagonal grid and (c), (d) a 20-μm square grid. The nearly Gaussian spatial intensity profile of the laser pulse is shown at the top in grayscale white corresponds to maximum intensity. (Shen et al. 2003)

A femtosecond laser (wavelength=800nm, pulse width=100fs) was focused to a beam waist of 200μm at the sample surface in their experiment. Due to the Frensel diffraction of light from the mask aperture, the capillary waves in the molten silicon are regarded as the mechanism for forming the coarsened structures. In the early stage of discover of black silicon, a number of publications focused on the underlying mechanisms for formation and enhanced-absorption with a broadband spectrum [75-77].

Recently, black silicon has been applied for various optoelectronic devices, e.g. solar cells, as a result of a dramatic reduction of reflectance [78]. Bao et al. fabricated active area of 40mm^2 samples by femtosecond pulse laser in ambient gas of SF_6 [79]. After laser treatment, the samples were thermally annealed in vacuum at 825K for 40 minutes to eliminate defects in silicon lattice. A comb contact was deposited through a mask on the front side and a thin Al film on the back side. The photovoltaic responses of black silicon samples were measured by using a He-Ne laser as an excitation source. It was found that the open circuit for one of the samples was 53.3mv and corresponding short current was -0.11mA,

which means that the external quantum efficiency (EQE) of sample was as high as 112.89%. The black silicon opens a new door for the promising applications on the solar-thermo electric generating system such as concentrating solar power (CSP) parabolic trough [80].

However, femtosecond laser processing technique takes a time consuming strategy. The laser is focused by a high numerical aperture (NA) mirror as the energy fluence of initial source is not sufficient to reach the damage threshold, so the irradiate area is limited. Herein, the method of quasi-periodic black silicon antireflection surface structures fabricated by DLIN is presented. For experimental counterparts, well-defined microcone structures are produced in the air ambiance. The scheme of experimental setup is shown in Fig. 6.2.

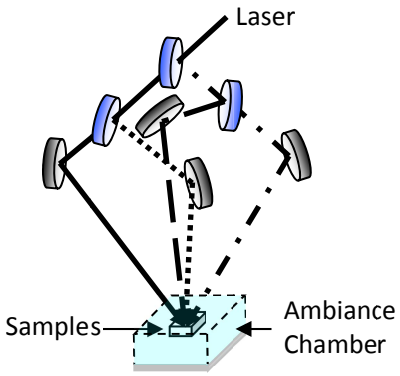

Fig. 6.2 Schematic set-up for the four-beam laser interference, different dotted lines refer to each optical path and a chamber is used to fill with gas ambiance.

6.2.2 Black Silicon Fabricated by Four-beam Laser Interference

As shown in Fig. 6.3, the conical spike structures are fabricated in the atmosphere of SF_6 gas. It can be known that SF_6 has a strong fluence of the structural morphology. During the irradiation of high peak power laser, SF_6 gas will be ionized into F^+, SF^+, SF_3^+, SF_5^+ and so on. Then F^+ ions react with silicon to form volatile SiF_4 which escapes from substrate. The whole process can be regarded as the chemical etching assisted by laser. Thereby, the process lacks the selectivity and the pattern loses the uniform. In the experiment, the SF_6 may have two effects. One is as a reaction gas involved the ablation process, aggravating the

etching level. The other is the formation of shields to avoid oxidation.

It can be known that SF_6 has a large influence on the resulting microcolumn morphology. SF_6 contributes to the generation of the melted droplet-shaped features on the top of conical spikes that growth on the periodic black silicon surface. Irradiation in the laser interference region induced decomposition of SF_6 and produced F_2 that diffuses in the highly heated substrate. The F_2 reacted with silicon and formed the volatile SiF_2 at the bottom of ablation holes. Then volatile SiF_2 could react later on the tip and sides of the conical spikes reform monocrystalline silicon.

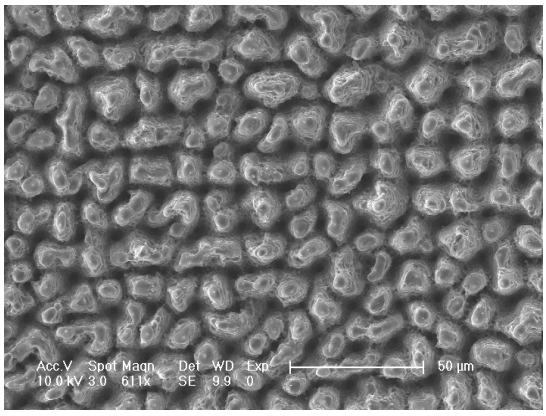

Fig. 6.3 SEM image of black silicon structures fabricated in SF_6 ambiance.

6.2.3 Fabrication of Microcone and Microhole Structures

According to the results of Chapter 5, two resulting structures on the silicon surface can be fabricated corresponding to two polarisation modes.

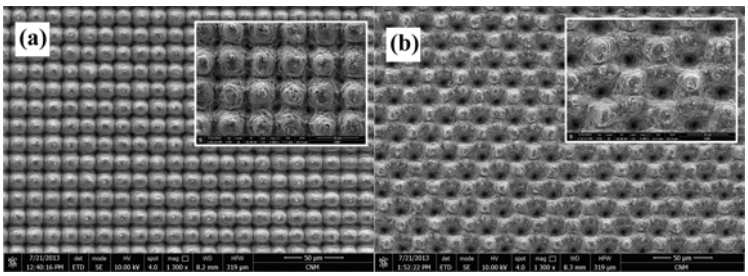

Fig. 6.4 (a) Cone structures; (b) Hole structures fabricated by the direct four-beam laser interference system with the TE-TE-TE-TE and TE-TE-TE-TM polarisation modes, respectively. The

insert images are 5000× magnification.

Fig. 6.4 illustrates the typical microcone and microhole structures. Generally, the exposure needs only 10-40 seconds with the laser fluence of around 400-1000mJ/cm^2. This means that DLIN can be regarded as a promising approach for the applications of high throughput and low cost.

The period of microcone structures can be changed by different incident angles. From Fig. 6.5 shown, the four incident beams follow a symmetrical configuration with the azimuthal angles of $\phi_1 = 0°$, $\phi_2 = 90°$, $\phi_3 = 180°$ and $\phi_4 = 270°$, and all the polarised angles of four beams are 90°. As to incident angles, two different cases of $\theta_1 = \theta_2 = \theta_3 = \theta_4 = 5°$ and $\theta_1 = \theta_2 = \theta_3 = \theta_4 = 4°$ were set, resulting in the approximate periods of 6μm and 15μm respectively. In the experiment, the laser fluence was utilised as 0.64J/cm^2 and the number of pulses was 300.

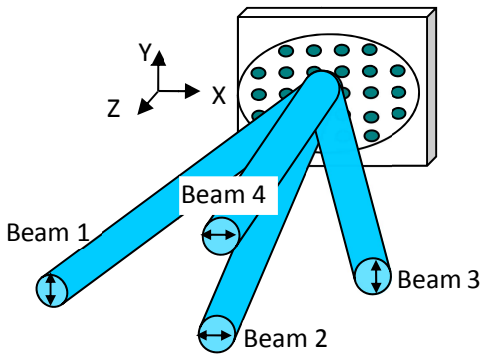

Fig. 6.5 The configuration of the four-beam laser interference in TE-TE-TE-TE polarisation mode. The double-headed arrows refer to the oscillating directions of the electric vectors.

In this case, surface temperatures between maximum and minimum intensity positions are not identical, bringing about a periodic ablation where the regions reach the value of melting or vaporisation points. Consequently, microcone structures adhering nanoparticles on the surface were fabricated, shown in Fig. 6.6.

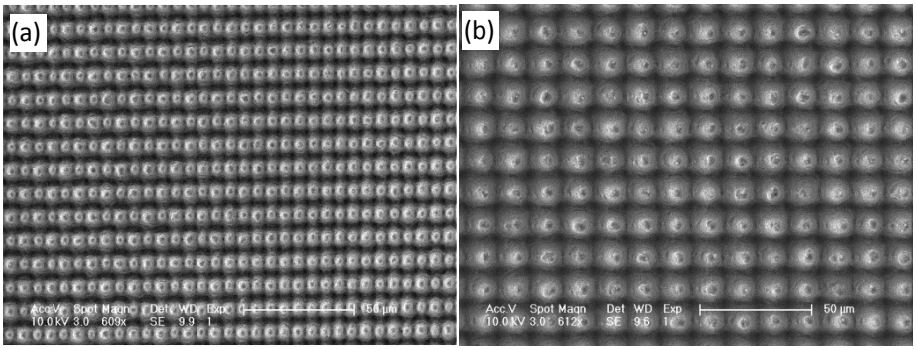

Fig. 6.6 SEM micrographs of microcone structures fabricated by direct four-beam laser interference technology: (a) period of 6µm; (b) period of 15µm.

6.2.4 Reflectance Measurements of three structures

A reflectance measurement system was setup to analyse the diffuse reflectivity value quantitatively. The schematic is shown in Fig. 6.7. An integrating sphere covered with a diffuse white reflective coating was added into the system. By multiple scattering reflections, any point on the inner surface is distributed equally to all other points. In addition, the main specifications of spectrometer and electrochemical workstation used in the experiment are listed in Table 2.

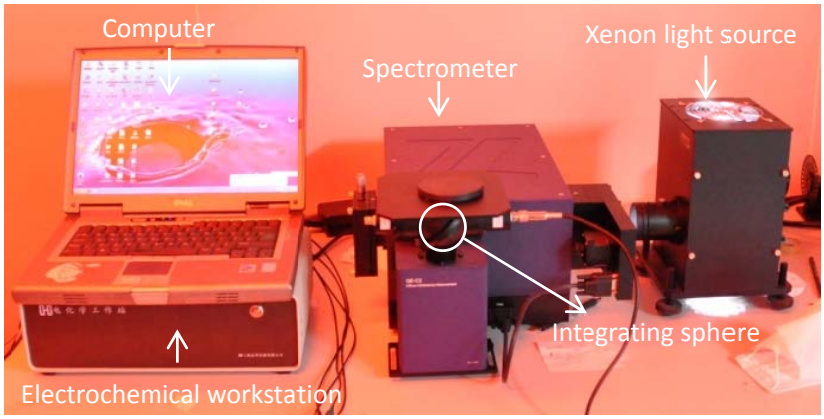

Fig. 6.7 The system setup of spectral responsivity by spectrometer equipped with an integrating sphere.

Table 2 Main specifications of spectrometer and electrochemical workstation.

Spectrometer	Specifications	Electrochemical workstation	Specifications

Focal length	300mm	Pulse width of CA/CC	0.0001 to 1000s
Resolution	0.1nm	Min sampling interval of CA/CC	1μs
Accuracy	0.2nm (1200 g/mm grating)	Pulse width of DPV/NPV	0.001 to 10s
Repeatability	0.1nm	SWV frequency	1 to 100KHz
Wavelength Range (nm)	200-2500nm	i-t min sampling interval	1μs

The reflectance is the fraction of incident electromagnetic power reflected from a specific sample and determined by the Eq. (6.1).

$$R_m = \frac{I_m}{I_s} \cdot R_s \quad . \tag{6.1}$$

where I_m is the current value of measured samples detected by electrochemical work station, I_s is the current value of standard plate specimen detected by electrochemical work station and R_s is the reflectivity of a calibrated standard specimen. The date of standard plate for reflectivity corresponding to wavelength is shown as Appendix B.

First, the reflection performs of microcone and microhole structures are investigated. Fig. 6.8 shows the measured curves. It indicates that both cone structures and hole structures have a lower reflectance than the original silicon surface (around 35%) as more light can be absorbed by lengthening the optical path or multiple reflections. In addition, the reflectance of microcone structures is lower than that of the microhole structures. Halbwas et al. simulated the reflectance performance of four different structures, and concluded that the spike or cone structures were better in terms of light absorption [81]. In order to obtain large-scale uniform cone structures, the TE-TE-TE-TE polarisation mode can be an alternative.

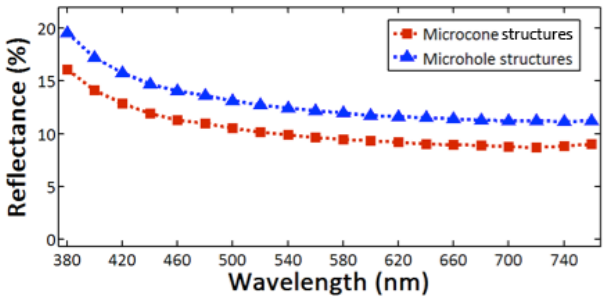

Fig. 6.8 Reflectance measurements of the microcone and microhole structures.

The reflectivity of black silicon and microcone structures was measured by the system. Fig. 6.9 shows that the reflectivity of black silicon is only several percent over the visible spectral range and it is responsible for the black appearance. It is also noticeable that microcone structures display light-trapping property. D'Alessandria et al. has demonstrated higher structure depths achieved for large periods based on simulations and experiments [51]. Multireflection inside deeper microcones contributes to iterative absorption. Therefore, microcone structures with the period of 15µm have a lower reflectivity than those of 6µm.

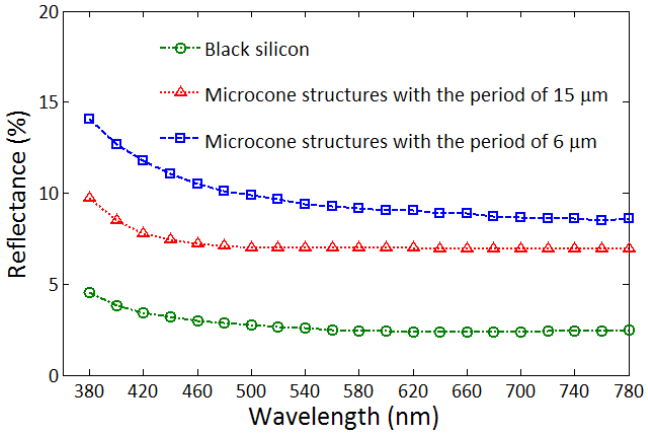

Fig. 6.9 Reflectance of three different structures as a function of wavelength.

A number of previous studies show that a high density of sulphur atoms in the sulphur hexafluoride gas is doped in silicon under laser irradiation [78, 80, 82]. The "dead layer" will reduce quantum efficiency due to the high enhancement of photocarrier recombination. In contrast, well-defined structures can be fabricated by direct laser interference technology in air after the hydrofluoric (HF)

acid was employed to wipe off the silica.

6.3 Investigation of Both Anti-reflection and Superhydrophobicity Functional Surfaces

6.3.1 Motivation

Triggered by the fantastic surfaces of nature, such as the anisotropy of the rice leaves [83], the iridescence of the butterfly wing [84], the self-cleaning of the lotus leaves [21, 27, 85], and the antireflection of Moth-eye [86, 87], the fabrication of artificial bio-structures has become a hot topic, attracting more and more attention in various fields [88-93]. The potential applications demand high efficiency and low cost techniques to realise the extraordinary functions and fulfil the macroscale fabrication [77, 94-98].

Up to now, great efforts have been devoted to study the hierarchical micro and nano structures, which are generally regarded to the critical reason for multifunctional realisation. On the one hand, Wu et al. achieved the controlled anisotropy wetting structures on the photosensitivity resist [29]. They investigated the anisotropic wetting property on grooves with different line widths, periods and heights of structures fabricated by LIL. Specially, it was found that the controlled behaviour strongly depends on the height. Finally, the perpendicular CA was enhanced to 131˚±2˚ by using their method. Wang et al. fabricated the grating structures on graphene surfaces (CA=156.7˚) by two-beam interference method and the structures also showed iridescence behaviour [84]. They pointed out that the results contribute to the design of colourful superhydrophobic surfaces and understanding of interaction at liquid-graphene interface. Wu et al. obtained a high contact angle (CA=175˚) at the cost of time consuming strategies, i.e. laser interference, photolithography, PDMS transfer and plasma treatment, as shown in Fig. 6.10 [28]. Three different microstructures, 20μm pitch pillar arrays, 2.5μm periodic pillar and gecko foot-like hierarchical structures, were fabricated. With the analysed of Wenzel's and Cassie's models, the hierarchical structures

show the highest CA (CA=175˚) and anti-oil property as well. Another strategy consisting of the complicated procedure, i.e. deposition by E-beam evaporator, annealing, RIE, and particles removal, was reported by son et al. [99]. Both nanopillar and nanohole structures on the glass substrate were fabricated and the samples after coating of PFTS (chemical functionalization with 1H, 1H, 2H, 2H-perfluorodecyltriethoxysilane) show a high CA of 167˚-170˚.

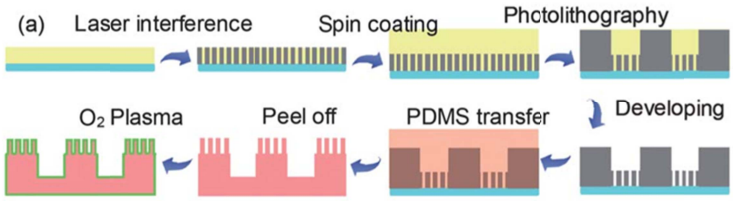

Fig. 6.10 The fabrication scheme of gecko foot-like arrays. The main fabrication process: laser interference, photolithography, and PDMS transfer. (Wu et al. 2011)

On the other hand, Mei et al. fabricated the black silicon using a scanning femtosecond laser under the sulphur hexafluoride (SF_6) gas ambiance condition and the absorption in the visible region was as high as 97% [100]. Oh et al. fabricated the silicon nanowire and nanopore arrays by a two-step metal-assisted etching technique [101]. Although the optical reflectance was down to 3%-11%, photogenerated charge collection was limited due to the surface recombination and Auger recombination. For the other light-trapping structures that are attributed to the mechanism of the plasmonic resonant, Fan et al. reported that they used FIB facility to fabricate the aluminium nanocuboids [102]. The resulting structures have the period of 160nm, width of 80nm and height of 80nm. It was found that the average absorbance of TM light was higher than that of TE light and the absorbance of TE light decreased with increasing incident angles. In their spectra measurement, the states of polarisation light and incident angle were mainly discussed. But in practice, natural light which is absorbed by solar cells is almost non-polarised state and omnidirectional. Recently, people inspired from Moth-eye structure to mimic the bio-structure. Ji et al. proposed a method containing four steps: prepare a layer of colloidal polystyrene (PS) nanoparticles

as a mask, size reduction of PS with O_2 plasma treatment, deep etching with CF_4 and H_2 plasma etching, and removal of PS with two cleaning processes [87]. Due to depend on the PS as an etching mask, the formation of fabricated structures is random. Impressively, 99% transmission was achieved on the glass substrate fabricated on the front and back sides. Subsequently, they further investigated the geometrical parameters of Moth-eye structures, such as height, periodic distance, shape, and arrangement in the reference [103]. In the conclusion, they suggested that periodic nanopillar arrays are more effective for light transmission than random nanopillar arrays.

Compared with them, to date, there is still a lack of a straightforward technique for realisation of both antireflection and superhydrophobicity simultaneously, especially considering the cost and production efficiency. For this reason, a straightforward method to fabricate well-defined micro and nano artificial bio-structures in this work was put forward. The developed four-beam nanosecond laser interference system configuring the TE-TE-TE-TE and TE-TE-TE-TM polarisation modes was set up to generate periodic micro cone and hole structures with a huge number of nano features on the surface. The results have shown that the periodic microcone structure exhibits excellent properties with both a high contact angle and low omnidirectional reflectance.

In recent years, lots of efforts have been focused on the omnidirectional high absorption of solar cells to achieve higher conversion efficiency. But the problem of incident energy loss caused by dust accumulation has not been properly addressed. In practice, not limited to solar cells, photoelectric sensors, detectors and other optical devices which are exposed under the surrounding environment all require a long-term and effective solution to overcome this problem. With the detailed analysis of experimental results, the microcone structure exhibited excellent properties with both a high contact angle (CA=156.3˚) and low omnidirectional reflectance (5.9-15.4%). Consequently, DLIN provides a new way for the fabrication of both antireflection and superhydrophobicity functional

structures.

6.3.2 Experimental Results

The experiment was carried out in the air and the parameters of the laser fluence, number of pulses and period of structures used in the experiment are listed in Table 3. Contact angles (CA) were measured by a contact angle measurement system (JGW-360A) and the surface topography of structures was characterised by a scanning electron microscope (SEM/FEI Quanta 250 FEG).

Table 3 Laser fluence, number of pulses and period of samples in the experiment.

No.	Laser fluence	Number of pules	Period
1	710mJ/cm^2	200	6.7μm
2	710mJ/cm^2	300	6.7μm
3	710mJ/cm^2	400	6.7μm
4	710mJ/cm^2	200	14.2μm
5	710mJ/cm^2	300	14.2μm
6	710mJ/cm^2	400	14.2μm

The laser fluence and exposure time were two important parameters which have a strong influence on the structural features and performances of both the reflectance and CA. In the experiment, a series of laser fluences were applied to determine the proper value of modification for the silicon. When a relative low fluence is used, the material is ablated with the need of more pulses so the efficiency is low. By increasing the laser fluence, more energy is absorbed by the material and the relative temperature between the interference maxima and minima will decrease. As a result, the whole irradiation area could be regarded as an evenly-distributed hot source and the periodic structures tended to form an irregularly ordered pattern [104]. Finally, the laser fluence of 710mJ/cm^2 was chosen to analyse the effects of the period and exposure time on the reflectance and CA performances.

With the laser fluence exceeding the material modification threshold, significant textures on the silicon surface were observed with less than 100 pulses. The

structures were formed homogenously over the laser spot area. As the laser pulses further increased in number, the texture became more pronounced and the ability of light-trapping was improved. The incident angels of $\theta_1=\theta_2=\theta_3=\theta_4=4.6°$ and $\theta_1=\theta_2=\theta_3=\theta_4=2.1°$, and the structure periods were 6.7μm and 14.2μm respectively. Meanwhile, the exposures of 20s, 30s and 40s were chosen to determine the optimal dose. The reflectance performance of the samples in the visible spectrum was measured as solar cells mainly absorbed the light of this range, as shown in Fig. 6.11.

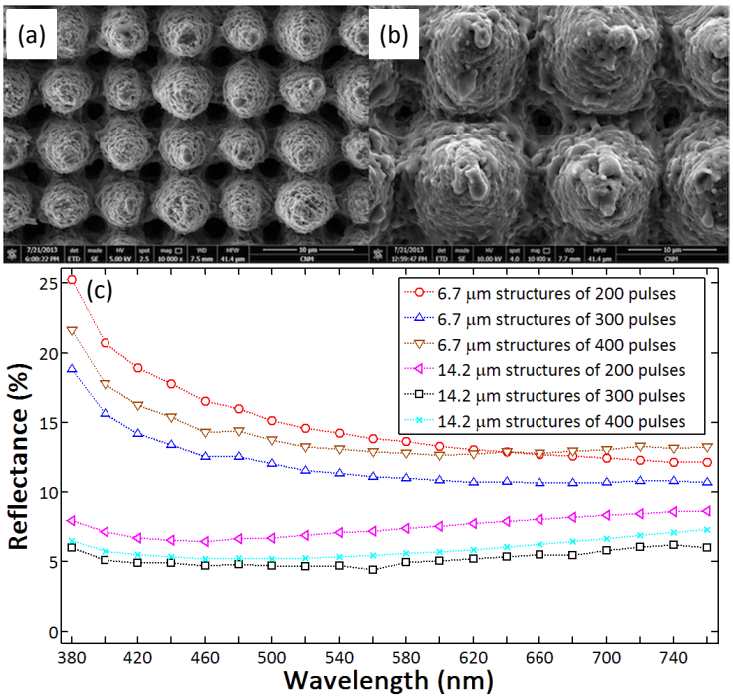

Fig. 6.11 Topographies of structures (a) Period of 6.7μm; (b) Period of 14.2μm; (c) Reflectance spectra of the two microcone structures with exposures of 20s, 30s and 40s. The scale bars are 10μm in (a) and (b).

Fig. 6.12 shows the structural depth of microcone structures as a function of the number of pulses for the structures with two different periods. The average depths of 14.2μm structures are larger than those of 6.7μm structures. With the accumulation of pulses, the structural depths increase but they tend to reach the stabilization at a level of 30s-40s exposures.

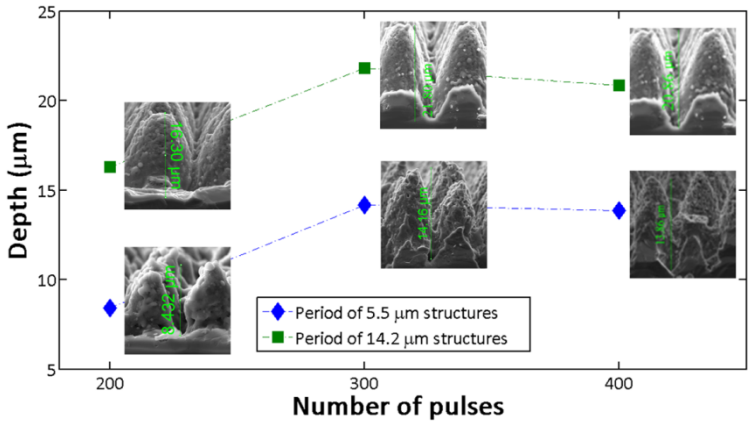

Fig. 6.12 Structural depths of samples as a function of the number of laser pulses.

A finite different time domain (FDTD) method was employed to analyse the reflectivity behaviour and simulate the power absorption profiles [105]. The model was built up according to the structural parameters achieved in the experiment. The simulations of reflection and absorption for 6.7μm period structures with three depths of 8μm, 12μm, and 14μm were performed. Fig. 6.13(a) shows the cross-profiles calculated by the FDTD model and the corresponding quantitative results are shown in Fig. 6.13(b). It is demonstrated that the deeper structures have lower reflection and higher absorption features, which is in accordance with the experimental results.

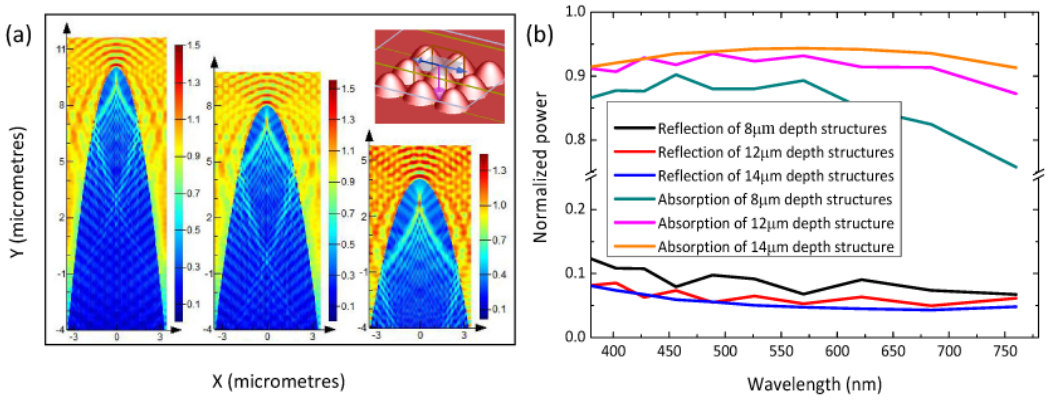

Fig. 6.13 (a) Power absorption cross-profiles of the structures with three depths, the inserted image is the model calculated by FDTD; (b) Normalized reflection and absorption of 6.7μm period structures with three depths of 8μm, 12μm and 14μm.

The special ability of water repellent plays a significant role in our daily life as the superhydrophobic surface can avoid contamination and erosion [106]. The microcone structures show not only the property of antireflection but also the property of superhydrophobicity at the same time. With the investigation of morphology, multi-scale structures in which there are a huge number of nanostructures on the top of microcones are observed by SEM. The process of direct laser interference ablation involves melting, vaporisation and solidification. The sufficient energy of incident laser causes the direct bond breaking of molecular chains in single or multi-photon mechanism, resulting in a huge number of molecular fragmentations. Fig. 6.14(b) shows the typical nanostructures whose sizes are around 100nm. Compared with the ordered microstructures, the hierarchical nanostructures enable reducing the solid-liquid contact area and increasing the CAs [44]. During the laser processing, a large volume of heat gave rise to chemical reactions between Si and O_2. In this case, hydrofluoric acid (concentration of 5%) was employed to wipe off silicon oxides for several minutes. Fig. 6.14 shows the typical SEM images of superhydrophobic structures.

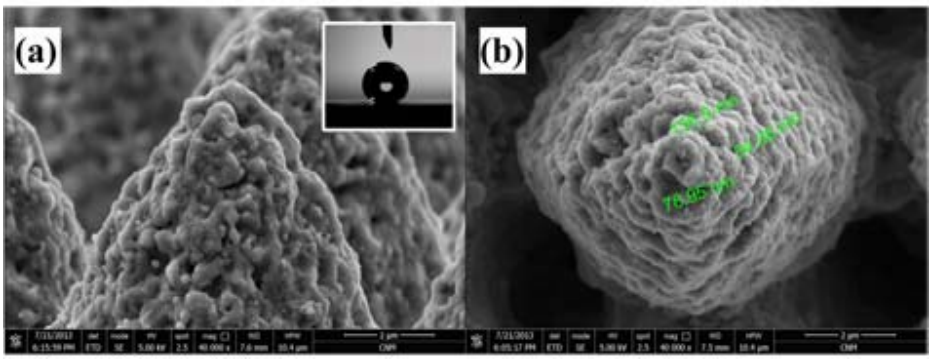

Fig. 6.14 Typical SEM images of superhydrophobic structures with nano features on the surface. (a) Lateral view; (b) Top view. The inset is the measurement of CA.

The theoretical CA of a water drop can be calculated based on the Cassie-Baxter model. The number of dots of the image in Fig. 6.11(a) is 24 in the area of 40×25μm^2. The average diameter of the micro feature point is 2μm. The result value of ψ_L is 0.048. The water CA of the untreated Si surface is 84.5°. According

to Eq. (2.15), the calculated water CA is about 161.3°, which is close to the experimental results. By comparison, the CAs of 6.7μm period structures are larger than those of 14.2μm period structures, as shown in Fig. 6.15. That is attributed to the fraction of the solid contact area.

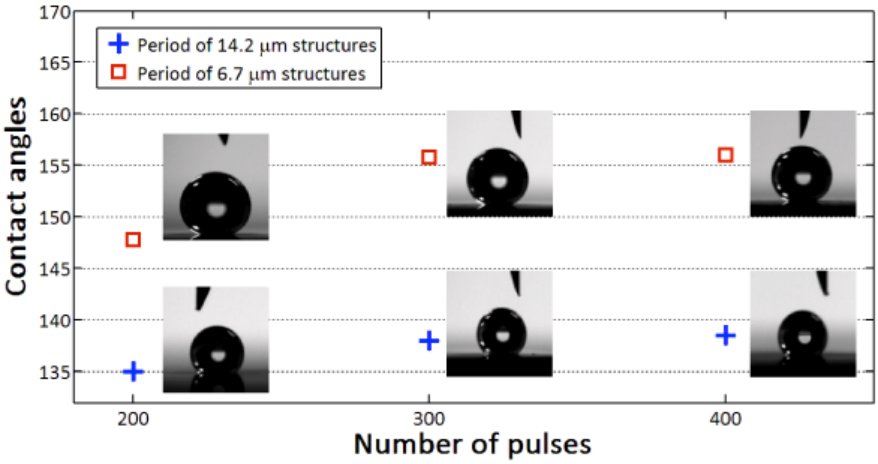

Fig. 6.15 The CAs of microcone structures as a function of the number of pulses.

6.4 Strategy of Beam Overlapping and Large-area Fabrication

Since the last several years ago, a research group from MIT has developed scanning-beam interference lithography (SBIL), which can be described as a hybrid between IL and mechanical ruling [107]. Its basic premise is to generate large-area grating structures by exposing a photoresist-coated substrate. Compared with their work, there are two different features in my thesis. First, the grating structures were focused on and their aim was to fabricate the ultralow distortion nanoruler. Second, they used a continue laser to expose the photoresist. Generally, the exposure time needs several seconds and the phase-shifting caused by air disturbance is hardly avoided. The optoelectronic modulators (Pockels cells) or acousto-optic modulators (AOMs) has to be used in the experiment to realise the fringe locking, while the nanosecond laser is utilised in my task. Without the need of pattern transfer and phase control system, periodic line or dot structures on the substrate can be fabricated only within 6-8 nanoseconds.

SBIL takes the parallel and perpendicular scanning strategies to write the large-area gratings through the movement of high accuracy stage at the same speed of v [108]. Herein, a point by point (the diameter of single point is approximate to 1cm) scanning strategy is applied to attain the wafer-scale fabrication, as shown in Fig. 6.16(a). In the most basic scheme, the condition of beam overlapping is of importance to the uniformity of the whole pattern and property of antireflection. Due to the Gaussian nature of the laser beams it is necessary to overlap neighbouring scanned points to achieve a uniform exposure does on the substrate. In this case, the linear displacement of one step (shown in Fig. 6.16(b)) and pulse number treated with one point (dwell time) are key parameters.

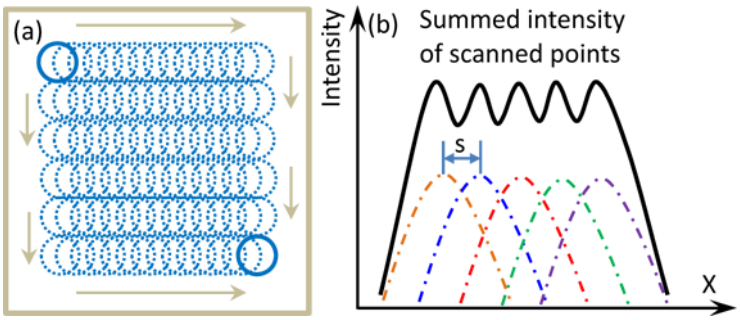

Fig. 6.16 Schematic description of the writing strategy in large-area fabrication. (a) Beam overlapping under point by point condition; (b) Schematic of intensities distribution within the overlapping region.

To determine the condition of optimum overlapping, different linear displacements of scanned overlapping and dwell times were used in the experiment. Fig. 6.17 shows the comparison optical micro images of different linear displacement. When the displacement was set too long, there would be blank regions unexposed and a trail of imprints. Importantly, the displacement of a single step is set an integral multiple of interference period. Given the conditions of laser fluence, period, pulse number (dwell time), the displacements of scanned overlapping (s) are investigated with a series of values setting in the precision stage.

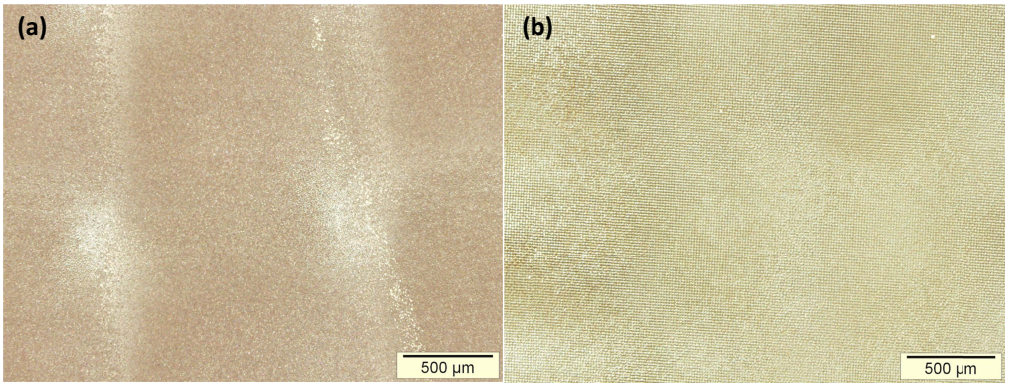

Fig. 6.17 Comparison optical images. (a) the linear displacement of scanned overlapping is approximately 1.5mm; (b) the linear displacement of scanned overlapping is approximately 1mm.

In the experiment, laser fluence of 700mJ/cm^2 was used with the repetition rate of 10Hz and the resulting period of four-beam interference was 20µm. From Fig. 6.18 shown, the reflectance declines with the decrease of displacement of scanned overlapping till reaches equilibrium at the value of 0.8mm. It can be attributed to overexpose to form the collapsed structures at the overlapping positions.

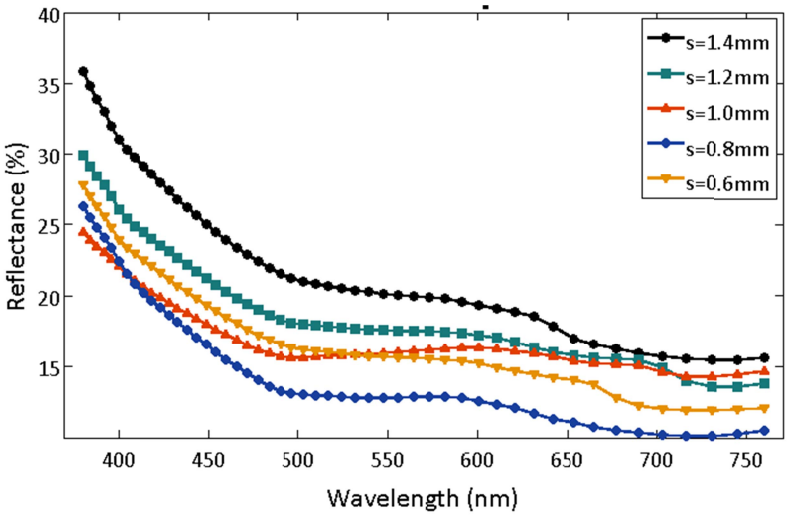

Fig. 6. 18 Wavelength as a function of reflectance with different linear displacements of scanned overlapping.

According to the optimum condition of overlapping, large-area antireflection structures were fabricated under SF_6 gas ambiance and the reflectance spectra were measured from near-UV (200nm) to near-IR (2000nm) using Perkin Elmer

lambda950 spectrophotometer with 60mm diameter integrating sphere. For comparison, the reflectance spectra of unstructured monocrystalline silicon surface and typical texture etched wafer using 2% NaOH concentration with 80 minutes were measured. From Fig. 6.19 shown, the average reflectance is below 3.5% in the measured wavelength range from the ultraviolet to the infrared. Hence, the excellent property of black silicon is suitable for the antireflection applications. The proposed method of direct laser interference nanomanufacturing (DLIN) takes a significant advantage of high efficiency as only a single technological procedure is needed without pretreatment, mask and pattern transfer processes.

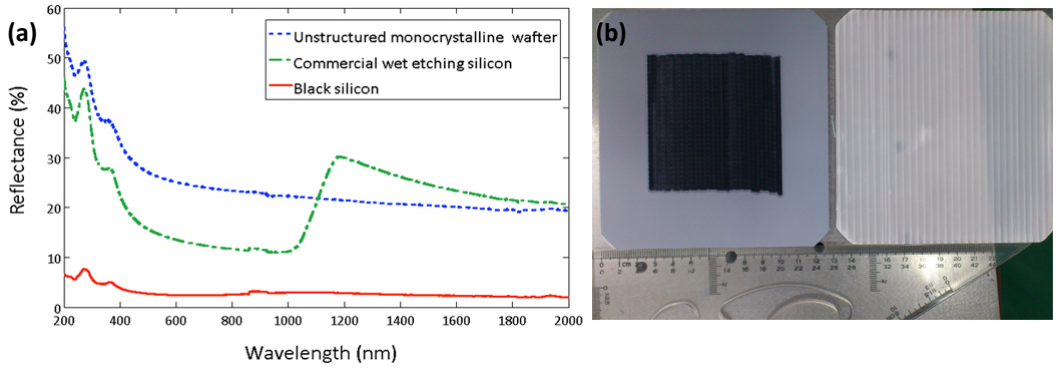

Fig. 6.19 (a) Measured reflectance spectra of large-area samples; (b) 6 inches silicon sample fabricated by DLIN under SF_6 gas ambiance.

It's worth pointing out that the whole fabrication process only costs 10-40 seconds in an area of $1cm^2$ approximately. In terms of the efficiency, DLIN shows a more powerful potential than EBL, FIB and so on. It is demonstrated that DLIN is suitable for mass production. The resulting structures demonstrated in this chapter are basically associated with large-area applications on micro scale. In the experiment, the wavelength of laser was 1064nm. The longer wavelength laser is used, the larger the period is produced. Additionally, in order to obtain the antireflection property, the deeper structures are fabricated in the larger period case. There is another flexible characterisation of interference technology that the scale of resulting structures can be adjusted by changing the used

wavelength. To further explore the capability of DLIN, the high-resolution nanostructures will be investigated by the 266nm laser interference system in the next chapter.

6.5 Summary

This chapter focuses on the large-area applications. Firstly, DLIN technology was investigated to generate three different anti-reflection structures over large area. Although the black silicon fabricated under SF_6 gas ambiance shows a better anti-reflection performance, the surface photocarrier recombination limits the conversion efficiency due to a high impurity concentration. Alternatively, microcone structures fabricated with the developed four-beam laser interference technology in the TE-TE-TE-TE polarisation mode have the capability of trapping the light as well.

Moreover, triggered by the fantastic surfaces of nature, DLIN was used to fabricate the artificial bio-structures on silicon surfaces. Both antireflection and superhydrophobicity behaviours exhibited by microcone structures were systemically studied. The average reflectance of 14.2μm periodic structures is from 5.9% to 8.8% while the average reflectance of 6.7μm periodic structures is from 13.6% to 15.4% over the spectral range from 380nm to 760nm. It was found that the reflective performance was dependent on the structural depth, and deeper structures were achieved for larger periods. This phenomenon can be explained as a consequence of the thermal effect. The relationship between the CAs and structural parameters were investigated as well. Theoretically, the fraction of solid surface area has a strong impact on the CAs. In practice, the structures with smaller periods resulted in smaller solid surface area fractions. Consequently, the microcone structure exhibited excellent properties with both a high contact angle (CA=156.3°) and low omnidirectional reflectance (5.9-15.4%). In conclusion, DLIN features direct ablation of micro and nano structures on substrates without the need of pretreatment, mask and pattern transfer processes, and it provides a new way for the fabrication of both antireflection

and superhydrophobicity functional structures.

With respect to large-area application, DLIN has the capability of wafer-scale fabrication (6 inches) utilising the overlapping strategy. For different structural periods, the optimum condition of overlapping can be found by a number of steps, i.e. scanned displacement and dwell time. The experimental results demonstrate that by means of the approach DLIN enables to achieve large-area fabrication and mass production.

Chapter 7

High-Resolution Fabrication and Applications

7.1 Introduction

As for the conventional LIL, an effective way to enhance the resolution is to implement the immersion concept and use a high refractive index liquid medium in the path of laser beam near to the photoresist layer. In the case, the period of two-beam interference is expressed as [109]

$$P = \frac{\lambda}{n \cdot 2\sin\theta}, \tag{7.1}$$

where n refers to the refractive index of surrounding medium. In order to increase the numerical aperture ($n\sin\theta$), deep ultraviolet (DUV) light source was employed considerably on a basis of prism or other optical components. Transmission in a high refractive index medium has the advantage of enhancement of the resolution as the effective wavelength is shorter than the vacuum wavelength. For example, the index of refraction of sapphire is ≈1.92, a 193nm wavelength leads to an effective wavelength of ≈100nm in a prism of sapphire. It is the same with the immersion medium. However, it must be pointed out that at present the high-index immersion fluids have an extremely high absorption for DUV wavelength.

Boor et al. reported that using the immersion interference lithography with a laser wavelength of 244nm produced the line patterns on the photoresist resulting a period of less than 100nm and a width of 45nm [110]. In their experiment, a triangular Littrow prism with one metal-coated side instead of a Llyod's mirror was used. The method remains the advantages of Lloyd's interferometer and improves the flexibility of periodicity. Bloomstein et al. utilised immersion interference lithography to fabricate linear photoresist

structures with a 22nm half pitch [111]. A DUV laser source of 157nm was employed and the system was complemented by a sapphire coupling prism with index 2.09 and a 30nm thick immersion fluid with an index of 1.82. The schematic of multi-layer system is show in Fig. 7.1. They pointed out that the system required careful control of immersion liquid layers with 30nm thickness by means of spin casting. Additionally, with a detailed analysis of trade-off between fluid indexes, it was found that a highly transparent medium was preferable but at the cost of low index. Therefore, there is always a contradiction between high transparent and high index, which leads to the limitation of the immersion interference lithography.

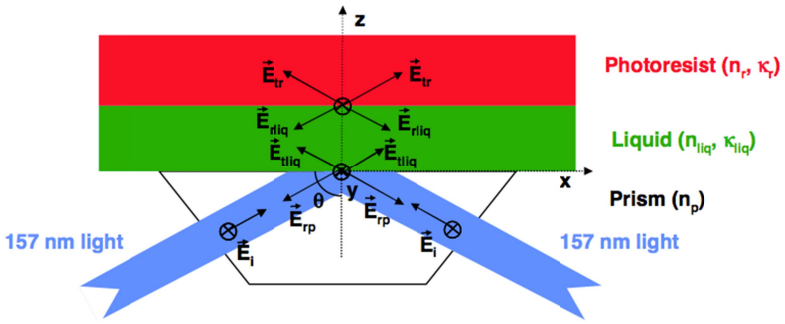

Fig. 7.1 Schematic representation of multi-layer immersion interference system. (Bloomstein et al. 2006)

Thus, an attempt to fabricate high-resolution structures using DLIN is proposed. With the merits of flexible operation and high throughput, DLIN need to be developed further. In the experiments, both organic material and metal thin films were treated by the 266nm nanosecond interference system. Sub-100nm structures on different material surfaces were fabricated. It is found that the interaction between laser and solid materials and thermal effects play a critical role in the quality and resolution of resulting structures and the studying of the mechanism so as to obtain a high-resolution structure. In the next section, the influence factors are described. In addition, as an alternative and complemented method, the combination of LIL and silver deposition was studied for the application of nanoelectrode arrays as well.

7.2 Influence Factors and Limitation of High Resolution

Different from conventional laser processing of materials (e.g. drilling, cutting and welding) with a single beam, novel material fabrication method has been developed based on the laser interference technology which produces various patterns via the superposition of two or multiple laser beams. More and more applications impel laser interference technology towards the high-resolution direction. But there are still a number of influence factors which limit the resolution.

7.2.1 Influence of Contrast

From Eqs. (2.4), (2.5), (2.16) and (2.17), if two beams follow a symmetrical configuration with the same azimuthal and incident angles, the intensity formulas with the polarisation of two-beam laser interference can be written as

$$I_{TE-TE} = A^2\left[2-2\cos(2k\sin\theta\cdot x)\right] \ , \tag{7.2}$$

$$I_{TM-TM} = A^2[2-2\cos 2\theta\cdot\cos(2k\sin\theta\cdot x)] \ . \tag{7.3}$$

Eqs. (7.2) and (7.3) indicate that the periods keep constant regardless of the polarised angles. However, the contrasts have the distinction in two-beam laser interference. Based on Eqs. (7.2), (7.3) and (3.2), the curve can be described as below. From Fig. 7.2 shown, the contrast of the TE-TE polarisation mode is equal to 1.

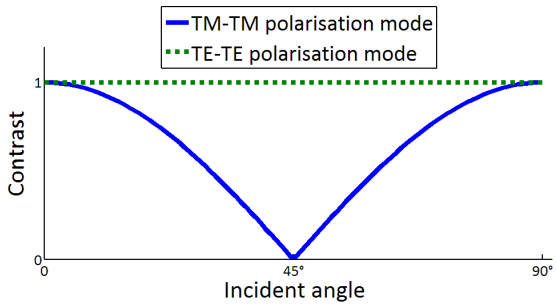

Fig. 7.2 Pattern contrast as a function of incident angle in two-beam laser interference.

It means that the maximum intensities can reach to 1 and the minimum intensities can reach to 0. The contrast of the TM-TM polarisation mode is not maintained when the incident angles change. Once the incident angles of two beams are 45˚, the contrast declines to zero. It means that the interference phenomenon does not occur because the oscillating orientation is perpendicular.

Both direct and indirect (i.e. photoresist) processes, the lower minimum intensity is expected due to the feature shape or called the characteristic dimension has a strong dependence on it. If the photoresist is reacted at the position of minimum intensities, a linear shape at the bottom and walls of structure could not be obtained [11]. As a consequence, the resolution declines.

7.2.2 Influence of Thermal Properties of Materials

The spatial resolution of the features on the material surfaces depends on the combination of fringe periods, contrasts and effects included the physical, chemical and metallurgical properties. Laser fluence (or energy density) along with the thermophysical parameters of materials determines the temperature field distribution.

The thermal simulation is based on the equation of Fourier's heat diffusion [112]:

$$\rho c_p \frac{\partial T}{\partial t} = q_a - q_m - q_v + div(k \cdot grad(T)) \quad , \tag{7.4}$$

where $T = T(x,z,t)$ is the temperature at the position (x, z) at time t; q_a, q_m and q_v are the absorbed heat, the heat of melting, and the heat of vaporisation respectively; ρ, k and c_p are the density, the thermal conductivity and the specific heat of the material respectively. The energy absorbed into material can be expressed by [52]

$$q_a = \alpha \frac{I(x)}{\sigma\sqrt{2\pi}} \exp\left(-\frac{(t-t_p)^2}{2\sigma^2}\right)(1-r)\exp(-\alpha z) \quad , \tag{7.5}$$

$$\sigma = \frac{\tau_p}{2\sqrt{2\ln 2}} \quad , \tag{7.6}$$

where α is the absorption coefficient, $I(x)$ is the interfering intensity distribution, t is the time, t_p is the pulse time, τ_p is the pulse duration, r is the reflectivity of surface. The energy required melting and vaporisation is given by Eqs. (7.7) and (7.8) [52], respectively.

$$q_m = L_m \rho \frac{\partial(0.5 erfc(T - T_m / T_{0m}))}{\partial t} \quad , \tag{7.7}$$

$$q_v = L_v \rho \frac{\partial(0.5 erfc(T - T_b / T_{0b}))}{\partial t} \quad , \tag{7.8}$$

where L_m is the latent heat of fusion, T_m is the melting temperature, T_b is the boiling temperature, L_v is the latent heat of vaporisation, and ρ is the density of solid or liquid. The *erfc* refers to the complementary Error Function.

For a simplified case of one-dimensional conduction without convection and radiation effects, the solution of the heat transfer equation can be re-arranged to estimate the energy required to produce a single fringe of a particular surface feature size. This equation of energy can be expressed as [113]

$$E = \frac{k T_m t_p 10^{-4}}{2\sqrt{\chi} ierfc\left[\frac{z}{2\chi t_p}\right]} \quad , \tag{7.9}$$

where E is energy fluence (J/cm^2), T_m is the melting point (°C), t_p is the pulse time (s), χ is the thermal diffusivity (m^2/s), and z is the surface feature size (m). The *ierfc* refers to the iterated integrals of the complementary error function.

According to the Eqs. (7.4)-(7.8), it can be found that the feature size or called the characteristic dimension must be equal or smaller than the period in order to obtain well-defined structures. Among them, the thermal conductivity is a

significant parameter. For the low conductivity materials, the region of thermal effects is limited into a narrow distance. With the increase of conductivity, the feature size approaches or even overs the period, resulting in the unordered structures. Based on the theoretical analysis of heat transfer, low conductivity materials are possible to achieve higher resolution structures with selection of appropriate laser processing parameters.

7.3 Experimental Aspects

In this session, the 266nm and 1064nm DLIN systems and the 405nm LIL system were employed to achieve high-resolution nanostructures. Each system has its advantage and disadvantage due to its nature of wavelength, power and output manner, which is described as below.

7.3.1 Direct Modification of Organic Material

The overview of the 266nm DLIN system is shown in Fig. 7.3.

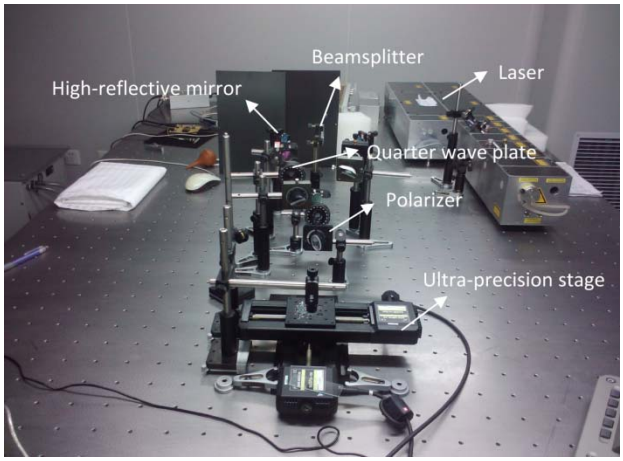

Fig. 7.3 Overview of the experimental setup for 266nm DLIN system.

By using the ultraviolet wavelength, the 266nm DLIN system is a powerful tool for the fabrication of smaller periodic structures. Theoretically, the incident angles can approach to 90˚ and the period will be down to a half of wavelength but in practice the projection profile of light takes place a change of ellipse obviously

when the angles over 60°. Thereby, $\lambda/2$ period of the interference fringe is obtained when two beams are counter-propagating. But for LIL applications, this will be unpractical.

The fundamental laser (1064nm) can be converted into second and third harmonics using harmonic generating assemblies containing KTP and KD*P crystals. The 266nm laser is the third harmonic generation and the max pulse energy at 266nm is 130mJ. In the experiment, the mixture of polyvinyl alcohol and cyclohexanone was chosen as the etched material. First, the organic material was coated by spinning for 30-40s on a polished silicon surface. Second, the hotplate was applied to bake it for 90s at 110˚C.

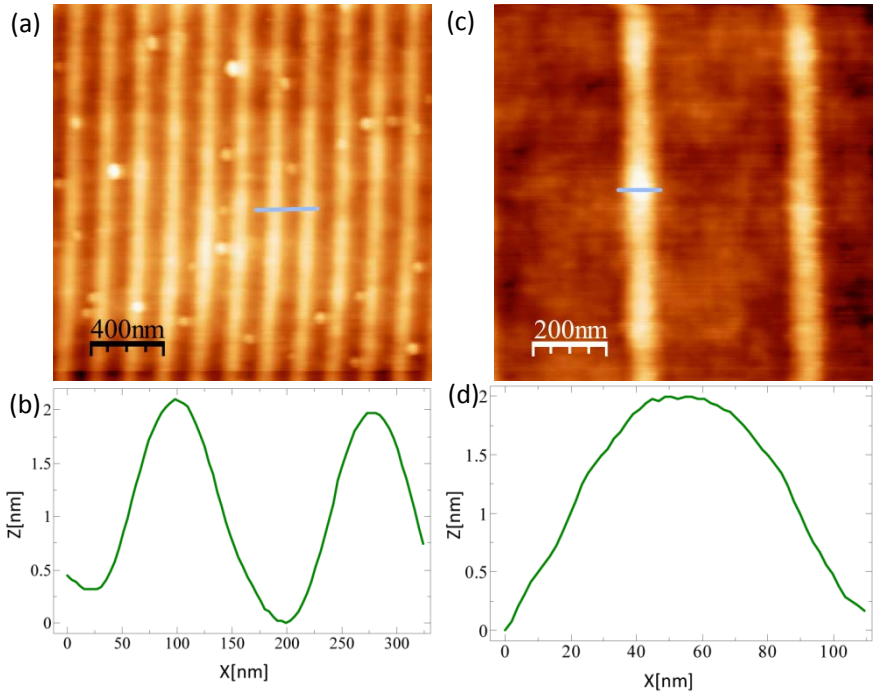

Fig. 7.4 Two periodic grating structures fabricated by 266nm DLIN system. (a) 190nm period fringe; (b) Cross-profile curve along a selected line in (a); (c) 420nm period fringe; (d) Cross-profile curve along a selected line in (c).

From Fig. 7.4 shown, two periodic structures were fabricated corresponding to two incident configurations. The modification threshold of the organic material is lower than those of semiconductor and metals. The used laser fluence was

around 21mJ/cm^2. An AFM was employed to observe the morphology and measure the periods and feature shapes. From Fig. 7.4(b) and (d) shown, the feature size of each grating line is down to 100nm and with regard to the radius of curvature (micro scale) of general AFM tip [114, 115], the real feature shape is estimated to around 50nm. Meanwhile, the height of fringe is only 2nm. Compared with the state of art in laser interference field, it is demonstrated that DLIN has the capability of sub-100nm fabrications and possibly provides a new way for the application of quantum dots, quantum wire and quantum well [4, 116]. Among the degree of 100nm nanofabrication technologies, DLIN takes the advantages of high throughput and low cost.

Based on a high-resolution microscope with image processing capabilities, high relative accuracy of object localization offers useful information in biological engineering, such as cell counting, checking and microinjection. One of challenging problems is to achieve high subpixel accuracy using pattern matching and curve fitting algorithms. Fig. 7.4(a) was selected for the reference pattern. The Image size is 512×512 pixels and scanning area is 2μm×2μm, i.e. one pixel is equal to 3.9nm approximately. Two image patches extracted from Fig. 7.4(a) was analysed with correlation function. The resulting curve is shown in Fig. 7.5.

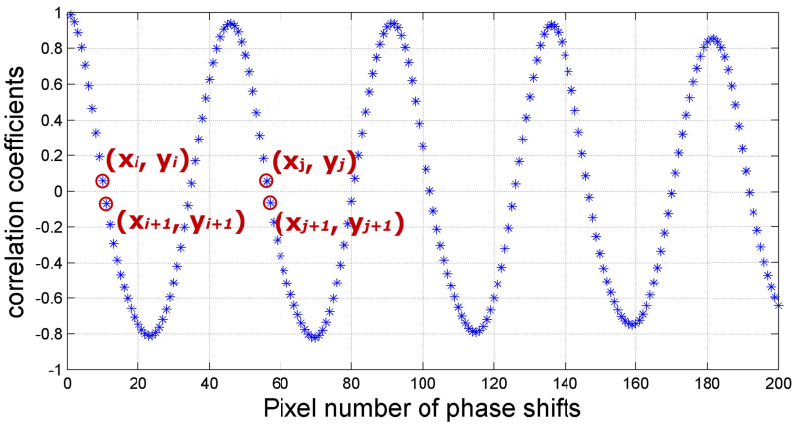

Fig. 7.5 Pattern matching curve of nanograting structures.

To improve the measurement resolution, the polynomial curve fitting method is used and the measured period by polynomial curve fitting is determined as [39]

$$p = x_j - \frac{y_j}{y_{j+1} - y_j} - (x_i - \frac{y_i}{y_{i+1} - y_i}). \tag{7.10}$$

According to Eq. (7.10), the result is 179.7083nm. To evaluate the stability of localization with the method, four group dates from different regions in the Fig. 7.4(a) were analysed, which is shown in Fig. 7.6. The results of four measurements are P_1=46.00532 pixels, P_2=46.04616 pixels, P_3=46.47057 pixels, and P_4=46.11591 pixels, respectively. The standard deviation of four group dates is 0.1893 pixels.

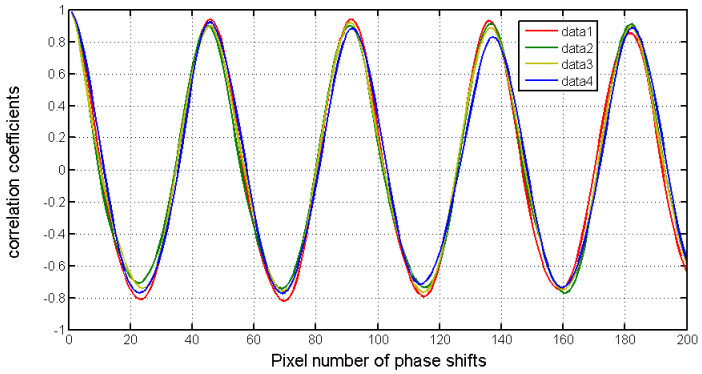

Fig. 7.6 Localization measurement of four different region in the Fig. 7.4(a).

It is demonstrated that the subpixel accuracy of measurements have been realised by correlation function and polynomial curve fitting. The statistical analysis shows that the approach is a very useful tool for intensity-based object localization.

7.3.2 Direct Modification of Metal Thin Films

There are many applications in the structural thin metal films, such as metamaterials [117], surface plasmon polaritons [118], filters for terahertz (THz) radiation [119] and other research and technological fields. Apart from the conventional way of single beam laser writing, FIB and EBL, an alternative scheme, DLIN, has been addressed. Laser-induced periodic surface arrays are useful to control the surface desirable shape. Two-dimensional (2D) and

three-dimensional (3D) structures are produced by using interference of several coherent beams and the method allows patterning of areas over a beam spot size.

In the experiment, the samples of Platinum (Pt) thin film with a thickness of 10nm were deposited on the polished silicon substrate. The 1064nm laser was split into two beams by a beamsplitter and two high-reflection mirrors with the incident angles of 17˚, which results in the period of 1.8μm theoretically. In the case of thin films, different topographical regimes were observed depending on the laser fluence. All the samples were treated by the nanosecond laser with a single shot. For a relative low range of laser fluence, a small quantity of molten materials where are the maximum intensities of interference can be seen in Fig. 7.7(a). As the laser fluence increases, the molten region goes larger from the maximum intensities toward the neighbour minimum intensities. In this condition, the surface temperature is raised to the melting point and results in a number of nanoparticles (shown in Fig. 7.7(b)). With the further increase of laser fluence, the Pt thin film is removed and shows a bump silicon structure at the maximum intensities. From Fig. 7.7(c) and (d) shown, the process of laser ablation is completed.

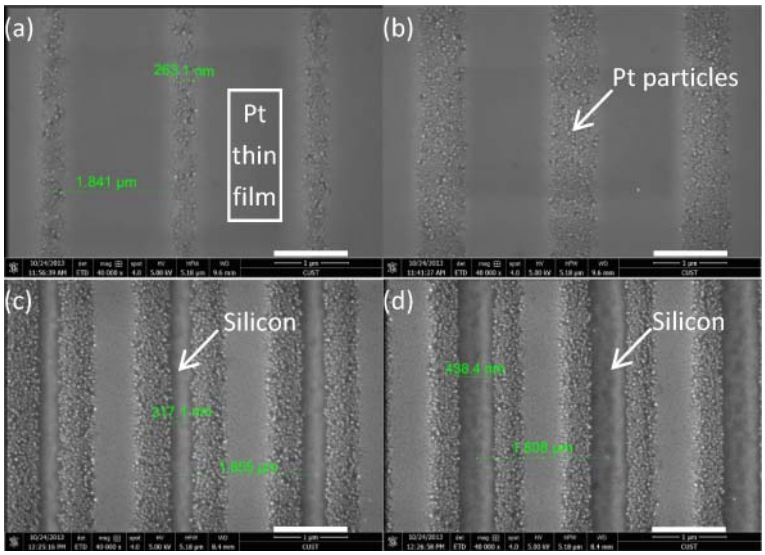

Fig. 7.7 SEM images of metal thin film treated by the two-beam laser interference system. (a)

laser fluence=250mJ/cm^2; (b) laser fluence=350mJ/cm^2; (c) laser fluence=450mJ/cm^2; (d) laser fluence=520mJ/cm^2; All the scale bars are 1μm.

It is demonstrated that the damage threshold depends on the natural properties of materials. In addition, the defined values of threshold are related to the absorption coefficient, reflectance, incident angles, laser wavelength and generation of defects. For thin films, the threshold is also dependent on the film thickness and substrate materials. Nonetheless, DLIN is a promising attempt to achieve high-resolution fabrication. It is typically of interest to study the limited resolution of various materials with different wavelengths.

7.3.3 Silverwire Arrays achieved by 405nm LIL System

In this session, a complemented method of LIL and chemical deposition is proposed to fabricate the nanosilver arrays. In the LIL system, a semiconductor laser with a wavelength of 405nm and an output power of 80mW was used as the coherent source. The flow chart of the manufacturing processes is shown in Fig. 7.8. The negative photoresist of NR9G-500P (Futurrex, Inc.) was used in the experiment. It is sensitive to exposure wavelengths shorter than 440nm. The detailed procedures can be concluded as below:

I. NR9G-500P resist is dispensed by spin coating at 3000 rpm for 40s. Acceleration from 0 to 3000 rpm is conducted in less than 1s.

II. Softbake on a hotplate at 110˚C for 60s.

III. Substrate cooling to room temperature.

IV. Exposure energy for 0.5μm thick film of NR9G-500P on silicon is around 8mJ/cm^2 for 1-2s.

V. Post-exposure bake on a hotplate at 110˚C for 60s.

VI. Substrate cooling to room temperature.

VII. Resist is developed by immersion and agitation at 20-25˚C. Development time for 0.5μm thick film is 3-5s.

VIII. Resist rinse in fast flowing stream of deionized water until water resistivity reaches prescribed limit.

IX. Drying resist.

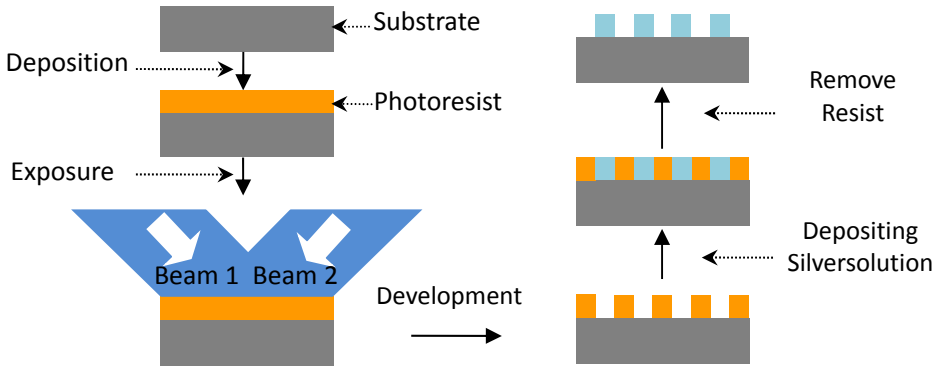

Fig. 7.8 The flow chart of the manufacturing processes.

The process described as above is similar to the traditional LIL process. Compared with previous publications, a spatial filtering and beam expansion system was setup in order to improve the quality of beam profile and uniform distribution of interfering beams. Generally, semiconductor lasers take the disadvantage of poor beam quality. It is a troublesome issue for many nanostructure-based applications achieved by LIL. Lasers used for LIL exposures usually produce an approximate Gaussian intensity profile. Therefore, a non-uniform Gaussian beam results in a non-uniformity distribution of resulting structures. In order to solve the problem, a spatial filtering and beam expansion system is presented, which is shown in Fig. 7.9. It is similar to the Kaplerian telescope system. Two positive focused lenses and a pinhole compose the system. Two focused lenses have different focal lengths. Generally, the focal length of f_2 is larger than that of f_1. In the experiment, the f_1=35mm and f_2=100mm lenses are chosen. The expansion ratio is 2.85 times. The input Gaussian beam has various intensity “noises” spatially, especially focused by an aspheric lens. That will produce a central

Gaussian spot on the optical axis and side diffractive fringes. By putting a pinhole in a central Gaussian spot, the unwanted “noises” will be blocked. A diameter of 25μm pinhole was chosen in the experiment.

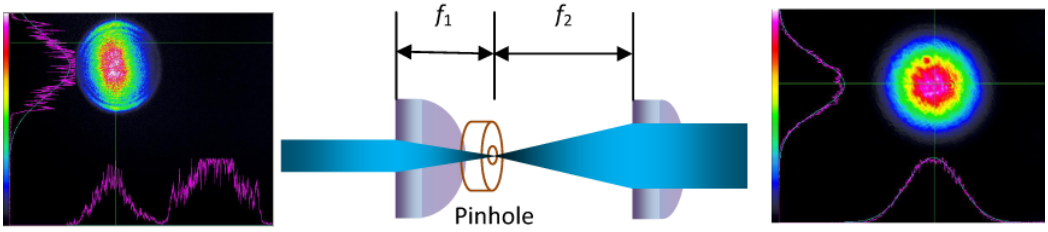

Fig. 7.9 Schematic description of spatial filtering and beam expansion system. Left: the beam quality of initial laser from 405nm semiconductor laser; Middle: principle for spatial filtering and beam expansion system; Right: the beam quality after the spatial filtering and beam expansion system.

The measurement instrument used in the experiment is the high-resolution SWIR laser beam profiling system (LaserCam-HR, Coherent Inc.) to characterise the beam quality. The compared parameters of beam quality are concluded in the Table 4.

Table 4 Compared parameters of beam quality between initial laser and improved laser.

Name	Initial laser	Improved laser
Effective Diameter 86.5% [mm]	2.671	3.190
Ellipticity Major, Minor 86.5% [mm]	3.084, 2.533	3.284, 3.144
Circularity Coefficient	0.821	0.957
Gaussian Coefficient in x axis	0.0	0.950
Gaussian Coefficient in y axis	0.813	0.932

From Fig. 7.9 and Table 4 suggested, the beam quality has been improved by the spatial filtering and beam expansion system. The beam quality will influence the micro and nano structures on the photoresist obviously. In the exposure experiment, the fabricated structures are sensitive to the laser power and exposure time (ET). The laser power can be adjusted by the combination of wave plates and polariser, and the ET is pre-set by a precision electronic shutter

positioned the exit of laser. The optimal energy does suggested in the instruction of photoresist company is useful to carry out the well-defined structures. But it is worth pointing out that the parameters of most photoresists are suitable to the IC industry that commonly employs optical lithography technique. That is quite different due to a discrepancy between the Gaussian beam and the collimated beam.

From Fig. 7.10 shown, the topographies of grating structures on photoresist have a significant difference with each other. The left image represents the result without the spatial filtering and beam expansion system. There are a number of adhesive and non-uniform regions. The right one represents the result fabricated by two-beam interference method with the spatial filtering and beam expansion system. From Fig. 7.10 shown, it is demonstrated that the feature shape and profile of structures can be improved by the spatial filtering and beam expansion system. That will be constructive to achieve the well-defined structures in the next procedures.

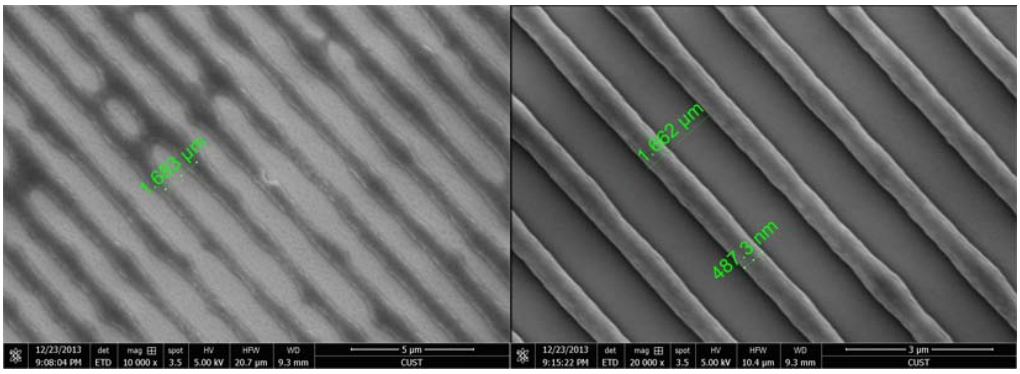

Fig. 7.10 Topographies of grating structures on the photoresist. Left: without the spatial filtering and beam expansion system; Right: with the spatial filtering and beam expansion system.

The silver solution was prepared in our laboratory and the preparation involves three steps. First a few drops of dilute sodium hydroxide are added to some aqueous silver nitrate. The OH^- ions from the sodium hydroxide react with the Ag^+ ions to give silver oxide, which is insoluble and shown as a brown solid. The reaction is well-known and expressed as

$$2Ag^{+} + 2OH^{-} \rightarrow Ag_2O\downarrow + H_2O. \quad (7.11)$$

In the next step, aqueous ammonia is added until all of the brown silver oxide is dissolved. The reaction is expressed as

$$Ag_2O + 4NH_3 + H_2O \rightarrow 2[Ag(NH_3)_2]^{+} + 2OH^{-}. \quad (7.12)$$

The third step is to put a small amount of glucose. It has an aldehyde (RCHO) group that easily undergoes oxidation even with weak oxidizing agents. The reaction is expressed as

$$RCHO + 2[Ag(NH_3)_2]^{+} + 2OH^{-} \rightarrow RCOOH + 2Ag\downarrow + 4NH_3 + H_2O. \quad (7.13)$$

After the deposition with an amount of solution, the solidification process needs a hot plate to heat the sample for several seconds. And then the photoresist layer was removed by RR41 (Futurrex, Inc.). The sample was rinsed under the deionized water and dried by nitrogen gas. From Fig. 7.11 shown, an array of nano silverwires was fabricated.

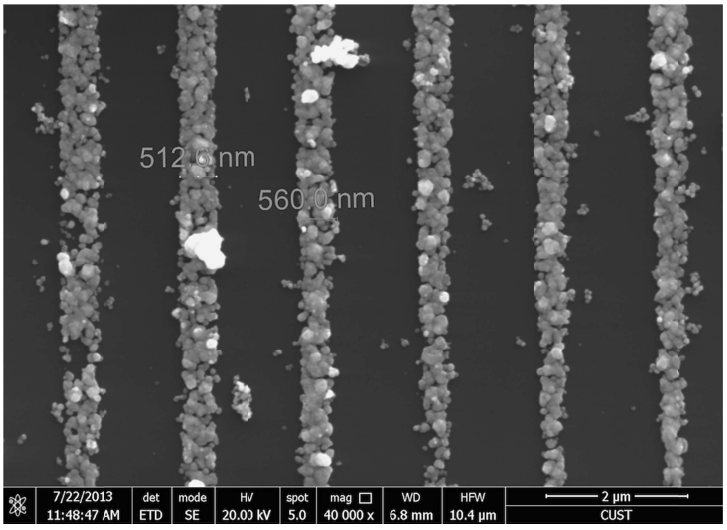

Fig. 7.11 SEM image of array of nano silverwires.

For the defects of nanowires, they can be improved with further fabrication optimizations. The current non-uniformity of the whole array could be due to the

concentration of silver solution and precise control of reaction temperature. In addition, the annealing process should be taken into account of the nanoelectrode detection.

In the experiment, it was found that the diameter of Ag particles forming into silverwires is dependent on the heating temperature of substrate. The smaller diameter of particles was obtained at a relative higher temperature. From Fig. 7.12 shown, the particles were generated when the heating temperature was approximately 70°C and the range of feature sizes of particles is from 20nm to 120nm.

As silver nanoparticles are well-known to perform higher light absorption efficiency then gold nanoparticles in the range of ultraviolet spectrum [105], the results from the work will provide a useful alternative for fabricating plasmonic layers, as well as, a range of other solar cells.

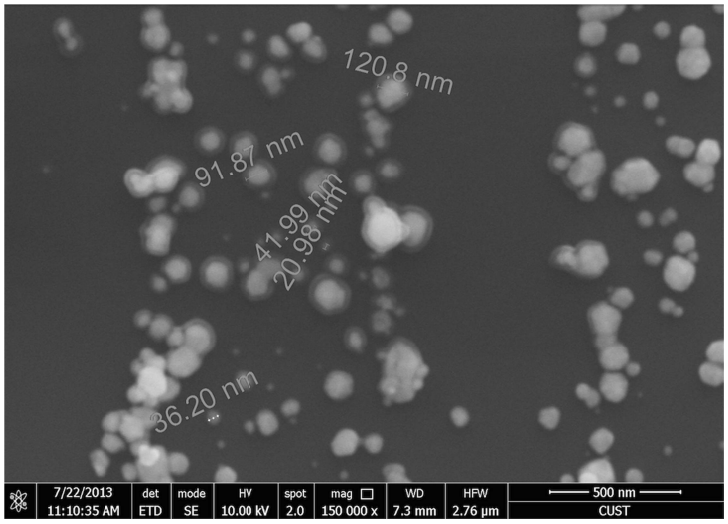

Fig. 7.12 SEM image of the feature sizes of Ag particles.

Whatever the platinum nanoparticles fabricated by DLIN or the silver nanoparticles achieved by the 405nm LIL system offer a new method of enhancing the localized surface plasmon resonance when the particle size decreases down to nano scale. These metal structures can be applied to biosensing, optical antennas, plasmonic waveguide, and surface enhanced

Raman scattering.

7.4 Summary

In this chapter, approaches to fabricate the high-resolution structures are proposed. A 266nm nanosecond laser interference system was set up and treated to difference materials. During the ablation process of organic material, grating arrays with a period of approximate 200nm and feature sizes of sub-100nm were fabricated. For the metal thin films, the feature sizes of well-defined structures were around 200nm. With increase of laser fluences, different topographies of samples were observed. A large number of nanoparticles took place at the maximum intensities. Compared with two materials treated by 266nm laser interference system, it can be seen that the ablation mechanisms of metal and non-metal materials are totally different. The thermal properties and parameters of materials play a key role in the formation of resulting structures. As an alternative, the complemented method of LIL with a 405nm semiconductor laser and chemical deposition was studied as well. It has been demonstrated that the spatial filtering and beam expansion system has an advantage of improving the quality of beam profile. The range of feature sizes of particles is from 20nm to 120nm. The proposed method is suitable for non-planar fabrication of nanoelectrode arrays.

DLIN has been demonstrated to be an extremely flexible and versatile tool for the fulfilment of wide-ranging applications. The fabricating periods are scalable from micrometre to nanometre to accommodate varying the incident angles or wavelengths, which can be verified from the results in chapters 6 and 7 respectively. Moreover, DLIN has a highly adaptable to the treated materials as well. Compared to quantities of previous studies concerning the indirect method, i.e. LIL, the work presented in the thesis can contribute to the high efficiency and throughput strategy in a straightforward manner. Importantly, the theoretical analyses on a basis of the methodology described in section 2.4 play a vital role in achieving the significant outcomes for the explanation of modulation in

chapter 5, the deigned scheme of functional structures in chapter 6 and the optimum contrast of high-resolution structures in chapter 7 all benefit from the detailed theoretical analyses.

Chapter 8

Conclusions

8.1 Summary of Thesis

The work presented in the thesis concerns laser interference and direct laser interference technologies from both theoretical and experimental perspectives. Chapter 1 provides a basic overview of current micro and nano fabrication technologies and describes both advantages and limitations of each technology respectively. Among them, LIL is regarded as a powerful tool for the fabrication of periodic and quasi-periodic structures. With the deep investigation of LIL, it is found that using direct modification of materials on a basis of nanosecond laser interference system technique makes up the insufficiency of LIL and takes the advantages of high efficiency and low cost. For the motivation of developing LIL towards high resolution and large area, the aim and objectives are determined. Chapter 2 reviews the fundamental theories of classical interference, anti-reflection and self-cleaning. Since the effects of polarisation vector on the formation, period and contrast of interference patterns are demonstrated by a number of experimental observations. The combination of polarisation vector and electric field vector is incorporated into the methodology of the thesis. The theoretical analyses based on the methodology are implemented throughout the experiment research.

In chapter 3, the He-Ne laser interference imaging system is introduced. It takes the advantage of real-time imaging and can contribute to visual feedback on micro and nano scales. Meanwhile, it offers an effective way to investigate the multi-beam laser interference patterns, especially 3D patterns and analyse the beam incidence conditions due to the challenges from a book-keeping perspective. In the experiment, the interference patterns were captured by a CCD camera under different incidence conditions, the measurement of the

pattern periods was achieved by the cross-correlation function, and the pattern contrasts were calculated by image processing. Subsequently, the incident angles and intensities of beams were determined based on the analysis of spatial distributions of interfering beams. As a consequence, the relationship between the beam incidence conditions and interference patterns is revealed. The proposed method is useful for the calibration of LIL processes and for reverse engineering applications.

In the chapter 4, by taking the strategy of direct nanosecond laser interference technology, and the silicon material is selected to create different well-defined surface structures based on theoretical analysis of the formation of laser interference patterns. Two, three and four-beam laser interference systems were set up to fabricate the grating, regular triangle and square structures on silicon surfaces, respectively. From the AFM micrographs, the critical features of structures have a dependence on laser fluences. For a relative low laser fluence, the grating and dot structures formed with bumps due to the Marangoni Effect. With the increase of laser fluences, melt and evaporation behaviours can be responsible for the laser modification. It can be demonstrated that well-defined grating and dot structures can be achieved by properly selecting the process parameters.

Chapter 5 gives a comprehensive study for the effects of polarisation vector on the interference patterns. Described in a number of literatures, the modulation phenomenon was regarded as a hardly avoided affair in four-beam laser interference. But, the theoretical equations according to different polarisation modes are derivate and corresponding analyses demonstrate that the modulation is the result of the misaligned or unequal incident angles only in the case of the TE-TE-TM-TM mode. With respect to TE-TE-TE-TE and TE-TE-TE-TM polarisation modes, they can be utilised to fabricate micro and nano cone and hole structures respectively. Actually, the conclusion obtained in the work is constructive to achieve the anti-reflection and superhydrophobicity applications

in chapter 6. The experimental results have shown a good correspondence with the theoretical analysis and simulations.

In chapters 6 and 7, the work is focused on the high resolution and large area applications. Inspired by nature, a number of techniques have been developed to fabricate the bionic structures of lotus leaves and Moth-eye which enable to realise the extraordinary functions of self-cleaning and antireflection. The straightforward method, DLIN, of fabricating well-defined micro and nano artificial bio-structures is proposed in this work. Both antireflection and superhydrophobicity behaviours exhibited by microcone structures were observed. It is found that the reflection behaviour is dependent on the structural depth, and the deeper structures were achieved for the larger periods. Compared with the one-dimension microstructures, the hierarchical nanostructures have ability of reducing the solid-liquid contact area and increasing the CAs. Consequently, the microcone structures exhibited excellent properties with both a high contact angle (CA=156.3°) and low omnidirectional reflectance (5.9-15.4%). In order to fabricate high-resolution structures, the 266nm nanosecond laser interference system is employed to treat the organic and metal-film materials. It can be seen that the thermal effects play a key role in the direct ablation process. Sub-100nm width and 2nm height of grating structures with a pitch of approximate 200nm was fabricated on the organic material surface, while quantities of molten materials where are the maximum intensities of interference can be observed on the metal thin films. That is related to the threshold of modification and the melting point of materials. Subsequently, another attempt to produce the nanoelectrode arrays by means of LIL and chemical deposition is put forward as well. In addition, the quality of beam was improved obviously by a 4*f* system. The method has an advantage of non-planar fabrication.

Chapter 8 finally summarises the work of the thesis and lays out the novel results and contributions achieved in the research. Recommendations of future work are

given as well.

8.2 Future Work

The work presented in the thesis has attained a number of significant achievements in the field of DLIN, but there are also other issues and potential tasks benefited from this work.

Although DLIN is a promising technology for the fabrication of periodic structures with high throughput and low cost, there are still intractable problems for DLIN. The interaction between short-pulse laser and matter on the nano scale is not well established. Once the radius of thermal region affected by short-pulse laser overs the period of interference, as a result, the processes of energy transfer, heat conduction and hydrodynamic expansion are complex and unpredictable. In this case, laser-matter interaction will bring about a huge number of interesting phenomena that need to be explored. The limited resolution or feature sizes for various materials treated by different wavelengths from infrared to ultraviolet should be investigated further.

Besides, DLIN is expected to make more aggressive advances in the potential applications. Recently, organic light-emitting diodes (OLEDs) have attracted considerable attention for their potential in next-generation mobile electronics and illuminations. However, the low out-coupling efficiency (20%-30%) that is attributed to waveguide effect at the interfaces limits their practical application. In 2014, Jeon et al. demonstrated that 2D nanohole arrays embedded between cathode and organic layers enhance the efficiency by a factor of 2.16 [120]. They used the reverse transfer (R^2T) technology to fabricate the period of 530nm structure. Compared with R^2T, DLIN is more flexible due to maskless. It is the same with multi-quantum-well solar cells with nanostructures. In 2014, Bai et al. investigated nanorod and nanohole structures inserted into InGaN/GaN solar cells by means of nanosphere lithography [121]. It was found that a larger enhancement is observed for the nanohole array, where the conversion efficiency

is enhanced by 51%.

Moreover, optical metamaterials (MMs) offers unprecedented functionalities of controlling the flow of light [122]. Surface plasmon polaritons (SPPs) has the advantages of tight spatial confinement, high local field intensity [123]. All of them show a dependence on nanostructures. For these reasons, DLIN has an excited potential for nano-optics, bio-photonics and so on.

References

[1] G. Li, M. Kang, S. Chen, S. Zhang, E. Y. B. Pun, K. W. Cheah, and J. Li, "Spin-Enabled Plasmonic Metasurfaces for Manipulating Orbital Angular Momentum of Light", *Nano letters,* 13 (2013), 4148-4151.

[2] Y. Liu, and X. Zhang, "Metasurfaces for Manipulating Surface Plasmons", *Applied Physics Letters,* 103 (2013), 141101.

[3] L. Huang, X. Chen, B. Bai, Q. Tan, G. Jin, T. Zentgraf, and S. Zhang, "Helicity Dependent Directional Surface Plasmon Polariton Excitation Using a Metasurface with Interfacial Phase Discontinuity", *Light: Science & Applications,* 2 (2013), 70.

[4] L. Y. Pan, Y. L. Zhang, H. Y. Wang, H. Liu, J. S. Luo, H. Xia, L. Zhao, Q. D. Chen, S. P. Xu, B. R. Gao, L. M. Fu, and H. B. Sun, "Hierarchical Self-Assembly of Cdte Quantum Dots into Hyperbranched Nanobundles: Suppression of Biexciton Auger Recombination", *Nanoscale,* 3 (2011), 2882-2888.

[5] V. Zorba, E. Stratakis, M. Barberoglou, E. Spanakis, P. Tzanetakis, S. H. Anastasiadis, and C. Fotakis, "Biomimetic Artificial Surfaces Quantitatively Reproduce the Water Repellency of a Lotus Leaf", *Advanced Materials,* 20 (2008), 4049-4054.

[6] L. Zhang, W. F. Dong, and H. B. Sun, "Multifunctional Superparamagnetic Iron Oxide Nanoparticles: Design, Synthesis and Biomedical Photonic Applications", *Nanoscale,* 5 (2013), 7664-7684.

[7] S. R. J. Brueck, "Optical and Interferometric Lithography-Nanotechnology Enablers", *Proceedings of the IEEE,* 93 (2005), 1704-1721.

[8] M. Zheng, M. Yu, Y. Liu, R. Skomski, S. H. Liou, D. J. Sellmyer, V. N. Petryakov, Y. K. Verevkin, N. I. Polushkin, and N. N. Salashchenko, "Magnetic Nanodot Arrays Produced by Direct Laser Interference Lithography", *Applied Physics Letters,* 79 (2001), 2606-2608.

[9] J. W. Menezes, J. Ferreira, M. J. L. Santos, L. Cescato, and A. G. Brolo, "Large-Area Fabrication of Periodic Arrays of Nanoholes in Metal Films and Their Application in Biosensing and Plasmonic-Enhanced Photovoltaics", *Advanced Functional Materials,* 20 (2010), 3918-3924.

[10] J. Xu, Z. Wang, Z. Zhang, D. Wang, and Z. Weng, "Fabrication of Moth-Eye Structures on Silicon by Direct Six-Beam Laser Interference Lithography", *Journal of Applied Physics,* 115 (2014), 203101.

[11] M. Ellman, A. Rodríguez, N. Pérez, M. Echeverria, Y. K. Verevkin, C. S. Peng, T. Berthou, Z. Wang, S. M. Olaizola, and I. Ayerdi, "High-Power Laser Interference Lithography Process on Photoresist: Effect of Laser Fluence and Polarisation", *Applied Surface Science,* 255 (2009), 5537-5541.

[12] P. Y. Baroni, B. Paivanranta, T. Scharf, W. Nakagawa, M. Roussey, M. Kuittinen, and H. P.

Herzig, "Nanostructured Surface Fabricated by Laser Interference Lithography to Attenuate the Reflectivity of Microlens Arrays", *Journal of the European Optical Society: Rapid Publications,* 5 (2010), 10006.

[13] Y. Yang, C. Hsu, T. Chang, L. Kuo, and P. Chen, "Study on Wetting Properties of Periodical Nanopatterns by a Combinative Technique of Photolithography and Laser Interference Lithography", *Applied Surface Science,* 256 (2010), 3683-3687.

[14] N. Pérez, T. Tavera, A. Rodríguez, M. Ellman, I. Ayerdi, and S. M. Olaizola, "Fabrication of Sub-Micrometric Metallic Hollow-Core Structures by Laser Interference Lithography", *Applied Surface Science,* 258 (2012), 9370-9373.

[15] J. H. Seo, J. Park, D. Zhao, H. Yang, W. Zhou, B.-K. Ju, and Z. Ma, "Large-Area Printed Broadband Membrane Reflectors by Laser Interference Lithography", *Photonics Journal, IEEE,* 5 (2013), 2200106.

[16] S. Bagheri, H. Giessen, and F. Neubrech, "Large-Area Antenna-Assisted Seira Substrates by Laser Interference Lithography", *Advanced Optical Materials* (2014), published online.

[17] R. Adato, and H. Altug, "In-Situ Ultra-Sensitive Infrared Absorption Spectroscopy of Biomolecule Interactions in Real Time with Plasmonic Nanoantennas", *Nature Communications,* 4 (2013), 2154.

[18] J. C. Maxwell, *A Dynamical Theory of the Electromagnetic Field*. Vol. 155, *Philosophical Transactions of the Royal Society of London* (1865), pp. 459-512.

[19] M. Born, and E. Wolf, *Principles of Optics: Electromagnetic Theory of Propagation, Interference and Diffraction of Light* (CUP Archive, 1999).

[20] H. Kikuta, Y. Ohira, H. Kubo, and K. Iwata, "Effective Medium Theory of Two-Dimensional Subwavelength Gratings in the Non-Quasi-Static Limit", *Journal of the Optical Society of America A,* 15 (1998), 1577-1585.

[21] Z. Wang, J. Zhang, L. Hang, S. Jiang, G. Liu, Z. Ji, C. Tan, and H. Sun, "Nanoscale Structures for Implementation of Anti-Reflection and Self-Cleaning Functions", *International Journal of Nanomanufacturing,* 9 (2013), 520-531.

[22] J. Yao, A. P. Le, S. K. Gray, J. S. Moore, J. A. Rogers, and R. G. Nuzzo, "Nanostructured Plasmonic Materials: Functional Nanostructured Plasmonic Materials (Adv. Mater. 10/2010)", *Advanced Materials,* 22 (2010), 1102-1110.

[23] C. H. Chou, and F. C. Chen, "Plasmonic Nanostructures for Light Trapping in Organic Photovoltaic Devices", *Nanoscale,* 6 (2014), 8444-8458.

[24] S. Varlamov, Z. Ouyang, X. Zhao, and D. S. Jung, "Surface Plasmon Enhanced Light-Trapping in Polycrystalline Silicon Thin-Film Solar", *Photonics Global Conference (PGC)*, pp (1-6), 2010.

[25] W. Barthlott, and C. Neinhuis, "Purity of the Sacred Lotus, or Escape from Contamination in Biological Surfaces", *Planta,* 202 (1997), 1-8.

[26] C. Neinhuis, and W. Barthlott, "Characterization and Distribution of Water-Repellent,

Self-Cleaning Plant Surfaces", *Annals of Botany,* 79 (1997), 667-677.

[27] W. L. Min, B. Jiang, and P. Jiang, "Bioinspired Self-Cleaning Antireflection Coatings", *Advanced Materials,* 20 (2008), 3914-3918.

[28] D. Wu, S. Z. Wu, Q. D. Chen, S. Zhao, H. Zhang, J. Jiao, J. A. Piersol, J. N. Wang, H. B. Sun, and L. Jiang, "Facile Creation of Hierarchical Pdms Microstructures with Extreme Underwater Superoleophobicity for Anti-Oil Application in Microfluidic Channels", *Lab on a Chip,* 11 (2011), 3873-3879.

[29] D. Wu, Q. D. Chen, J. Yao, Y. C. Guan, J. N. Wang, L. G. Niu, H. H. Fang, and H. B. Sun, "A Simple Strategy to Realize Biomimetic Surfaces with Controlled Anisotropic Wetting", *Applied Physics Letters,* 96 (2010), 053704.

[30] N. D. Wanasekara, and V. B. Chalivendra, "Role of Surface Roughness on Wettability and Coefficient of Restitution in Butterfly Wings", *Soft Matter,* 7 (2011), 373–379.

[31] T. Young, "An Essay on the Cohesion of Fluids", *Philosophical Transactions of the Royal Society of London* (1805), 65-87.

[32] R. N. Wenzel, "Resistance of Solid Surfaces to Wetting by Water", *Industrial & Engineering Chemistry,* 28 (1936), 988-994.

[33] A. Cassie, and S. Baxter, "Wettability of Porous Surfaces", *Transactions of the Faraday Society,* 40 (1944), 546-551.

[34] B. Bhushan, Y. C. Jung, and K. Koch, "Micro-, Nano- and Hierarchical Structures for Superhydrophobicity, Self-Cleaning and Low Adhesion", *Philosophical Transactions of the Royal Society A: Mathematical, Physical and Engineering Sciences,* 367 (2009), 1631-1672.

[35] W. Li, Z. Wang, D. Wang, Z. Zhang, L. Zhao, D. Li, R. Qiu, and C. Maple, "Superhydrophobic Dual Micro-and Nanostructures Fabricated by Direct Laser Interference Lithography", *Optical Engineering,* 53 (2014), 034109-034109.

[36] D. Wang, Z. Wang, Z. Zhang, Y. Yue, D. Li, and C. Maple, "Modification of Silicon Surface by Direct Laser Interference", *International Conference on Manipulation, Manufacturing and Measurement on the Nanoscale (3M-NANO)*, pp (5-8), 2012.

[37] Z. Wang, P. J. Bryanston-Cross, and H. Long, "Displacement Measurement Based on Young's Experiment", *Proceedings of SPIE*, pp (786-793), 1996.

[38] J. Ze, Z. Jin, P. Changsi, T. Chunlei, S. M. Olaizola, T. Berthou, S. Tisserand, Y. K. Verevkin, and W. Zuobin, "Quality Inspection of Nanoscale Patterns Produced by Laser Interference Lithography Using Image Analysis Techniques", *International Conference on Mechatronics and Automation, ICMA*, pp (1835-1840), 2009.

[39] L. Liu, H. Xu, Z. Song, R. Liu, J. Zhang, and Z. Wang, "Phase Difference Determination by Fringe Pattern Correlation", *International Conference on Mechatronics and Automation, ICMA*, pp (4868-4873), 2009.

[40] L. Liu, H. Pan, J. Xu, H. Xu, Y. Yue, D. Li, Z. Song, Z. Weng, Z. Hu, Z. Wang, and J. Zhang,

"Oblique Fringe Measurement by Pattern Correlation", *IEEE International Conference on Information and Automation (ICIA)*, pp (940-945), 2010.

[41] C. S. Lim, M. H. Hong, Y. Lin, Q. Xie, B. S. Luk'yanchuk, A. Senthil Kumar, and M. Rahman, "Microlens Array Fabrication by Laser Interference Lithography for Super-Resolution Surface Nanopatterning", *Applied Physics Letters,* 89 (2006), 1911251-1911253.

[42] J. Škriniarová, N. Tarjányi, M. Veselý, and I. Turek, "Periodic Structures Prepared by Two-Beam Interference Method", *Microelectronics Journal,* 38 (2007), 746-749.

[43] J. L. Stay, and T. K. Gaylord, "Three-Beam-Interference Lithography: Contrast and Crystallography", *Applied optics,* 47 (2008), 3221-3230.

[44] Y. Zhang, Y. Chen, L. Shi, J. Li, and Z. Guo, "Recent Progress of Double-Structural and Functional Materials with Special Wettability", *Journal of Materials Chemistry,* 22 (2012), 799-815.

[45] S. Wong, M. Deubel, F. Pérez-Willard, S. John, G. A. Ozin, M. Wegener, and G. von Freymann, "Direct Laser Writing of Three-Dimensional Photonic Crystals with a Complete Photonic Bandgap in Chalcogenide Glasses", *Advanced materials,* 18 (2006), 265-269.

[46] M. Stroisch, T. Woggon, U. Lemmer, G. Bastian, G. Violakis, and S. Pissadakis, "Organic Semiconductor Distributed Feedback Laser Fabricated by Direct Laser Interference Ablation", *Optics Express,* 15 (2007), 3968-3968.

[47] B. Voisiat, M. Gedvilas, S. Indrišiūnas, and G. Račiukaitis, "Picosecond-Laser 4-Beam-Interference Ablation as a Flexible Tool for Thin Film Microstructuring", *Physics Procedia,* 12 (2011), 116-124.

[48] T. Kondo, S. Matsuo, S. Juodkazis, and H. Misawa, "Femtosecond Laser Interference Technique with Diffractive Beam Splitter for Fabrication of Three-Dimensional Photonic Crystals", *Applied Physics Letters,* 79 (2001), 725-727.

[49] M. R. S. Castro, A. F. Lasagni, H. K. Schmidt, and F. Mücklich, "Direct Laser Interference Patterning of Multi-Walled Carbon Nanotube-Based Transparent Conductive Coatings", *Applied Surface Science,* 254 (2008), 5874-5878.

[50] A. Lasagni, F. Mücklich, M. R. Nejati, and R. Clasen, "Periodical Surface Structuring of Metals by Laser Interference Metallurgy as a New Fabrication Method of Textured Solar Selective Absorbers", *Advanced Engineering Materials,* 8 (2006), 580-584.

[51] M. D'Alessandria, A. Lasagni, and F. Mücklich, "Direct Micro-Patterning of Aluminum Substrates Via Laser Interference Metallurgy", *Applied Surface Science,* 255 (2008), 3210-3216.

[52] A. Lasagni, and F. Mücklich, "Fem Simulation of Periodical Local Heating Caused by Laser Interference Metallurgy", *Journal of Materials Processing Technology,* 209 (2009), 202-209.

[53] T. Roch, V. Weihnacht, H. J. Scheibe, A. Roch, and A. F. Lasagni, "Direct Laser Interference Patterning of Tetrahedral Amorphous Carbon Films for Tribological Applications", *Diamond and Related Materials,* 33 (2013), 20-26.

[54] J. Kim, M. H. Ji, D. Yuan, R. Guo, J. Liu, M. Asadirad, T. Detchprohm, M.-K. Kwon, R. D. Dupuis, and S. Das, "Direct Periodic Patterning of Gan-Based Light-Emitting Diodes by Three-Beam Interference Laser Ablation", *Applied Physics Letters,* 104 (2014), 141105.

[55] J. H. Kim, J. Y. Cho, J. Park, B. K. Lee, K. H. Baek, H. Lee, and L. M. Do, "Improvement of Light out-Coupling Efficiency in Organic Light-Emitting Diodes with Variable Nanopatterns", *Electronic Materials Letters,* 10 (2014), 27-29.

[56] T. Tavera, N. Pérez, and A. Rodríguez, "Periodic Patterning of Silicon by Direct Nanosecond Laser Interference Ablation", *Applied Surface Science,* 258 (2011), 1175-1180.

[57] M. A. Green, and M. J. Keevers, "Optical Properties of Intrinsic Silicon at 300 K", *Progress in Photovoltaics: Research and Applications,* 3 (1995), 189-192.

[58] L. T. Lee, S. Ito, H. Benten, H. Ohkita, and D. Mori, "Current Mode Atomic Force Microscopy (C-Afm) Study for Local Electrical Characterization of Conjugated Polymer Blends", *AMBIO,* 41 (2012), 135-137.

[59] Y. Liu, J. He, O. Kwon, and D. M. Zhu, "Probing Local Surface Conductance Using Current Sensing Atomic Force Microscopy", *Review of Scientific Instruments,* 83 (2012), 013701.

[60] H. M. Su, Y. C. Zhong, X. Wang, X. G. Zheng, J. F. Xu, and H. Z. Wang, "Effects of Polarization on Laser Holography for Microstructure Fabrication", *Physical Review E* 67 (2003), 056619.

[61] A. Rodriguez, M. Echeverría, M. Ellman, N. Perez, Y. K. Verevkin, C. S. Peng, T. Berthou, Z. Wang, I. Ayerdi, J. Savall, and S. M. Olaizola, "Laser Interference Lithography for Nanoscale Structuring of Materials: From Laboratory to Industry", *Microelectronic Engineering,* 86 (2009), 937-940.

[62] S. Z. Wu, D. Wu, J. Yao, Q. D. Chen, J. N. Wang, L. G. Niu, H. H. Fang, and H. B. Sun, "One-Step Preparation of Regular Micropearl Arrays for Two-Direction Controllable Anisotropic Wetting", *Langmuir,* 26 (2010), 12012-12016.

[63] D. Wu, Q. D. Chen, H. Xia, J. Jiao, B. B. Xu, X.-F. Lin, Y. Xu, and H.-B. Sun, "A Facile Approach for Artificial Biomimetic Surfaces with Both Superhydrophobicity and Iridescence", *Soft Matter,* 6 (2010), 263-263.

[64] C. Tan, C. S. Peng, V. N. Petryakov, Y. K. Verevkin, J. Zhang, Z. Wang, S. M. Olaizola, T. Berthou, S. Tisserand, and M. Pessa, "Line Defects in Two-Dimensional Four-Beam Interference Patterns", *New Journal of Physics,* 10 (2008), 023023.

[65] C. Tan, C. S. Peng, J. Pakarinen, M. Pessa, V. N. Petryakov, Y. K. Verevkin, J. Zhang, Z. Wang, S. M. Olaizola, T. Berthou, and S. Tisserand, "Ordered Nanostructures Written Directly by Laser Interference", *Nanotechnology,* 20 (2009), 125303.

[66] X. Li, Y. Shimizu, S. Ito, and W. Gao, "Fabrication of Scale Gratings for Surface Encoders by Using Laser Interference Lithography with 405 Nm Laser Diodes", *International Journal of Precision Engineering and Manufacturing,* 14 (2013), 1979-1988.

[67] R. Catrin, D. Horwat, J. F. Pierson, S. Migot, Y. Hu, and F. Mücklich, "Nano-Scale and

Surface Precipitation of Metallic Particles in Laser Interference Patterned Noble Metal-Based Thin Films", *Applied Surface Science,* 257 (2011), 5223-5229.

[68] A. F. Lasagni, D. Langheinrich, and S. Eckhardt, "Direct Fabrication of Periodic Patterns on Polymers Using Laser Interference", *Society of Plastics Engineers,* 53 (2012), 1-2.

[69] J. Sutanto, R. L. Smith, and S. D. Collins, "Fabrication of Nano-Gap Electrodes and Nano Wires Using an Electrochemical and Chemical Etching Technique", *Journal of Micromechanics and Microengineering,* 20 (2010), 045016.

[70] K. Y. Lai, Y. R. Lin, H. P. Wang, and J. H. He, "Synthesis of Anti-Reflective and Hydrophobic Si Nanorod Arrays by Colloidal Lithography and Reactive Ion Etching", *CrystEngComm,* 13 (2011), 1014-1014.

[71] V. Grigaliūnas, S. Tamulevičius, M. Muehlberger, D. Jucius, A. Guobienė, V. Kopustinskas, and A. Gudonytė, "Nanoimprint Lithography Using Ir Laser Irradiation", *Applied Surface Science,* 253 (2006), 646-650.

[72] T. H. Her, R. J. Finlay, C. Wu, S. Deliwala, and E. Mazur, "Microstructuring of Silicon with Femtosecond Laser Pulses", *Applied Physics Letters,* 73 (1998), 1673-1675.

[73] J. D. Fowlkes, A. J. Pedraza, and D. H. Lowndes, "Microstructural Evolution of Laser-Exposed Silicon Targets in Sf6 Atmospheres", *Applied Physics Letters,* 77 (2000), 1629-1631.

[74] M. Y. Shen, C. H. Crouch, J. E. Carey, R. Younkin, E. Mazur, M. Sheehy, and C. M. Friend, "Formation of Regular Arrays of Silicon Microspikes by Femtosecond Laser Irradiation through a Mask", *Applied Physics Letters,* 82 (2003), 1715-1717.

[75] C. H. Crouch, J. E. Carey, M. Shen, E. Mazur, and F. Y. Génin, "Infrared Absorption by Sulfur-Doped Silicon Formed by Femtosecond Laser Irradiation", *Applied Physics A,* 79 (2004), 1635-1641.

[76] C. H. Crouch, J. E. Carey, J. M. Warrender, M. J. Aziz, E. Mazur, and F. Y. Génin, "Comparison of Structure and Properties of Femtosecond and Nanosecond Laser-Structured Silicon", *Applied Physics Letters,* 84 (2004), 1850-1852.

[77] A. Y. Vorobyev, and C. Guo, "Direct Creation of Black Silicon Using Femtosecond Laser Pulses", *Applied Surface Science,* 257 (2011), 7291-7294.

[78] Y. Xia, B. Liu, J. Liu, Z. Shen, and C. Li, "A Novel Method to Produce Black Silicon for Solar Cells", *Solar Energy,* 85 (2011), 1574-1578.

[79] X. Bao, F. Liu, and X. Zhou, "Photovoltaic Properties of Black Silicon Microstructured by Femtosecond Pulsed Laser", *Optik,* 123 (2012), 1474-1477.

[80] H. Mei, C. Wang, J. Yao, Y. C. Chang, J. Cheng, Y. Zhu, S. Yin, and C. Luo, "Development of Novel Flexible Black Silicon", *Optics Communications,* 284 (2011), 1072-1075.

[81] M. Halbwax, T. Sarnet, P. Delaporte, M. Sentis, H. Etienne, F. Torregrosa, V. Vervisch, I. Perichaud, and S. Martinuzzi, "Micro and Nano-Structuration of Silicon by Femtosecond Laser: Application to Silicon Photovoltaic Cells Fabrication", *Thin Solid Films,* 516 (2008),

6791-6795.

[82] M. A. Sheehy, B. R. Tull, C. M. Friend, and E. Mazur, "Chalcogen Doping of Silicon Via Intense Femtosecond-Laser Irradiation", *Materials Science and Engineering B,* 137 (2007), 289-294.

[83] K. Liu, and L. Jiang, "Bio-Inspired Self-Cleaning Surfaces", *Annual Review of Materials Research,* 42 (2012), 231-263.

[84] J. N. Wang, R. Q. Shao, Y. L. Zhang, L. Guo, H. B. Jiang, D. X. Lu, and H. B. Sun, "Biomimetic Graphene Surfaces with Superhydrophobicity and Iridescence", *Chemistry—An Asian Journal,* 7 (2012), 301-304.

[85] Y. R. Lin, K. Y. Lai, H. P. Wang, and J. H. He, "Slope-Tunable Si Nanorod Arrays with Enhanced Antireflection and Self-Cleaning Properties", *Nanoscale,* 2 (2010), 2765–2768.

[86] R. Dewan, S. Fischer, V. B. Meyer-Rochow, Y. Özdemir, S. Hamraz, and D. Knipp, "Studying Nanostructured Nipple Arrays of Moth Eye Facets Helps to Design Better Thin Film Solar Cells", *Bioinspiration and Biomimetics,* 7 (2012), 016003.

[87] S. Ji, J. Park, and H. Lim, "Improved Antireflection Properties of Moth Eye Mimicking Nanopillars on Transparent Glass: Flat Antireflection and Color Tuning", *Nanoscale,* 4 (2012), 4603-4610.

[88] S. Ji, K. Song, T. B. Nguyen, N. Kim, and H. Lim, "Optimal Moth Eye Nanostructure Array on Transparent Glass Towards Broadband Antireflection", *ACS applied materials & interfaces,* 5 (2013), 10731-10737.

[89] J. Rao, R. Winfield, and L. Keeney, "Moth-Eye-Structured Light-Emitting Diodes", *Optics Communications,* 283 (2010), 2446-2450.

[90] C. T. Wu, C. H. Lin, C. Cheng, C. S. Wu, H. C. Ting, F. C. Chang, and F. H. Ko, "Design of Artificial Hollow Moth-Eye Structures Using Anodic Nanocones for High-Performance Optics", *Chemistry of Materials,* 22 (2010), 6583-6589.

[91] D. H. Ko, J. R. Tumbleston, K. J. Henderson, L. E. Euliss, J. M. DeSimone, R. Lopez, and E. T. Samulski, "Biomimetic Microlens Array with Antireflective “Moth-Eye” Surface", *Soft Matter,* 7 (2011), 6404-6407.

[92] C. H. Sun, P. Jiang, and B. Jiang, "Broadband Moth-Eye Antireflection Coatings on Silicon", *Applied Physics Letters,* 92 (2008), 061112.

[93] B. J. Bae, S.-H. Hong, E.-J. Hong, H. Lee, and G.-y. Jung, "Fabrication of Moth-Eye Structure on Glass by Ultraviolet Imprinting Process with Polymer Template", *Japanese Journal of Applied Physics,* 48 (2009), 010207.

[94] P. Qu, F. Chen, H. Liu, Q. Yang, J. Lu, and J. Si, "A Simple Route to Fabricate Artificial Compound Eye Structures", *Optics Express,* 20 (2012), 5775-5782.

[95] I. Talian, M. Aranyosiova, A. Oriňák, D. Velič, D. Haško, D. Kaniansky, R. Oriňáková, and J. Hübner, "Functionality of Novel Black Silicon Based Nanostructured Surfaces Studied by Tof Sims", *Applied Surface Science,* 256 (2010), 2147-2154.

[96] B. Kang, J. Noh, J. Lee, and M. Yang, "Heterodyne Interference Lithography for One-Step Micro/Nano Multiscale Structuring", *Applied Physics Letters,* 103 (2013), 243111-243114.

[97] Y. F. Liu, J. Feng, Y. G. Bi, J. F. Song, Y. Jin, Y. Bai, Q. D. Chen, and H. B. Sun, "Omnidirectional Emission from Top-Emitting Organic Light-Emitting Devices with Microstructured Cavity", *Optics Letters,* 37 (2012), 124-126.

[98] D. D. Zhang, J. Feng, H. Wang, Y. F. Liu, L. Chen, Y. Jin, Y. Q. Zhong, Y. Bai, Q. D. Chen, and H.-B. Sun, "Efficiency Enhancement in Organic Light-Emitting Devices with a Magnetic Doped Hole-Transport Layer", *IEEE Photonics Journal,* 3 (2011), 26-30.

[99] J. Son, S. Kundu, L. K. Verma, M. Sakhuja, A. J. Danner, C. S. Bhatia, and H. Yang, "A Practical Superhydrophilic Self Cleaning and Antireflective Surface for Outdoor Photovoltaic Applications", *Solar Energy Materials and Solar Cells,* 98 (2012), 46-51.

[100] K. C. Park, H. J. Choi, C. H. Chang, R. E. Cohen, G. H. McKinley, and G. Barbastathis, "Nanotextured Silica Surfaces with Robust Superhydrophobicity and Omnidirectional Broadband Supertransmissivity", *ACS Nano,* 6 (2012), 3789-3799.

[101] J. Oh, H. C. Yuan, and H. M. Branz, "An 18.2%-Efficient Black-Silicon Solar Cell Achieved through Control of Carrier Recombination in Nanostructures", *Nature nanotechnology,* 7 (2012), 743-748.

[102] R. H. Fan, L. H. Zhu, R. W. Peng, X. R. Huang, D. X. Qi, X. P. Ren, Q. Hu, and M. Wang, "Broadband Antireflection and Light-Trapping Enhancement of Plasmonic Solar Cells", *Physical Review B,* 87 (2013), 195444.

[103] S. Ji, K. Song, T. B. Nguyen, N. Kim, and H. Lim, "Optimal Moth Eye Nanostructure Array on Transparent Glass Towards Broadband Antireflection", *ACS Appl Mater Interfaces,* 5 (2013), 10731-10737.

[104] A. Lasagni, M. D'Alessandria, R. Giovanelli, and F. Mücklich, "Advanced Design of Periodical Architectures in Bulk Metals by Means of Laser Interference Metallurgy", *Applied Surface Science,* 254 (2007), 930-936.

[105] D. H. Lee, J. Y. Kwon, S. Maldonado, A. Tuteja, and A. Boukai, "Extreme Light Absorption by Multiple Plasmonic Layers on Upgraded Metallurgical Grade Silicon Solar Cells", *Nano Letters,* 14 (2014), 1961-1967.

[106] T. An, S. J. Cho, W. S. Choi, J. H. Kim, S. T. Lim, and G. Lim, "Preparation of Stable Superhydrophobic Mesh with a Biomimetic Hierarchical Structure", *Soft Matter,* 7 (2011), 9867–9870.

[107] R. K. Heilmann, C. G. Chen, P. T. Konkola, and M. L. Schattenburg, "Dimensional Metrology for Nanometre-Scale Science and Engineering: Towards Sub-Nanometre Accurate Encoders", *Nanotechnology,* 15 (2004), 504-511.

[108] R. K. Heilmann, P. T. Konkola, C. G. Chen, G. S. Pati, and M. L. Schattenburg, "Digital Heterodyne Interference Fringe Control System", *Journal of Vacuum Science and Technology B,* 19 (2001), 2342-2346.

[109] R. Sidharthan, and V. Murukeshan, "Periodic Feature Patterning by Lens Based Solid Immersion Multiple Beam Laser Interference Lithography", *Laser Physics Letters,* 9 (2012), 691.

[110] J. D. Boor, D. S. Kim, and V. Schmidt, "Sub-50 Nm Patterning by Immersion Interference Lithography Using a Littrow Prism as a Lloyd's Interferometer", *Optics letters,* 35 (2010), 3450-3452.

[111] T. M. Bloomstein, and M. F. Marchant, "22-nm Immersion Interference Lithography", *Optics Express,* 14 (2006), 6434-6443.

[112] F. Mücklich, A. Lasagni, and C. Daniel, "Laser Interference Metallurgy-Periodic Surface Patterning and Formation of Intermetallics", *Intermetallics,* 13 (2005), 437-442.

[113] P. G. Engleman, N. Dahotre, A. Kurella, A. Samant, and C. Blue, "The Application of Laser-Induced Multi-Scale Surface Texturing", *Journal of The Minerals, Metals & Materials Society,* 57 (2005), 46-50.

[114] X. Wang, L. Vincent, and D. Bullen, "Scanning Probe Lithography Tips with Spring-on-Tip Designs: Analysis, Fabrication, and Testing", *Applied Physics Letters,* 87 (2005), 0541021-0541023.

[115] S. Alexey, Y. Izzet, P. Dirch Hjorth, B. Peter, B. Malte, K. Florian, O. Maria, and H. Torsten, "Ultra-High Aspect Ratio Replaceable Afm Tips Using Deformation-Suppressed Focused Ion Beam Milling", *Nanotechnology,* 24 (2013), 4657011-4657018.

[116] L. Wang, H. Y. Wang, B. R. Gao, L. Y. Pan, Y. Jiang, Q. D. Chen, W. Han, and H. B. Sun, "Transient Absorption Spectroscopic Study on Band-Structure-Type Change in Cdte/Cds Core-Shell Quantum Dots", *IEEE Journal of Quantum Electronics,* 47 (2011), 1177-1184.

[117] A. V. Kildishev, A. Boltasseva, and V. M. Shalaev, "Planar Photonics with Metasurfaces", *Science,* 339 (2013), 12320091-12320096.

[118] Y. Chen, G. Song, J. Xiao, L. Yu, and J. Zhang, "Subwavelength Polarization Beam Splitter with Controllable Splitting Ratio Based on Surface Plasmon Polaritons", *Optics Express,* 21 (2013), 314-321.

[119] S. Indrišiūnas, B. Voisiat, M. Gedvilas, and G. Račiukaitis, "Two Complementary Ways of Thin-Metal-Film Patterning Using Laser Beam Interference and Direct Ablation", *Journal of Micromechanics and Microengineering,* 23 (2013), 0950341-0950349.

[120] S. Jeon, J. H. Jeong, Y. S. Song, W. I. Jeong, J. J. Kim, and J. R. Youn, "Vacuum Nano-Hole Array Embedded Organic Light Emitting Diodes", *Nanoscale,* 6 (2014), 2642-2648.

[121] J. Bai, C. Yang, M. Athanasiou, and T. Wang, "Efficiency Enhancement of Ingan/Gan Solar Cells with Nanostructures", *Applied Physics Letters,* 104 (2014), 051129.

[122] N. Yu, P. Genevet, M. A. Kats, F. Aieta, J.-P. Tetienne, F. Capasso, and Z. Gaburro, "Light Propagation with Phase Discontinuities: Generalized Laws of Reflection and Refraction", *Science,* 334 (2011), 333-337.

[123] J. Lin, J. P. B. Mueller, Q. Wang, G. Yuan, N. Antoniou, X. C. Yuan, and F. Capasso,

"Polarization-Controlled Tunable Directional Coupling of Surface Plasmon Polaritons", *Science,* 340 (2013), 331-334.

Appendix A-Matlab Scripts

```
%Measurement for period in the x axis direction
Clear all
format long;
format compact;
I1=imread('');% filename of interference patterns
save zhouqi1.mat;
load zhouqi1;
T0=40;
t1=100; t2=199;
T=200+2*T0;
A=I1(t1:t2,200:T);
j=0;
k=0;
m=0;
n=0;
a=1:1:120;
for i=1:1:120
    j=i+200;
    k=T+i;
    D=I1(t1:t2,j:k);
    a([i])=corr2(A,D);
end
plot(a);
hold on;
xlabel('Pixel number of phase shifts');ylabel('correlation coefficients');
legend('r0');
grid on;
N=a;
i=0;
for k=1:119
    if (N(k)>=0)&(N(k+1)<=0)
        i=i+1;
        x(i)=k;
    end;
```

```
end;
x1=[x(1) x(1)+1];
y1=[a(x(1)) a((x(1)+1))];
yi=0;
xi1a=interp1(y1,x1,yi);
z2=[x(2) x(2)+1];
y2=[a(x(2)) a((x(2)+1))];
yi2=0;
xi1b2=interp1(y2,z2,yi2);
p=xi1b2-xi1a
%Measurement for period in the x axis direction
clear all
  format long;
format compact;
I1=imread(''); % filename of interference patterns
save zhouqi1.mat;
load zhouqi1;
T0=40;
t1=100; t2=199;
T=200+2*T0;
A=I1(t1:t2,200:T);
j=0;
k=0;
m=0;
n=0;
a=1:1:120;
for i=1:1:120
        j=i+100;
        k=199+i;
        D=I1(j:k,200:T);
        a([i])=corr2(A,D);
end
plot(a);
hold on;
xlabel('Pixel number of phase shifts');ylabel('correlation coefficients');
legend('r0');
grid on;
```

```
N=a;
i=0;
for k=1:119
    if (N(k)>=0)&(N(k+1)<=0)
        i=i+1;
        x(i)=k;
    end;
end;
x1=[x(1) x(1)+1];
y1=[a(x(1)) a((x(1)+1))];
yi=0;
xi1a=interp1(y1,x1,yi);
z2=[x(2) x(2)+1];
y2=[a(x(2)) a((x(2)+1))];
yi2=0;
xi1b2=interp1(y2,z2,yi2);
p=xi1b2-xi1a

%Measurement for contrast of interference patterns
clc;
clear all;
format long;
I1=imread(''); % filename of interference patterns
I2=double(I1);
A=I2;
clear vision;
k=1;
for i=1:10:(960-96);
for j=1:10:(1280-128);
m1=max(max(A(i:i+95,j:j+127)));
m2=min(min(A(i:i+95,j:j+127)));
vision(k)=(m1-m2)/(m1);
k=k+1
end;
end;
visionk=mean(vision)
```

```
%2D intensity profile of TE-TE-TM-TM polarisation mode
clc
clear
lamda=200*1e-9;
k=2*pi/lamda;
thita=(pi/180)*6;%incident angles
thitb=(pi/180)*9;%misaligned angle
x=linspace(-2000,100,2000)*1e-8;
y=linspace(-2000,100,2000)*1e-8;
z=0*1e-9;
[X,Y,Z] = meshgrid(x,y,z);
I=4+2*(sin(thita)^2-cos(thita)^2)*cos(2*k*sin(thita)*Y)+2*cos(thita)*cos(k*sin(thita)*X-k*sin(thit
a)*Y)-2*cos(thita)*cos(k*sin(thita)*X+k*sin(thita)*Y)-2*cos(k*sin(thita)*X+k*sin(thitb)*X)-2*cos(
thita)*cos(k*sin(thitb)*X+k*sin(thita)*Y)+2*cos(thita)*cos(k*sin(thitb)*X-k*sin(thita)*Y);
imagesc(x,y,I);
```

Appendix B-the Data of Standard Plate for Reflectivity

Init E (V) = 0

Sample Interval (s) = 0.1

Run Time (sec) = 1

Quiet Time (sec) = 0

Sensitivity (A/V) = 1e-6

380nm	390nm	400nm	410
Time/sec, Current/A	Time/sec, Current/A	Time/sec, Current/A	Time/sec, Current/A
1.000e-1, 5.519e-8	1.000e-1, 6.818e-8	1.000e-1, 8.594e-8	1.000e-1, 9.000e-8
2.000e-1, 5.512e-8	2.000e-1, 6.806e-8	2.000e-1, 8.602e-8	2.000e-1, 8.971e-8
3.000e-1, 5.487e-8	3.000e-1, 6.863e-8	3.000e-1, 8.589e-8	3.000e-1, 8.956e-8
4.000e-1, 5.520e-8	4.000e-1, 6.817e-8	4.000e-1, 8.610e-8	4.000e-1, 8.938e-8
5.000e-1, 5.491e-8	5.000e-1, 6.790e-8	5.000e-1, 8.567e-8	5.000e-1, 8.995e-8
6.000e-1, 5.499e-8	6.000e-1, 6.820e-8	6.000e-1, 8.558e-8	6.000e-1, 9.016e-8
7.000e-1, 5.525e-8	7.000e-1, 6.830e-8	7.000e-1, 8.595e-8	7.000e-1, 9.056e-8
8.000e-1, 5.476e-8	8.000e-1, 6.784e-8	8.000e-1, 8.568e-8	8.000e-1, 9.013e-8
9.000e-1, 5.529e-8	9.000e-1, 6.736e-8	9.000e-1, 8.595e-8	9.000e-1, 8.949e-8
1.000e+0, 5.519e-8	1.000e+0, 6.776e-8	1.000e+0, 8.582e-8	1.000e+0, 8.956e-8
420nm	430nm	440nm	450nm
Time/sec, Current/A	Time/sec, Current/A	Time/sec, Current/A	Time/sec, Current/A
1.000e-1, 9.943e-8	1.000e-1, 1.169e-7	1.000e-1, 1.228e-7	1.000e-1, 1.342e-7
2.000e-1, 1.000e-7	2.000e-1, 1.160e-7	2.000e-1, 1.223e-7	2.000e-1, 1.347e-7
3.000e-1, 9.939e-8	3.000e-1, 1.164e-7	3.000e-1, 1.212e-7	3.000e-1, 1.353e-7
4.000e-1, 9.976e-8	4.000e-1, 1.161e-7	4.000e-1, 1.220e-7	4.000e-1, 1.347e-7
5.000e-1, 1.002e-7	5.000e-1, 1.158e-7	5.000e-1, 1.217e-7	5.000e-1, 1.348e-7
6.000e-1, 1.004e-7	6.000e-1, 1.157e-7	6.000e-1, 1.224e-7	6.000e-1, 1.346e-7
7.000e-1, 1.009e-7	7.000e-1, 1.158e-7	7.000e-1, 1.221e-7	7.000e-1, 1.340e-7
8.000e-1, 1.007e-7	8.000e-1, 1.157e-7	8.000e-1, 1.221e-7	8.000e-1, 1.349e-7
9.000e-1, 1.006e-7	9.000e-1, 1.148e-7	9.000e-1, 1.224e-7	9.000e-1, 1.343e-7
1.000e+0, 9.988e-8	1.000e+0, 1.150e-7	1.000e+0, 1.225e-7	1.000e+0, 1.338e-7
460nm	470nm	480nm	490nm
Time/sec, Current/A	Time/sec, Current/A	Time/sec, Current/A	Time/sec, Current/A
1.000e-1, 1.741e-7	1.000e-1, 2.480e-7	1.000e-1, 2.279e-7	1.000e-1, 2.337e-7
2.000e-1, 1.733e-7	2.000e-1, 2.493e-7	2.000e-1, 2.272e-7	2.000e-1, 2.341e-7
3.000e-1, 1.743e-7	3.000e-1, 2.475e-7	3.000e-1, 2.267e-7	3.000e-1, 2.330e-7
4.000e-1, 1.743e-7	4.000e-1, 2.478e-7	4.000e-1, 2.277e-7	4.000e-1, 2.352e-7
5.000e-1, 1.750e-7	5.000e-1, 2.482e-7	5.000e-1, 2.267e-7	5.000e-1, 2.352e-7
6.000e-1, 1.734e-7	6.000e-1, 2.473e-7	6.000e-1, 2.252e-7	6.000e-1, 2.339e-7
7.000e-1, 1.749e-7	7.000e-1, 2.489e-7	7.000e-1, 2.268e-7	7.000e-1, 2.344e-7
8.000e-1, 1.737e-7	8.000e-1, 2.481e-7	8.000e-1, 2.272e-7	8.000e-1, 2.345e-7
9.000e-1, 1.750e-7	9.000e-1, 2.499e-7	9.000e-1, 2.276e-7	9.000e-1, 2.343e-7
1.000e+0, 1.750e-7	1.000e+0, 2.487e-7	1.000e+0, 2.281e-7	1.000e+0, 2.347e-7

500nm	510nm	520nm	530nm
Time/sec, Current/A	Time/sec, Current/A	Time/sec, Current/A	Time/sec, Current/A
1.000e-1, 2.335e-7	1.000e-1, 2.306e-7	1.000e-1, 2.388e-7	1.000e-1, 2.461e-7
2.000e-1, 2.332e-7	2.000e-1, 2.312e-7	2.000e-1, 2.377e-7	2.000e-1, 2.472e-7
3.000e-1, 2.322e-7	3.000e-1, 2.333e-7	3.000e-1, 2.384e-7	3.000e-1, 2.474e-7
4.000e-1, 2.339e-7	4.000e-1, 2.326e-7	4.000e-1, 2.388e-7	4.000e-1, 2.462e-7
5.000e-1, 2.339e-7	5.000e-1, 2.314e-7	5.000e-1, 2.405e-7	5.000e-1, 2.462e-7
6.000e-1, 2.334e-7	6.000e-1, 2.321e-7	6.000e-1, 2.396e-7	6.000e-1, 2.450e-7
7.000e-1, 2.350e-7	7.000e-1, 2.300e-7	7.000e-1, 2.388e-7	7.000e-1, 2.429e-7
8.000e-1, 2.339e-7	8.000e-1, 2.314e-7	8.000e-1, 2.413e-7	8.000e-1, 2.454e-7
9.000e-1, 2.339e-7	9.000e-1, 2.316e-7	9.000e-1, 2.393e-7	9.000e-1, 2.469e-7
1.000e+0, 2.351e-7	1.000e+0, 2.304e-7	1.000e+0, 2.391e-7	1.000e+0, 2.452e-7
540nm	550nm	560nm	570nm
Time/sec, Current/A	Time/sec, Current/A	Time/sec, Current/A	Time/sec, Current/A
1.000e-1, 2.540e-7	1.000e-1, 2.582e-7	1.000e-1, 2.623e-7	1.000e-1, 2.689e-7
2.000e-1, 2.525e-7	2.000e-1, 2.592e-7	2.000e-1, 2.625e-7	2.000e-1, 2.691e-7
3.000e-1, 2.534e-7	3.000e-1, 2.583e-7	3.000e-1, 2.642e-7	3.000e-1, 2.683e-7
4.000e-1, 2.536e-7	4.000e-1, 2.592e-7	4.000e-1, 2.647e-7	4.000e-1, 2.705e-7
5.000e-1, 2.541e-7	5.000e-1, 2.593e-7	5.000e-1, 2.658e-7	5.000e-1, 2.669e-7
6.000e-1, 2.518e-7	6.000e-1, 2.589e-7	6.000e-1, 2.640e-7	6.000e-1, 2.692e-7
7.000e-1, 2.538e-7	7.000e-1, 2.582e-7	7.000e-1, 2.647e-7	7.000e-1, 2.687e-7
8.000e-1, 2.531e-7	8.000e-1, 2.588e-7	8.000e-1, 2.642e-7	8.000e-1, 2.698e-7
9.000e-1, 2.513e-7	9.000e-1, 2.584e-7	9.000e-1, 2.634e-7	9.000e-1, 2.692e-7
1.000e+0, 2.549e-7	1.000e+0, 2.596e-7	1.000e+0, 2.646e-7	1.000e+0, 2.698e-7
580nm	590m	600nm	610nm
Time/sec, Current/A	Time/sec, Current/A	Time/sec, Current/A	Time/sec, Current/A
1.000e-1, 2.757e-7	1.000e-1, 2.779e-7	1.000e-1, 2.665e-7	1.000e-1, 2.576e-7
2.000e-1, 2.744e-7	2.000e-1, 2.784e-7	2.000e-1, 2.665e-7	2.000e-1, 2.576e-7
3.000e-1, 2.723e-7	3.000e-1, 2.776e-7	3.000e-1, 2.666e-7	3.000e-1, 2.582e-7
4.000e-1, 2.730e-7	4.000e-1, 2.775e-7	4.000e-1, 2.659e-7	4.000e-1, 2.582e-7
5.000e-1, 2.749e-7	5.000e-1, 2.776e-7	5.000e-1, 2.656e-7	5.000e-1, 2.602e-7
6.000e-1, 2.739e-7	6.000e-1, 2.772e-7	6.000e-1, 2.662e-7	6.000e-1, 2.592e-7
7.000e-1, 2.747e-7	7.000e-1, 2.778e-7	7.000e-1, 2.660e-7	7.000e-1, 2.585e-7
8.000e-1, 2.741e-7	8.000e-1, 2.777e-7	8.000e-1, 2.658e-7	8.000e-1, 2.570e-7
9.000e-1, 2.734e-7	9.000e-1, 2.782e-7	9.000e-1, 2.660e-7	9.000e-1, 2.577e-7
1.000e+0, 2.750e-7	1.000e+0, 2.773e-7	1.000e+0, 2.658e-7	1.000e+0, 2.590e-7
620nm	630nm	640nm	650nm
Time/sec, Current/A	Time/sec, Current/A	Time/sec, Current/A	Time/sec, Current/A
1.000e-1, 2.681e-7	1.000e-1, 2.613e-7	1.000e-1, 2.459e-7	1.000e-1, 2.437e-7
2.000e-1, 2.671e-7	2.000e-1, 2.593e-7	2.000e-1, 2.470e-7	2.000e-1, 2.436e-7
3.000e-1, 2.677e-7	3.000e-1, 2.606e-7	3.000e-1, 2.458e-7	3.000e-1, 2.432e-7
4.000e-1, 2.692e-7	4.000e-1, 2.601e-7	4.000e-1, 2.467e-7	4.000e-1, 2.433e-7
5.000e-1, 2.702e-7	5.000e-1, 2.604e-7	5.000e-1, 2.467e-7	5.000e-1, 2.439e-7

6.000e-1, 2.693e-7	6.000e-1, 2.614e-7	6.000e-1, 2.468e-7	6.000e-1, 2.442e-7
7.000e-1, 2.700e-7	7.000e-1, 2.612e-7	7.000e-1, 2.466e-7	7.000e-1, 2.441e-7
8.000e-1, 2.696e-7	8.000e-1, 2.619e-7	8.000e-1, 2.474e-7	8.000e-1, 2.442e-7
9.000e-1, 2.691e-7	9.000e-1, 2.613e-7	9.000e-1, 2.474e-7	9.000e-1, 2.440e-7
1.000e+0, 2.709e-7	1.000e+0, 2.600e-7	1.000e+0, 2.458e-7	1.000e+0, 2.440e-7
660nm	670nm	680nm	690nm
Time/sec, Current/A	Time/sec, Current/A	Time/sec, Current/A	Time/sec, Current/A
1.000e-1, 2.288e-7	1.000e-1, 2.309e-7	1.000e-1, 2.326e-7	1.000e-1, 2.559e-7
2.000e-1, 2.299e-7	2.000e-1, 2.316e-7	2.000e-1, 2.327e-7	2.000e-1, 2.551e-7
3.000e-1, 2.309e-7	3.000e-1, 2.312e-7	3.000e-1, 2.324e-7	3.000e-1, 2.568e-7
4.000e-1, 2.306e-7	4.000e-1, 2.315e-7	4.000e-1, 2.312e-7	4.000e-1, 2.565e-7
5.000e-1, 2.287e-7	5.000e-1, 2.315e-7	5.000e-1, 2.299e-7	5.000e-1, 2.565e-7
6.000e-1, 2.302e-7	6.000e-1, 2.309e-7	6.000e-1, 2.312e-7	6.000e-1, 2.554e-7
7.000e-1, 2.287e-7	7.000e-1, 2.310e-7	7.000e-1, 2.291e-7	7.000e-1, 2.562e-7
8.000e-1, 2.286e-7	8.000e-1, 2.309e-7	8.000e-1, 2.291e-7	8.000e-1, 2.580e-7
9.000e-1, 2.295e-7	9.000e-1, 2.312e-7	9.000e-1, 2.308e-7	9.000e-1, 2.562e-7
1.000e+0, 2.283e-7	1.000e+0, 2.318e-7	1.000e+0, 2.301e-7	1.000e+0, 2.550e-7
700nm	710nm	720nm	730nm
Time/sec, Current/A	Time/sec, Current/A	Time/sec, Current/A	Time/sec, Current/A
1.000e-1, 2.045e-7	1.000e-1, 1.927e-7	1.000e-1, 2.174e-7	1.000e-1, 2.046e-7
2.000e-1, 2.057e-7	2.000e-1, 1.934e-7	2.000e-1, 2.177e-7	2.000e-1, 2.046e-7
3.000e-1, 2.044e-7	3.000e-1, 1.930e-7	3.000e-1, 2.172e-7	3.000e-1, 2.048e-7
4.000e-1, 2.055e-7	4.000e-1, 1.934e-7	4.000e-1, 2.164e-7	4.000e-1, 2.036e-7
5.000e-1, 2.039e-7	5.000e-1, 1.934e-7	5.000e-1, 2.177e-7	5.000e-1, 2.054e-7
6.000e-1, 2.045e-7	6.000e-1, 1.928e-7	6.000e-1, 2.174e-7	6.000e-1, 2.049e-7
7.000e-1, 2.049e-7	7.000e-1, 1.941e-7	7.000e-1, 2.174e-7	7.000e-1, 2.056e-7
8.000e-1, 2.047e-7	8.000e-1, 1.928e-7	8.000e-1, 2.182e-7	8.000e-1, 2.061e-7
9.000e-1, 2.054e-7	9.000e-1, 1.937e-7	9.000e-1, 2.188e-7	9.000e-1, 2.051e-7
1.000e+0, 2.049e-7	1.000e+0, 1.932e-7	1.000e+0, 2.178e-7	1.000e+0, 2.051e-7
740nm	750nm	760nm	770nm
Time/sec, Current/A	Time/sec, Current/A	Time/sec, Current/A	Time/sec, Current/A
1.000e-1, 2.168e-7	1.000e-1, 1.929e-7	1.000e-1, 2.000e-7	1.000e-1, 2.713e-7
2.000e-1, 2.167e-7	2.000e-1, 1.915e-7	2.000e-1, 2.011e-7	2.000e-1, 2.703e-7
3.000e-1, 2.155e-7	3.000e-1, 1.938e-7	3.000e-1, 1.990e-7	3.000e-1, 2.699e-7
4.000e-1, 2.173e-7	4.000e-1, 1.927e-7	4.000e-1, 1.999e-7	4.000e-1, 2.704e-7
5.000e-1, 2.169e-7	5.000e-1, 1.925e-7	5.000e-1, 1.996e-7	5.000e-1, 2.700e-7
6.000e-1, 2.157e-7	6.000e-1, 1.954e-7	6.000e-1, 2.011e-7	6.000e-1, 2.701e-7
7.000e-1, 2.172e-7	7.000e-1, 1.960e-7	7.000e-1, 1.992e-7	7.000e-1, 2.701e-7
8.000e-1, 2.167e-7	8.000e-1, 1.954e-7	8.000e-1, 1.994e-7	8.000e-1, 2.723e-7
9.000e-1, 2.148e-7	9.000e-1, 1.931e-7	9.000e-1, 2.012e-7	9.000e-1, 2.707e-7
1.000e+0, 2.159e-7	1.000e+0, 1.948e-7	1.000e+0, 2.000e-7	1.000e+0, 2.711e-7